2020

Metal-Oxide Nanostructures Fabricated from Reactive Laser Ablation in Liquid

Mallory G. John

Virginia Commonwealth University

Doctoral Thesis

Metal-Oxide Nanostructures Fabricated from Reactive Laser Ablation in Liquid

---

Author: *Mallory G. John*

Supervisor: *Katharine M. Tibbetts*

A thesis submitted in fulfillment of the requirements

for the degree of Doctor of Philosophyin the

Department of Chemistry

31 March 2020

Abstract

The development of metal-oxide nanostructures is a growing area due to their applications in diverse fields spanning energy conversion and storage, chemical manufacturing, and environmental technology. This interest in catalytically active nanomaterials has prompted the synthesis and investigation of highly functionalized nanoparticles (NPs), including core-shell, silicate-stabilized, and bi- and multi-metallic nanocomposites. While wet-chemical synthesis methods of metal-oxide nanostructures have led to several morphologies, compositions, and shapes, these syntheses often require high temperatures, toxic solvents or reducing agents, and long reaction times.

Laser synthesis and processing of colloids (LSPC) encompasses both 'top down' and 'bottom up' approaches to synthesize metal-oxide nanostructures. Pulsed laser ablation in liquid (PLAL) involves focusing laser pulses onto a solid target immersed in a liquid in which target atoms coalesce to form nanostructured materials once ejected into solution. Laser reduction in liquid (LRL) is a second laser-assisted approach to synthesizing nanomaterials, where photochemical reduction of metal salts is achieved by focusing the laser beam into solution. Both PLAL and LRL are able to generate metal and semiconductor NPs at room temperature in aqueous solutions without added surfactants or stabilizers, giving them an advantage over conventional wet-chemical methods.

Recently, these two approaches have been combined into a single step- referred to as reactive laser ablation in liquid (RLAL), in which laser ablation of a solid target is carried out in a metal salt solution. This work goes through the synthesis and characterization of femtosecond-RLAL (fs-RLAL)-generated silica-metal nanostructures, and discusses the relationship between the precursor solution composition, the product morphology, and the catalytic activity toward a model para-nitrophenol (PNP) reduction reaction. First, silica-Au NPs were synthesized, exhibiting two populations of product nanoparticles which resulted

from reaction dynamics occurring on two distinct timescales. Next, silica-Cu NPs were synthesized under different pH conditions, yielding pH-dependent product morphology. The different morphologies resulted from the surface charge of ablated silica species, which repelled the Cu^{2+} ions in solution at low pH yielding core/shell morphology, and attracted the Cu^{2+} ions at high pH, forming well-dispersed $\sim$1.5 nm Cu clusters stabilized by a phyllosilicate matrix. This led to the investigation of pH-dependent dissolved silicate species generated from ablating the Si wafer in water and solutions of added $Ni(NO_3)_2$ over a range of pH conditions. When the solution was above pH 10, silicic acid was generated which was the key species leading to the formation of nickel-phyllosilicate (Ni-PS) when nickel nitrate was added to solution. When the solution was below pH 7, no silicic acid was generated from ablation, and consequently no Ni-PS was formed in the dried product. The mechanism of Ni-PS formation from fs-RLAL of a silicon wafer immersed in aqueous nickel nitrate solutions is discussed. Based on this mechanism, it is expected that the fs-RLAL method will be capable of generating a variety of metal-phyllosilicates from different metal salt precursors.

Acknowledgements

I am very grateful to Dr. Katharine Tibbetts, my advisor, for her care and support over the past five years. She has been an incredible mentor throughout my research, providing me with many opportunities to grow into the scientist and person I am today. I will always treasure my experience in her research group.

I would also like to thank my committee members: Dr. Hani El-Kaderi, Dr. Dusan Bratko, and Dr. Puru Jena. I am honored to have them on my committee and am very grateful for the support and feedback they have provided me through my time at VCU.

I am also very thankful for my fellow group members, as they have helped create a fun and supportive work environment that I deeply cherish. I am especially thankful for the friendships I have grown with Tori Meader, Laysa Frias, and Dr. Anna Forzano. The bond we have of going through this graduate program together is unique, and I deeply value them.

Finally, I am so lucky to have the support system of friends, family, and my partner Kyler O'Brien. My friends Sam, Molly, Devon, and Lisa have especially been role models in my life. Each of them is dedicated to their passion and strive to be the best version of themselves each day, and inspire me to be a better person and scientist. I am also very grateful to have a loving and caring family- words can't express my gratitude to my parents, Tom and Faith, and my sisters, Charlotte and Colleen, for their unconditional love and support for me throughout my life. My grandmother, Helen Weber, is an inspiration to me- her strength, kindness, and compassion motivate me to work hard through difficult times. I am also so fortunate to have Kyler O'Brien in my life. His patience, care, and insight have helped me stay grounded throughout my degree program, and I very lucky to have him by my side.

Contents

List of Figures

List of Tables

List of Abbreviations

AuNP	gold nanoparticle
NP	nanoparticle
LDH	layered double hydroxide
Au NP	gold nanoparticle
OER	oxygen evolution reaction
SEA	strong electrostatic adsorption
TOF	turnover frequence
LSPC	laser synthesis and processing of colloids
PLALP	pulsed laser ablation in liquid
LRL	laser reduction in liquid
RLAL	reactive laser ablation in liquid
fs-RLAL	femtosecond-reactive laser ablation in liquid
e^-_{aq}	hydrated or water-solvated electrons
OB	optical breakdown
PNP	*p*-nitrophenol
CCD	charge-coupled device
SAED	selected area electron diffraction
SPR	surface plasmon resonance
MOF	metal-organic framework
FWHM	full width at half mass
PAP	*p*-aminophenol
PDI	polydispersity index
PZC	point of zero charge
Cu-PS	copper-phyllosilicate
Ni-PS	nickel-phyllosilicate
Co-PS	cobalt-phyllosilicate

MS	metasilicate
SA	silicic acid
FFT	fast Fourier transform
SN	supernatant

List of Symbols

P	power	W ($J s^{-1}$)
I	intensity (peak irradiance)	W cm^{-2}
τ_p	pulse duration	fs
sE_p	pulse energy	J
ρ_e	electron density	cm^{-3}
Δ	band gap	eV
k_{app}	apparent rate constant (s^{-1}	
k_{Au}	mol Au-normalized rate constant (s^{-1} μmol Au^{-1})	
k_1	SSA-normalized rate constant ($Lm^{-2}s^{-1}$)	
μs	microsecond (10^{-6}s)	
ns	nanosecond (10^{-9}s)	
ps	picosecond (10^{-12}s)	
fs	femtosecond (10^{-15}s)	

Chapter 1

Introduction

1.1 Background and motivation

1.1.1 Properties and applications of metal-oxide nanostructures

Functional nanostructures are widely studied for their applications in biomedicine, sensing, optoelectronics, and catalysis.[1–3] In particular, significant attention has been paid to the development of various metal and metal-oxide-based catalysts for reactions including water splitting, the water-gas shift reaction, CO_2 conversion, and biomass utilization.[4–6] Catalytically active metal nanostructures such as Ag, Au, Pd, Pt, Ru, and Ir are highly active and stable over a range of experimental conditions; however, due to their low abundance and high cost, the development of transition metal-based nanostructures (Fe, Co, Ni, Cu, Zn) is gaining significant attention as low-cost alternatives to the noble metal-based nanostructures.[4,6–12] Incorporating the transition metals with highly functionalized oxide support materials such as silica, titania, or alumina increases both the catalytic activity and the stability of the metal NPs over a range of experimental conditions, due to the enhanced metal-support interactions.[13–18] Ideal features of highly active nanocatalysts include high surface area with high numbers of accessible active sites, and durability over continued reaction cycles.[19] Nanoparticles (NPs) have an exceptionally high surface-to-volume ratio compared to bulk materials, which may be increased further by decreasing the metal NP size or modifying the shape to include edges or steps.[20,21] Incorporating the metal NPs throughout a support material has led to the development of highly functionalized nanostructures including layered double hydroxides (LDH), metal-phyllosilicates, nanohybrids, mixed metal spinels, as well as unique shapes and morphologies of core/shell particles and alloyed nanoparticles, exhibiting high

catalytic activity and stability.[15,22–24] These structured nanomaterials have exhibited exceptional activity toward catalytic reactions, including Ni-Fe LDHs grown on carbon nanotubes that had higher electrocatalytic activity toward OER than commercial Ir catalysts[17], and Ni-NP embedded titania/silica catalysts with high activity and stability toward CO_2 reforming of methane.[25] These are a few examples of the promising nanostructured materials comprised of earth-abundant elements for environmentally relevant catalytic applications.

1.2 Synthesis approaches to metal-oxide nanostructures

Synthesizing oxide supported metal nanostructures has been achieved through a variety of wet chemical approaches, including incipient wetness impregnation, deposition-precipitation, strong electrostatic adsorption, and ammonia evaporation.[18,26–30] In these methods, the oxidic support such as silica, can be prepared from the Stöber method, from sol-gel synthesis, or using fumed amorphous silica. Subsequent introduction of the metal complex precursor to interact with the support material is conducted by heating up the slurry or solution, followed by calcining the finished product.[30]

The surface of oxidic supports (SiO_2, Al_2O_3, TiO_2) contain hydroxyl groups which act as adsorption sites for metal complexes and are the key to interactions between the metal precursor and support.[31] Depending on the pH of the aqueous solution, the hydroxyl ligands may become protonated (acidic) or deprotonated (alkaline), allowing for strong adsorption interactions between the support and the metal complex. This concept has been used for strong electrostatic adsorption (SEA) synthesis of very small (∼1.5 nm) metal NPs comprised of highly dispersed Ni, Ru, Cu, Pd, and Pt NPs throughout amorphous silica supports.[30,32] Heterogeneous catalyst development also focuses on increasing the density of metal NPs dispersed over support materials by increasing the specific surface area (SSA) of the catalytically active metal NPs, achieved by decreasing the NP size. However, previous reports on nanocatalyst synthesis have shed light on how poorly understood the structure-activity relationship is of these materials. For example, 2 nm Pt NPs in polymer electrolyte membrane fuel cells were unstable over time, but increasing the size to 5 nm Pt NPs resulted in nearly no catalyst deactivation.[33] In a separate study, the turnover frequency (TOF), a parameter used to describe the relationship between the nature of the active sites of a nanocatalyst and the SSA of it, decreased for a cobalt catalyst when the Co NP size was reduced below 6 nm, but no

decrease in TOF was observed when the size of the Co NPs was increased above 6 nm up to 15 nm.[34] These methods often result in uneven distributions of the metal precursror throughout the oxide support, resulting in poorly dispersed NPs with large size distributions and low metal loading. Additionally, synthesis of these materials involve multiple steps that take up to several days and require toxic organic reducing agents and surfactants.[30,35] These studies indicate that developing a rapid, facile, and environmentally-friendly synthesis method to oxide-metal nanostructures remains a challenge.

1.2.1 Laser Synthesis and Processing of Colloids

Laser synthesis and processing of colloids (LSPC) is an emerging field and nanomaterial synthesis.[36,37] This field encompasses the synthesis of colloidal NPs using intense laser pulses focused into liquid solutions. The first type of laser-assisted NP synthesis technique involved ablating a silicon target in liquid by focusing laser pulses into a liquid using a "ruby flash" at 694 nm.[38] This field has since exploded over the past several decades, leading to better understanding and thus control over nanoparticle synthesis. Due to the highly nonequilibrium environment generated in the laser plasma, unique and metastable phases are generated which are difficult to access using benchtop methods.[36] Since photons are the major reactant driving the formation of NPs in LSPC, the use of reducing agents is not required, and under certain laser parameters the colloidal NPs are electrostatically stabilized, making the addition of stabilizing agents or surfactants unnecessary. The ability to synthesize metal and semiconductor nanostrucures in a single step at room temperature in water gives LSPC a major advantage over conventional wet chemical synthesis approaches.[36,39–44]

Two common approaches to colloidal metal NP synthesis using laser-assisted methods involve a top-down and a bottom-up approach. In the top-down approach, laser pulses are focused onto the surface of a solid target immersed in liquid, where the ejected atoms are quenched by the surrounding liquid, forming nanoparticles. This technique is referred to as Pulsed Laser Ablation in Liquid (PLAL).[36,43] The second approach involves irradiating a metal-salt solution to produce reducing agents via solvent-molecule photolysis, referred to as Laser Reduction in Liquid (LRL)[45–47] Controlling nucleation and growth of the nanoparticles during metal-salt reduction by changing laser parameters (focusing conditions, pulse duration, pulse energy, irradiation time), and chemical parameters (metal-ion concentration,

solvent composition, presence of capping agents), determines the size, shape, and stability of the colloidal products[45–60]. The experimental setup for PLAL and LRL synthesis of NPs is very simple, allowing for efficient exploration of nanomaterial development and optimization. Figure 1.1 displays the laser conditions involved in PLAL and LRL synthesis techniques.

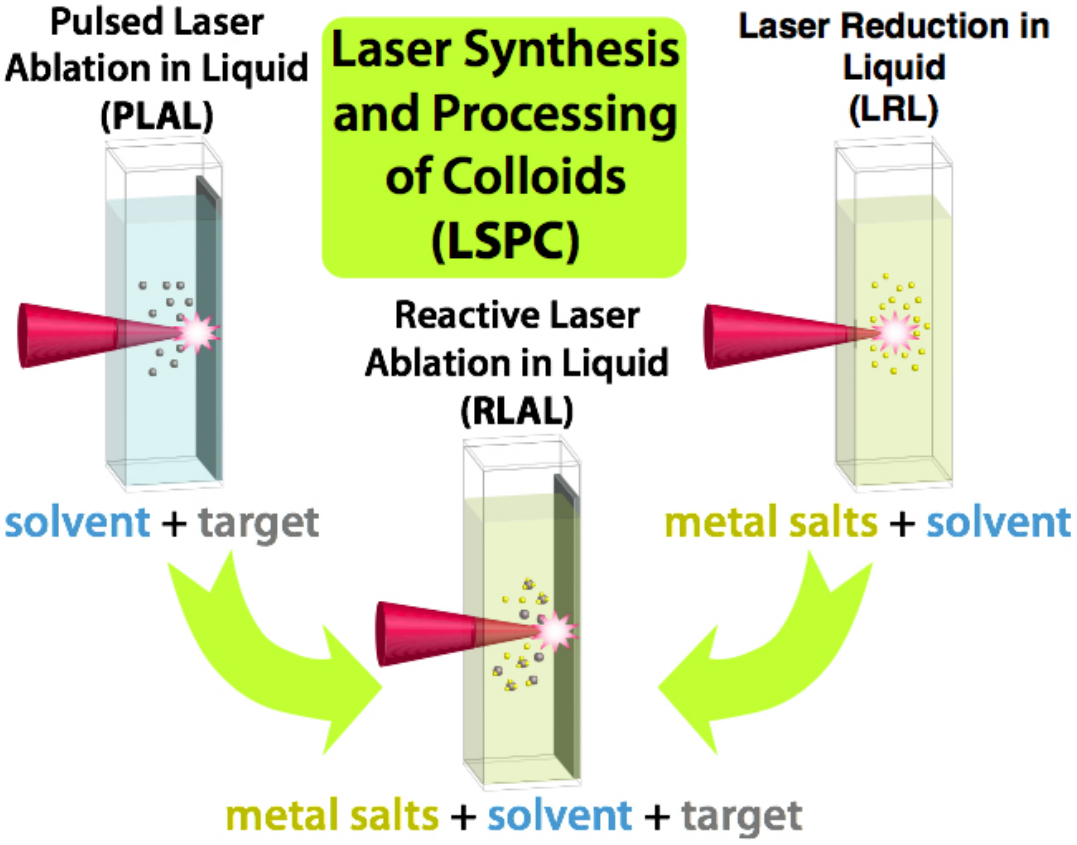

Figure 1.1: Diagram of laser conditions used to synthesize colloidal nanomaterials.

1.2.2 Mechanism of Laser-Matter Interaction

Pulsed laser ablation involves complex physical and chemical processes, including heating, melting, species ejection, vaporization, plasma creation and expansion, and chemical reactions.[61–67] Key parameters that affect the ablation process and thus the nanomaterial product include both laser parameters (pulse duration, pulse wavelength, pulse repetition rate) and chemical properties (target material composition, liquid solution composition). When laser pulses are used to synthesize colloids in PLAL, the ablated target material that is dispersed into the liquid is the product, as shown in Fig. 1.1 (labeled PLAL). While the majority

of the ablated species in solution retain the chemical composition of the target material, a fraction of their surface becomes oxidized or reduced due to interaction with the liquid or from oxygen vacancies. These charges enable the colloids to be electrostatically stabilized in solution, and the surface defects are beneficial for catalytic applications.[36,43,68] PLAL may be carried out using fs, picosecond (10^{-12} s, ps), nanosecond (10^{-9} s, ns), and microsecond (10^{-6} s, μs) pulsed lasers, with the mechanism of material ablation dependent on the electron cooling time (electron-to-phonon relaxation time).[36] The electron cooling time is material-dependent, typically on the order of several ps (Au: $3-4$ ps[69], Cu: $1-4$ ps[70], Si: 0.35 ps[71], ZnO: 0.5 ps[72]). Because the electron-to-phonon relaxation time is shorter than the ns pulse duration, ns-PLAL ablation depends strongly on the properties of the material, and follows a thermal mechanism of ablation which involves heating and melting of the target from the ns laser pulses. Fs laser pulses are shorter than the electron cooling time, and therefore the ablation process follows a solid−vapor transition.[73] Ps laser pulses are on the same order as the electron-to-phonon relaxation time and therefore may follow either the thermal mechanism or solid−vapor transition, depending on the pulse duration and material properties.[36]

The peak intensities reached with fs laser pulses are on the order of $10^{13}-10^{16}$ Wcm^{-2}, which exceed the ionization point of most dielectrics, and ionization of the surface target atoms occurs within a few fs.[36,47,74–77] Free electrons in metals (or electrons in the valence band of semiconductors or insulators) are the main species absorbing the pulse energy in the material, and gain even more energy due to inverse Bremsstrahlung (collisions with highly charged ions), which occurs within several ps. After the pulse energy deposition, isochoric (constant volume) heating occurs where transient temperatures of $5000-7000$ K are present in the laser-induced plasma, followed by the electron-to-phonon relaxation, involving energy transfer from the electrons to the crystal lattice in the form of vibrations. The free electrons generated gain enough energy exceeding the Fermi level of most materials, and are able to escape the crystal lattice. Left behind is an electron-deficient, highly charged surface, which drives Coulombic explosion of the target atoms due to the confined charge repulsion. The target atoms eject out of the solid material into the surrounding liquid, forming unique and metastable phases and structures including nanocubes, nanodiamonds, and thermodynamically metastable crystal structures of TiO_2, Si, and Ge due to the rapid cooling from solution mixing.[36,61,78–84] Synthesis of NPs from PLAL of Au targets have resulted in bimodal size distribution of the Au NPs in solution, where the photon-based nonthermal ablation led to

the formation of small Au NPs, while larger, 3−10 nm Au NPs of poor size distribution were generated from the plasma-related thermal ablation process.[41,61] Laser parameters such as energy and pulse repetition rate have been identified as improving the size distributions of colloidal Au NPs generated from this method.[85,86] The size and size distribution of metal NPs generated from PLAL can be further optimized by modifying the solution composition (pH, ionic strength, addition of capping agents).[36,41,87,88]

Alternatively, LRL is a more recent laser-assisted technique to synthesize metal NPs in solution, and is based on the generation of reducing species from solvent photolysis.[46] The peak intensities reached using fs laser pulses (10^{13}−10^{16} Wcm^{-2}) are sufficient to induce multiphoton ionization of water molecules, forming a dense localized plasma in a process called optical breakdown (OB).[89,90] The formation of OB plasma in water involves a number of reactions including[57,91–95]

$$H_2O \xrightarrow{nh\nu} e^- + H^+ + OH\cdot \tag{1.1}$$

$$e^- \longrightarrow e^-_{aq} \tag{1.2}$$

$$e^-_{aq} + OH\cdot \longrightarrow OH^- \tag{1.3}$$

$$H_2O \xrightarrow{nh\nu} H\cdot + OH\cdot \tag{1.4}$$

$$2\,OH\cdot \longrightarrow H_2O_2 \tag{1.5}$$

$$H\cdot + H_2O \longrightarrow H_3O^+ + e^-_{aq}. \tag{1.6}$$

These reactions have been widely found to enable the photochemical reduction of metal ions in solution to form metal NPs in the absence of chemical reducing agents.[45–47,49–51,56,57,96] Figure 1.1 displays the laser and colloids formed under LRL conditions (labeled LRL). Although hydrated electrons and H_2O_2 are particularly well-suited for photochemical conversion of Au(III) ions to Au NPs due to an autocatalytic reduction process[46,47,49], the formation of H_2O_2 hinders the ability to apply this technique to fabricate uncapped, colloidally stable NPs of other metals because H_2O_2 acts as a strong oxidant. For instance, Ag^0 and Cu^+ back-oxidize to Ag^+ and Cu^{2+} respectively, in the presence of H_2O_2[97,98], which inhibits the formation of NPs via photochemical reduction of Ag^+ or Cu^{2+} in an OB plasma.[96,99]

Due to the well known back-oxidation of metals to cations ($M^0 \rightarrow M^{n+}$) in the presence of H_2O_2 formed from water photolysis, addition of hydroxyl radical scavengers (secondary

alcohols) or stabilizers have been used to reduce the metal ions.[47,100] Preparation of metal NPs in an OB plasma has also been made possible with the addition of other species to the metal salt precursor, including TiO_2 sodium citrate, and surfactants such as sodium dodecylsulfate (SDS).[101,102] In addition to modifying the chemical composition of the precursor solution to synthesize metal NPs from fs-LRL, laser parameters such as the laser focus, pulse energy, and irradiation time have been used to control the metal NP size, shape, and morphology. In a recent demonstration, the focus of a beam was adjusted from a tight focusing geometry to a collimated beam, which modified the density of free electrons in the plasma. As a result, size of Au NPs in the tight focus increased from 3.5 nm to 27 nm when the beam was collimated.[74] The solution pH also affects the metal NP product morphology, and in another experiment the size distribution of LRL-Au NPs improved from 8.6±6.7 nm at pH 5.2 to 9.5±4.5 nm at pH 9.3.[74] These examples demonstrate the broad range of laser and chemical parameters that may be modified to control the size, shape, and morphology of metal nanoparticles and nanostructures synthesized from PLAL and LRL.

1.2.3 Reactive laser ablation in liquid

The previous section discussed the mechanisms involved in generating nanostructured materials using PLAL and LRL from ultrashort, intense laser pulses, and the experimental parameters used to control the morphology and composition of the products. In this section, the laser-assisted method referred to as Reactive Laser Ablation in Liquid (RLAL) will be discussed, which combines both the top-down and bottom-up approaches to nanomaterial synthesis into one step, as displayed in Figure 1.1, labeled RLAL. When PLAL is conducted in a liquid containing species that interact with the ablated target atoms to form a material of different chemical composition to the target, it is called RLAL. The first demonstration of RLAL in 2008 produced silica-capped Ag and Au NPs by ablating a silicon wafer immersed in either $Ag(NO_3)$ or $HAuCl_4$ aqueous solutions.[103] Since this initial work, many metastable and unique bi- and multi-metallic nanostructures have been reported. For instance, mixed-metal Pt-Co and Pt-Co-Cu oxide NPs for fuel cell applications were synthesized by ablating a Co target immersed in Pt and Cu metal salt solutions, and Ni-Fe layered hydroxides doped with Ti and La for electrochemical water splitting were synthesized by ablation of Fe powder in aqueous solutions of Ni, Ti, and La salts.[15,22,104–106] Complex metal-oxide mineral phases of copper and zinc were synthesized by RLAL of Zn or Cu targets immersed in aqueous Zn

or Cu salt solutions, and silica-supported Au or Ag nanomaterials have been synthesized by ablating silicon wafers in aqueous gold or silver salt solutions.[103,107–110] Significant development of highly functionalized nanostructures has been made in the field of RLAL. However, the above examples of the composite nanomaterials generated used nanosecond laser pulses. As discussed in the previous section, the ablation mechanism of ns pulses follows a thermal mechanism, while that of fs laser pulses follows an ionization-Coulombic explosion mechanism, resulting in higher ablation efficiency than ns laser ablation. This field is very new, and very little research has been reported using fs laser pulses for RLAL to synthesize nanostructured metal-oxide materials. This work focuses on the synthesis and characterization of metal-oxide composite nanomaterials generated from fs-RLAL, and the structure-property relationships are investigated, leading to better understanding of the chemical components that affect the morphology and composition of silica-Au, silica-Cu, and silica-Ni nanostructures.

1.3 Catalytic Applications

The ligand-free, bare surfaces of laser-synthesized NPs and nanomaterials make them valuable reference materials for model catalytic reactions. For example, the catalytic reduction of para-nitrophenol by sodium borohydride was modeled using laser-synthesized Au NPs, and had better experimental fit compared to chemically synthesized Au NPs to kinetic models.[36,111]

Additionally, the simple and versatile fs-RLAL synthesis setup enables efficient exploration of various chemical and laser parameters that affect the product morphology and thus the catalytic properties.[36,37] In addition to the electrostatically stabilized NPs, when the nanomaterials are generated from ablation, the surface of the products contain high densities of structural defects, making them ideal catalysts.[36] Thus, the class of nanostructures synthesized via laser irradiation, both LRL and PLAL, exhibit properties that are beneficial for catalytic applications. The elements explored in this work were chosen for their reported applications in catalytic reactions. First, with the discovery that sub-5 nm diameter Au NPs supported on silica exhibited superior catalytic oxidation of CO to CO_2 than Au NPs of larger diameters, researchers have investigated this structure-activity relationship for decades.[10,112,113] Next, the motivation to fabricate catalytically active materials made up of

earth-abundant elements led to the development of the silica-Cu and silica-Ni nanostructures. Specifically, the hydrogenation of CO_2 to carbon-containing feedstocks is an important reaction due to the abundance of CO_2 in our atmosphere that is contributing to global changes in weather.[114] Silica-Cu and silica-Ni nanostructures are known to selectively convert CO_2 to methanol and methane, respectively. By synthesizing silica-Cu and silica-Ni nanostructures using fs-RLAL, the product materials may be used as reference materials to investigate the specific bonding sites that contribute to the selectivity of these element-specific products.[24]

Chapter 2

Femtosecond-Reactive Laser Ablation in Liquid

2.1 Materials and Methods

Materials Silicon wafers (n-doped, (111)-oriented, single side polished, 300 μm thick, NOVA electronic materials), potassium tetrachloroaurate ($KAuCl_4$, STREM), potassium hydroxide (KOH, Fisher), copper(II) nitrate ($Cu(NO_3)_2$, Fisher), nickel(II) nitrate ($Ni(NO_3)_2$, Fisher), and nitric acid (HNO_3, Fisher) were used as received. Stock and working solutions were prepared with purified water from a Millipore Ultrapure water system (resistivity is 18.2 $M\Omega cm^{-1}$ at 25°C).

2.1.1 Sample Preparation

Ch. 3: Silica-Au Samples

Working solutions containing $[AuCl_4]^-$ (0.1 mM) and KOH (0.55 mM) were prepared from stock solutions (25 mM $KAuCl_4$ and 200 mM KOH), using Millipore Ultrapure filtered water. The working solution was prepared 18−24 hr before carrying out experiments and stored at 6°C. For each sample, 3.0 mL of the working solution was transferred to a 10×10×40 mm quartz fluorimeter cuvette containing a micro-stir bar (Fisher Scientific) and equilibrated to room temperature. The solution pH was measured to confirm it was 10.0±0.4, and a pre-cut silicon wafer was placed inside the cuvette and secured against one side. For synthesis of Au NPs via LRL, the working solution was transferred to a quartz cuvette without a silicon wafer, and irradiated following the conditions outline in section 2.3.

For the fs-RLAL samples, UV-vis measurements were taken to confirm complete conversion of the precursor $[AuCl_4]^-$ solution to nanoparticles, with an irradiation time of 9 min required for complete conversion. UV-vis spectra of the sample after incremental laser irradiation times are displayed in Figure 2.1a. Further details of determining the irradiation time for the silica-Au NPs are provided in Appendix A.

Synthesis of Au NPs from LRL were carried out in a home-built in situ UV-vis spectrometer as described in section 2.3. The cuvette containing 3.0 mL of the working solution were irradiated with laser pulses focused into the solution. UV-vis measurements were recorded to confirm full conversion of the $[AuCl_4]^-$ to Au NPs in 10 min, and the final UV-vis spectrum is displayed in Figure 2.1b. Further details of determining the irradiation time for the controlAu NPs are provided in Appendix A.

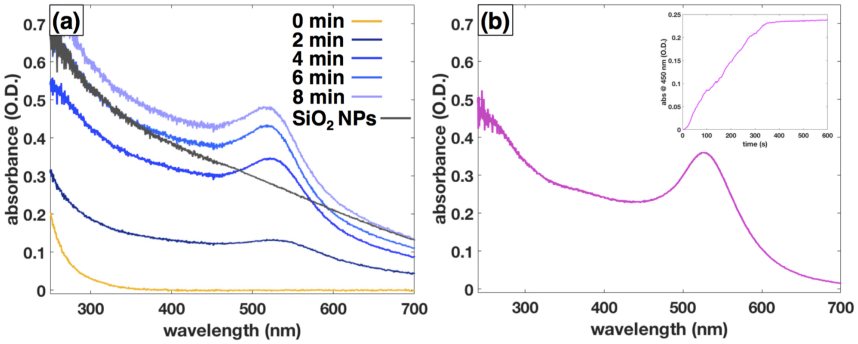

Figure 2.1: UV-vis spectra of silica-Au NPs after incremental laser irradiation and spectrum of silica (SiO_2) NPs generated from ablating a Si wafer in water for 8 min. (a) Final spectrum of control Au NPs; inset shows in situ UV-vis absorbance recorded at 450 nm to show growth of Au NPs (b).

Post-irradiation Sample Processing

The silica-Au NPs were centrifuged using a Fisher Scientific accuSpin Micro17 microcentrifuge. The as-synthesized samples were centrifuged for 30 min at 5,000 rpm, the pellet was washed with water and centrifuged for an additional 30 min at 5,000 rpm. For TEM imaging, the concentrated pellet was diluted and drop cast on a carbon coated copper TEM grid (Ted Pella) and let dry under ambient conditions. For SEM-EDX and XPS analysis the concentrated pellet was drop cast on conductive carbon tape and let dry at room temperature under vacuum. For para-nitrophenol (PNP) reactions, the as-synthesized silica-Au or Au NPs was added to the reaction flask. Further detail on this is provided in Section 2.4 and in Appendix A.

Ch. 4: Silica-Cu Samples

Working solutions of $Cu(NO_3)_2$ (2.0 mM) were prepared from a freshly prepared aqueous stock solution (50 mM) and the pH was recorded as ~5.4. Either HNO_3 (1.0 mM) was added from a 10 mM stock solution or KOH (5.0 mM) was added from a 200 mM stock, resulting in working solution pH values of 3.0 and 10.4, respectively. The working solution was transferred to a 10×10×40 mm quartz cuvette (3.0 mL) equipped with a stir bar, and a pre-cut silicon wafer was placed in a glass cuvette and secured to one side. Table 2.1 displays the solution composition, sample name, and initial solution pH for the samples discussed in Chapter 4.

Sample Name	mM $Cu(NO_3)_2$	mM HNO_3 or KOH	Initial pH
Cu-silica-3.0	2	1.0 mM HNO_3	3.0±0.1
Cu-silica-5.4	2	0	5.4±0.6
Cu-silica-10.4	2	5 mM KOH	10.4±0.2

Table 2.1: Sample names and solution composition.

fs-RLAL irradiation of the Si wafer immersed in the working solution was conducted for 30 min while stirring (details of laser parameters in section 2.2), followed by centrifugation for 15 min at 6,000 rpm (Thermo Fisher AccuSpin Micro 17). The supernatant was replaced with water and centrifuged a second time for 15 min at 6,000 rpm. The pellet was diluted in water and drop cast onto a carbon coated copper grid for TEM analysis. For SEM-EDX and XPS analysis, the concentrated pellet was drop cast onto conductive carbon tape and let dry under vacuum at room temperature. The pellet was dried under vacuum at room temperature and collected for XRD, FTIR, and ICP-OES analysis. For the PNP catalytic reactions the concentrated pellet was redispersed in 3 mL water and tested for its catalytic activity.

Ch. 5: Nickel-Phyllosilicate Samples

Working solutions were prepared directly in a 15 mL 10×40×40 mm glass cuvette from $Ni(NO_3)_2$ (50 mM) and KOH (500 mM) stock solutions. The cuvette was equipped with a stir bar and a precut silicon wafer (NOVA electronics). Table 2.2 displays the sample name and the solution composition of all samples prepared. After irradiation was complete, the solution pH was recorded, and the sample was centrifuged for 90 min at 13,000 rpm, washed with water and repeated. The supernatant was collected for characterization with

ICP-OES, and the pellet was collected and dried at room temperature under vacuum for characterization. For TEM imaging, one drop of the pellet was diluted to 1.0 mL water, and drop cast onto a carbon-coated copper grid. The remaining pellet was dried under vacuum at room temperature and the powder was collectd for XRD, and FTIR analysis, and was deposited on conductive carbon tape for SEM-EDX, and XPS analysis.

Sample Name	mM $Ni(NO_3)_2$	mM KOH	Initial pH
silica-5.9	0	0	5.9±0.05
silica-7.8	0	0.02	7.8±0.45
silica-10.3	0	0.2	10.3±0.04
silica-11.7	0	5	11.7±0.01
silica-Ni-5.9	2	0	5.9±0.01
silica-Ni-8.3	2	1	8.3±0.06
silica-Ni-10.6	2	5	10.6±0.10
silica-Ni-11.8	2	10	11.8±NA

Table 2.2: Sample names and solution composition prepared in this work.

2.2 Instrumentation

Laser irradiation was performed using a titanium-sapphire-based chirped-pulse amplifier (Astrella, Coherent, Inc.) delivering 7 mJ, 30 fs pulses with bandwidth centered at 800 nm at a 1 kHz repetition rate. The pulse energy was adjusted to 50−200 μJ with a zero-order $\lambda/2$ waveplate (ThorLabs, Inc.) and broadband thin-film polarizer (Altechna), as well as a dispersion compensated 90:10 (R:T) beamsplitter (Newport, Inc.).

Two focusing conditions were used for the different experiments carried out, and described below.

Laser Ablation in Liquid Conditions

For fs-RLAL samples, the silicon wafer in the cuvette was placed approximately 10 mm before the focal point of a f = 50 mm lens. The high-numerical aperture lens ensures that no filamentation occurs on the window of the cuvette or in the aqueous solution prior to interaction with the Si wafer. The ablation spot size was 85 μm in diameter based on the measurement of an ablated Si wafer with an optical microscope.

For the silica-gold NP synthesis, the pulse energy was attenuated to 50 μJ, corresponding to a laser fluence of 0.88 J cm^{-2}, and a peak intensity of 2.9×10^{13} W cm^{-2}. The silica-Cu

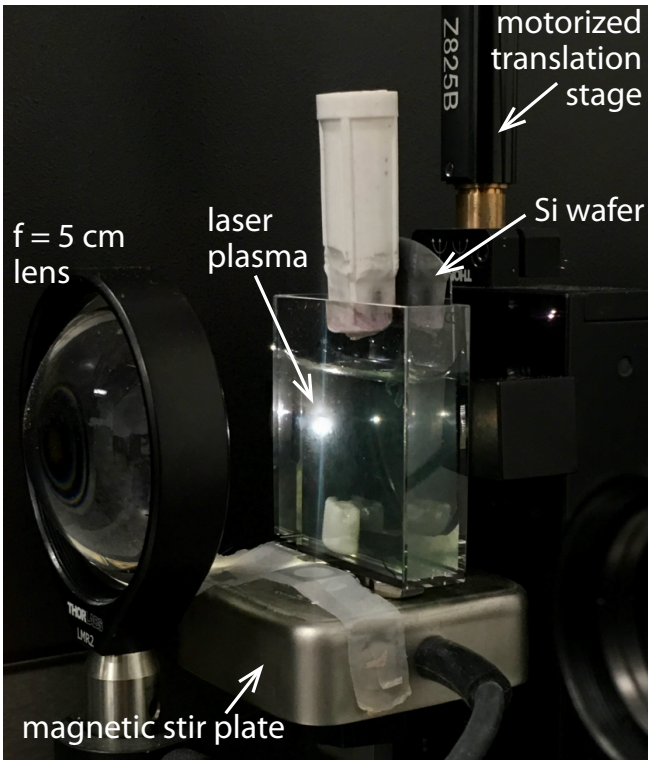

Figure 2.2: fs-RLAL setup.

and silica-Ni samples were generated using 200 μJ pulses, corresponding to a laser fluence of 3.5 J cm^{-2} and an intensity of 1.2×10^{14} W cm^{-2}. The sample cuvette was placed on a miniature stir plate (Thermo Scientific) mounted to x- and y- motorized translation stages (Thorlabs). The stages were mounted on a manually controlled z-direction stage (Thorlabs), which was adjusted to focus the laser beam onto the Si wafer. The cuvette was translated in the x- and y- directions at a rate of 0.5 mm/s during the irradiation experiments to move the laser focus across the Si wafer. Figure 2.2 displays an image of the fs-RLAL experimental setup.

Laser Reduction in Liquid (LRL) Conditions

The 11 mm (1/e^2) diameter laser beam out of the laser was expanded to a diameter D = 29 mm (1/e^2) prior to focusing with a f = 50 mm aspheric lens (Figure 2.3a). The resulting focusing geometry is f/1.7, which is similar to the tightest focusing condition with a microscope objective reported in ref[115] and is significantly tighter than other recently reported focusing geometries for Gaussian beams.[116,117] The beam waist and Rayleigh range in air were measured with a CCD camera (ThorLabs, Inc.) to be w_0 = 6.52 μm and z_r = 77.7

μm, respectively. The calculated peak irradiance at the focus (neglecting losses and plasma-induced defocusing in front of the focus[115,118,119]) was 1.25×10^{15} W cm^{-2}, and a fluence of 34.7 J cm^{-2}.

The laser beam was passed through at 10×10×40 mm quartz fluorescence cuvette containing the prepared $KAuCl_4$ working solution (cf. section 2.1.1). The working solution was irradiated for 10 min for sufficient conversion of the $[AuCl_4]^-$ to Au NPs. To monitor the kinetics of $[AuCl_4]^-$ reduction during irradiation, the irradiation experiments were carried out in a home-built in situ UV-vis spectrometer consisting of a stabilized deuterium tungsten light source (Ocean Optics, DH2000-BAL), optical fibers, two pairs of off-axis parabolic mirrors, and a compact spectrometer (Ocean Optics, HR4000), see Fig. 2.3. The UV-vis spectrum of the irradiated solution is provided in Fig. **??**b along with the absorbance at 450 nm over time, representing the formation of Au^0.

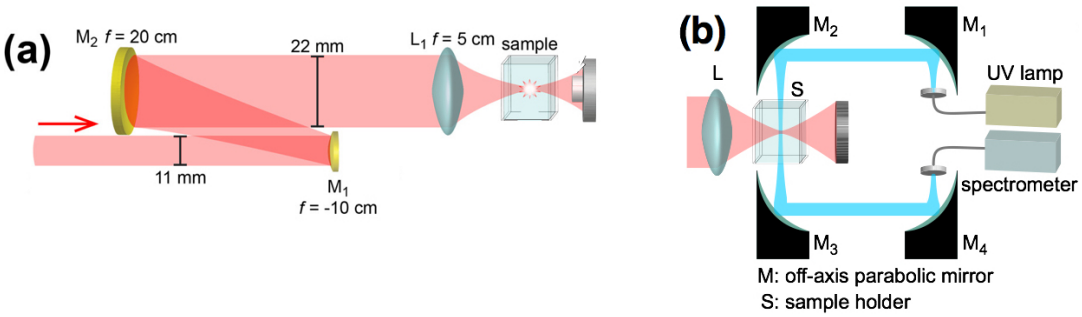

Figure 2.3: Diagram of laser setup for PCR (a). Home built in situ UV-vis experimental setup for PCR experiments (b).

2.3 Characterization

Transmission Electron Microscopy (TEM) TEM images were collected on a JEOL JEM-1230 TEM at 120 kV. High resolution TEM (HRTEM) images and SAED patterns were collected on an FEI Titan 80 300 kV with a Gatan 794 Multi-Scan Camera. Samples were prepared by drop-casting the diluted or re-dispersed powder pellet onto a carbon-coated copper grid (100 mesh, Ted Pella, Inc.) and left to dry for at least 24 hr at room temperature. Size distributions were determined by measuring 300 individual particles from three separate parts of the grid using ImageJ software. Gatan Microscopy Software Suite version 3.x was

used to determine the crystal lattices of the nanoparticles in the HRTEM images. Details on this process are described in the Appendix B.

Scanning Electron Microscopy-Energy Dispersive X-ray Spectroscopy (SEM-EDX) SEM-EDX was carried out on a Hitachi FE SEM SU-70 (spatial resolution 1.0 nm) equipped with an Energy Dispersive X-ray Spectroscopy (EDX) detector. Images were obtained at 10 keV and elemental analysis was conducted at 20 keV, with ZAF standardless quantification employed for EDX measurements. Samples were prepared by either drop casting the centrifuged pellets or dispersing the dried powder pellets onto conductive carbon tape stabilized on an aluminum stage, and drying under vacuum at room temperature.

X-ray Diffraction (XRD) XRD was conducted on a Panalytical Empryrean Diffractometer with CuKα radiation (λ = 0.15418 nm) at 40 kV and 45 mA, with scanning angle (2θ) of 10−90° and a gonio focusing geometry. Samples were prepared for XRD analysis by drying the centrifuged pellet under vacuum at room temperature and collecting the dried powder.

X-ray Photoelectron Spectroscopy (XPS) XPS was conducted on a PHI VersaProbe III Scanning XPS Microprobe with a monochromatic Al kα X-ray source (1486.6 eV) run at 25 W and 15 KV, with a pass energy set to 112 eV for survey scans and 69 eV for high resolution spectra. A spot diameter of 100 μm was irradiated using a take off angle of 90°, and a detector was situated at an angle of 45°. Charge neutralization was achieved by employing an ion gun and a flood gun during the analysis. Samples were prepared by either drop casting the centrifuged pellet or depositing the dried powder onto conductive carbon tape. Sample analysis was carried out using CasaXPS Software version 2.3.19PR1.0, employing Gaussian and Lorentzian convolution to fit the spectral lines, and all high resolution spectra were corrected by shifting the C1s peak at 284.8 eV.

Fourier Transform Infrared Spectroscopy (FTIR) FTIR analysis was conducted on a Nicolet iS50 FTIR spectrometer equipped with a mid- and far- IR-capable diamond ATR. Spectra were obtained using 32 scans in the range of 4000 to 400 cm^{-1} with 5 cm^{-1} resolution. Samples were prepared for FTIR analysis by drying the centrifuged pellet under vacuum at room temperature and collecting the dried powder.

Inductively Coupled Plasma-Optical Emission Spectroscopy (ICP-OES) ICP-OES was carried out on a Varian VISTA-MPX inductively coupled plasma optical emission spectrometer. Analysis of elements (Cu, Au, Si) was achieved by digesting the dried pellet in

a 1:1 H_2O:HNO_3 solvent and sonicated overnight. Elements were quantified against an external calibration curve prepared from 1000 ppm stock standard solutions of Au, Cu, and Si (Inorganic Ventures). Analysis of Ni content in the supernatant (Section 5) was achieved by centrifuging the as-prepared samples at 13,000 rpm for 90 min followed by filtering of the supernatant solution through a 0.22 μm cellulose filter, and dispersed in 6 v/v% HNO_3 in water.

Electrospray Mass-Spectrometry (ESI-MS) ESI-MS data were run in the Mass Spectrometry facility at VCU. The spray voltage was operated at 3.5 V using a flow rate of 0.7 μL/min. Data was collected using LTQ-Tune and visualized with Qual Browser (Thermo XCalibur software). Samples were prepared by filtering (0.22 μm cellulose) the supernatant (13,000 rpm for 90 min) and mixing 1:1 with acetonitrile.

2.4 Para-nitrophenol Reduction Catalytic Reactions

2.4.1 Materials and Methods

Sodium borohydride ($NaBH_4$, Acros Organics) and para-nitrophenol (PNP, Acros Organics) were used as received. Stock and working solutions were prepared with purified water from a Millipore Ultrapure water system (resistivity is 18.2 MΩcm^{-1} at 25°C).

The catalytic reduction of para-nitrophenol (PNP) by $NaBH_4$ was carried out in a home-built in situ UV-vis spectrometer. In a typical catalytic run, the catalyst was was either used as prepared (silica-Au, Au NPs, Section 3.3), or the centrifuged pellet was redispersed in 3.0 mL water (silica-Cu samples, Section 4.3.1), and 300 μL of the catalyst solution was added to a cuvette containing PNP (0.1 mM) and $NaBH_4$ (10 mM) while stirring. The PNP was added from a stock solution (1.5 mM) and the $NaBH_4$ was added from a freshly prepared stock solution (100 mM). The absorbance at 400 nm (as the para-nitrophenolate ion) was recorded, and the reaction was considered complete when it had disappeared completely. Data processing for the PNP reaction was conducted based on the methods of Ref.[120] and details are provided in Appendix A.

2.4.2 Instrumentation

The PNP catalytic reactions were carried out in second a home-built in situ UV-vis spectrometer consisting of a deuterium-tungsten lamp (Ocean Optics, DH2000-DUV), a sample

holder for 10×10×40 mm cuvettes placed on a stir plate, and a compact spectrometer (Ocean Optics, USB4000) connected via optical fibers. Spectra were recorded once per 1.2 s using LabVIEW software (National Instruments). A figure of the experimental setup, UV-vis spectra over time, and details on calculating the apparent rate constant are provided in Appendix A.

Chapter 3

Silica-Gold Nanostructures

In this chapter the synthesis conditions and reaction timescales for fs-RLAL of silica-Au NPs are explored. By combining the 'bottom up' approach of generating Au NPs with the 'top down' method of laser ablation to generate silica nanomaterials into one step, silica-stabilized Au NPs are fabricated. The timeline of reactive species generated in the ablation plasma will be discussed to describe the morphology and composition of the silica-Au NPs formed from fs-RLAL.

3.1 Background and Motivation

Supported gold nanocrystals were identified to be highly effective catalysts for CO oxidation at very low temperatures in the 1980's, initiating intense research in understanding both the synthesis conditions for optimizing the catalytic activity of oxide-supported Au nanocrystals and understanding the active sites for this low-temperature catalytic reaction.[113,121] While the most active support materials included TiO_2, CeO_2, and Fe_2O_3, silica has also been investigated due to its inert chemical properties, to isolate the Au nanocrystals' activity toward the CO oxidation reaction.[122] Laser-assisted synthesis of nanomaterials are advantageous for exploring bonding environments and active catalytic sites due to their stability without added surfactants. Preparing silica-Au NPs from fs-RLAL by ablating a silicon wafer immersed in $[AuCl_4]^-$ solutions and comparing the catalytic activity to Au NPs generated under LRL conditions may provide insight to the role that the silica support plays in the catalytic activity of silica-Au nanocomposites.

3.2 Morphology and Composition of Au-Silica Nanostructures

The silica-Au NP and control Au NP samples were visualized using TEM, with representative images displayed in Fig. 3.1 and in Appendix B. The silica-Au NPs in Fig. 3.1a show two distinct populations of particles; larger, often isolated particles (light blue arrow in Fig. 3.1a, 'isolated particles') and small particles within a matrix (dark blue arrow in Fig. 3.1a, 'stabilized particles'). The size distribution of the isolated particles was determined by counting particles that were separate from the silica matrix, yielding 7.0±2.0 nm (light blue histogram, Fig. 3.1c). To measure the size distribution of the stabilized particles, the as-synthesized sample was centrifuged under extreme conditions to separate out the isolated particles (10,000 rpm, 30 min). Fig. 3.1b shows a TEM image of the centrifuged pellet, where the small Au NPs remain dispersed within the silica matrix (dark blue arrow in Fig. 3.1b), while isolated Au NPs that were not removed during centrifugation agglomerated to form a chain-like structure (light blue arrow in Fig. 3.1b). In the centrifuged pellet, only particles visually found within the silica matrix were counted to obtain the size distribution of 1.9±0.7 nm (dark blue histogram, Fig. 3.1c). The control Au NPs in Fig. 3.1e were larger and more polydisperse, having a mean diameter of nm (Fig. 3.1f), and several nanotriangles were visible as well.

SEM-EDX was used to visualize the surface morphology of the sample and quantify the Au and Si present in the supernatant and centrifuged pellet portions of the silica-Au NP sample. Fig. 3.1d shows an SEM image of the centrifuged pellet, showing many spherical grey particles and amorphous structures decorated with white edges. Since the sample was not sputter-coated prior to imaging it is unclear whether the white portion of the image is due to the conductive Au present, or due to charging of the non-conductive silica. However, EDX analysis of the sample detected some gold (8.7 wt.%) and mostly silicon (76.8 wt.%), while the remainder of the sample contained oxygen (not reported). The supernatant contained more gold than the pellet did, with 44.6 wt.% Au and 12.3 wt.% Si (Fig. B2 in Appendix B; oxygen not reported). Control silica NPs were also analyzed with SEM-EDX, revealing similar surface morphology to the silica-Au NPs, and a small amount of gold present in the sample, likely from contamination in the cuvettes used (0.36 wt.% Au, 89.2 wt.% Si, Fig. B2b in Appendix B).

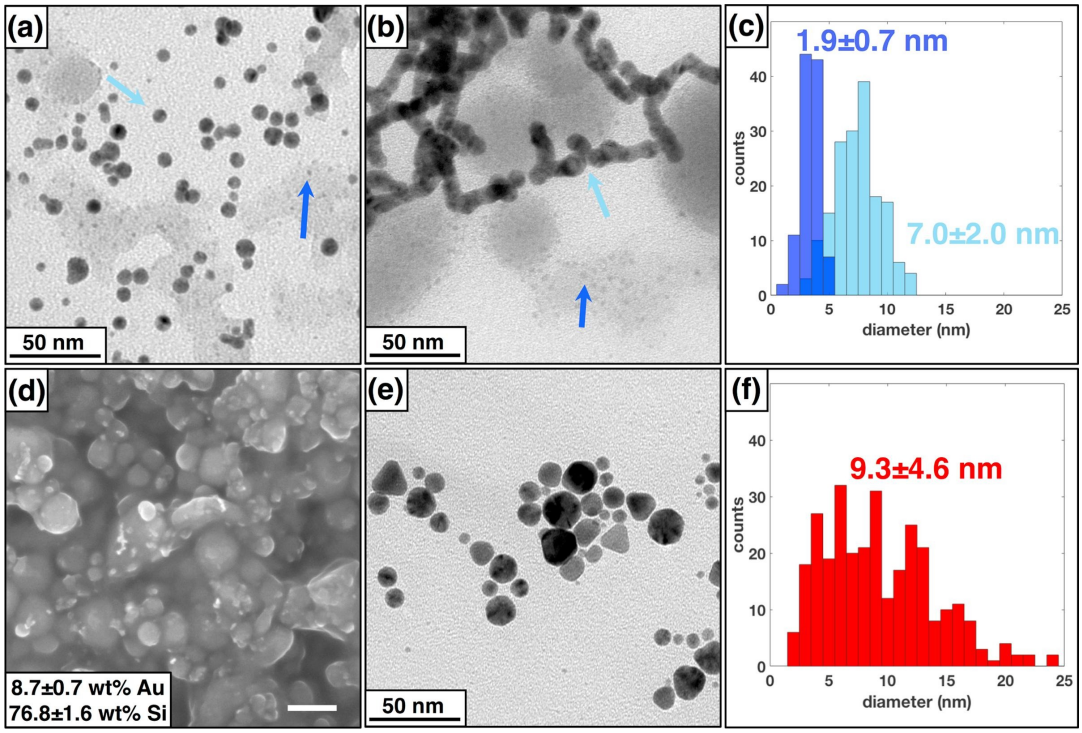

Figure 3.1: TEM image of as-synthesized (a) and centrifuged pellet (b) silica-Au NPs. Size distribution of as-synthesized silica-Au NPs (c). SEM image with EDX quantification of Si and Au in centrifuged pellet silica-Au NPs; scale bar represents 200 nm (d). TEM image of control Au NPs (e) with size distribution (f).

HRTEM analysis (Fig. 3.2a) shows polycrystalline particles, with lattice spacings corresponding to fcc-Au. Both populations of the silica-Au NPs are polycrystalline, as shown in the inset of the HRTEM in Fig. 3.2a. The spacings were measured to be 2.32 Å, 2.10 Å, and 1.45 Å, corresponding to the (111), (200), and (220) planes of fcc-Au. The matrix containing the small Au NPs appears to be amorphous, since no lattice spacings were observed. The control Au NPs were also polycrystalline, with the 2.44 Å, 2.35 Å, and 1.39 Å spacings corresponding to the (111) and (220) planes of fcc-Au. The fast Fourier transform (FFT) of the Au NPs within the red square of Fig. 3.2b confirms the fcc-Au pattern.

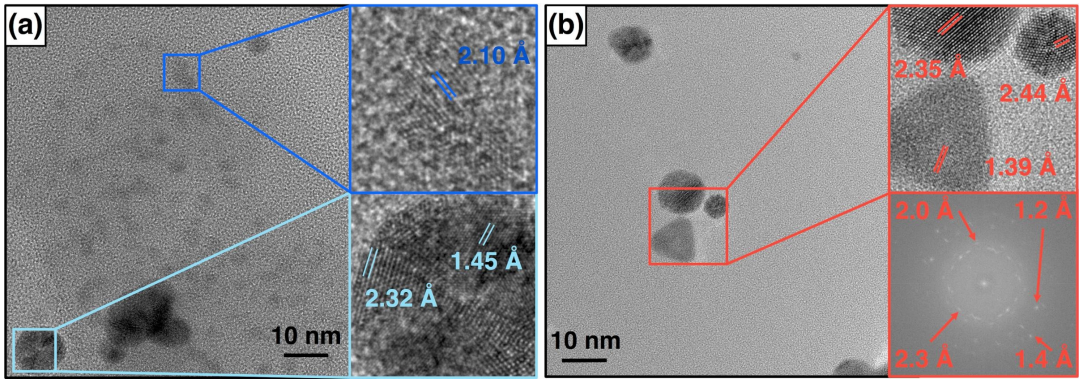

Figure 3.2: HRTEM image with lattice spacings for silica-Au NPs (a) and HRTEM image, lattice spacings and FFT of control Au NPs (b).

HAADF-STEM images of the silica-Au NPs revealed white spheroid particles and grey amorphous material, corresponding to gold and silica, respectively. Due to the significantly different atomic numbers between gold and silicon, it is possible to visually identify the two elements: the higher atomic number element has higher contrast (gold = white) than the lower atomic number element (silicon = grey) [47]. The EDX spectrum in Fig. 3.3a taken of an isolated Au NP (white particle) inside the red circle shows the presence of both Si and Au. While the area in the red circle appears to be all white, corresponding to Au, the Si detected could either be from surrounding Si in the matrix, or due to interstitial Si atoms within the Au crystal lattice. Since the XRD patterns of the silica-Au NPs and the control Au NPs match (Fig. 3.4), it is likely that the Si detected with EDX is predominantly from the amorphous silica near the free Au NP, although small amounts of interstitial Si in the Au NPs cannot be ruled out. In Fig. 3.3b, the EDX spectrum of a barely visible light particle inside the red circle contains mostly silicon and a small amount of gold, indicative of a small Au NP stabilized by a large amount of silica. This result is consistent with the small particles visible

in the TEM images in Fig. 3.1 and Fig. 3.2a of small Au NPs stabilized by a silica matrix.

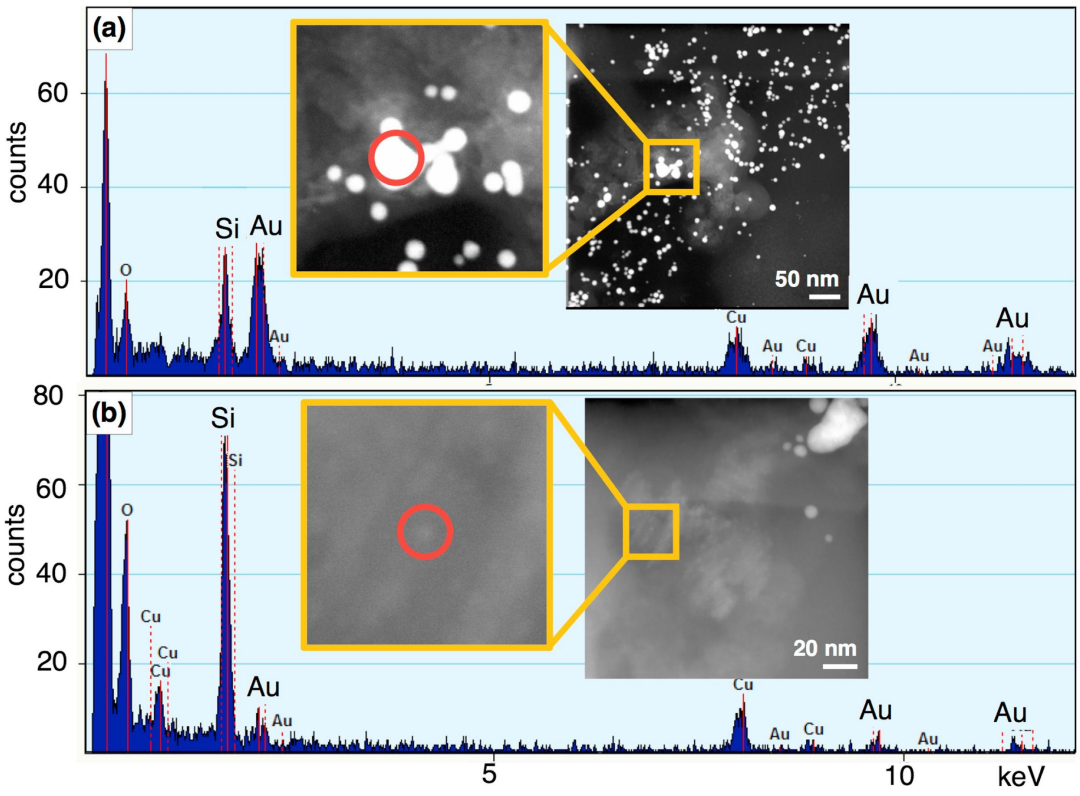

Figure 3.3: HAADF-STEM image of silica-Au NPs with EDX spectrum taken of portion inside red circle.

The XPS spectra from the Au4f, Si2p, and O1s atomic orbitals for the silica-Au NPs, control Au NPs, and control silica NPs generated from ablating a silicon wafer in water are displayed in Fig. 3.5; peak fittings with binding energies, atomic percentages, and suggested species are presented in Table 3.1. The Au4f spectra reveal both neutral Au^0 and oxidized surface Au atoms in the silica-Au NPs and control Au NPs. The 84.0 eV binding energy corresponds to bulk Au^0, while peaks at slightly lower binding energy near 83 eV represent low coordinated Au^0 atoms.[123–125] The control Au NP sample contained significantly more low coordinated Au^0 atoms than the silica-Au NP sample. The peak near 85 eV corresponds to partially oxidized Au atoms or low coordinated Au^{1+} atoms (Au^{1+}) in Fig. 3.5 and Table 3.1.[124] In addition to the Au^{1+} species, a peak at 85.8 eV was fit in the silica-Au NPs only, corresponding to as Au_2O_3 surface oxide species.[126] This oxidation state was not fit in the control Au NP sample.

The Si2p spectrum for the silica-Au NPs in Fig. 3.5b contains the expected peaks at 103.5 eV for SiO_2[128–130] and 99.4 eV for Si^0[128–130], with an additional peak at 98.0 eV,

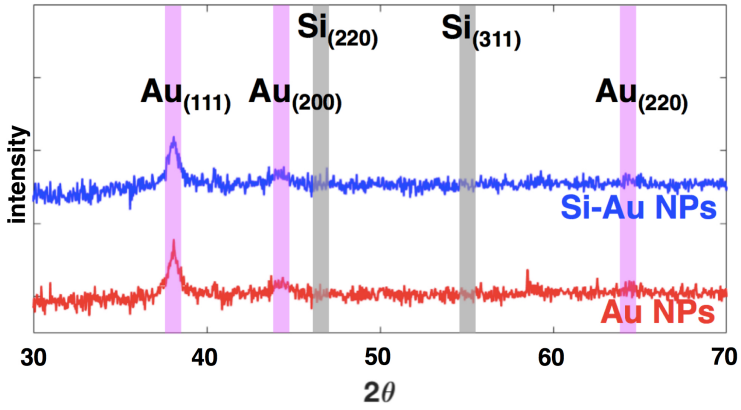

Figure 3.4: XRD patterns for silica-Au NPs (blue) and Au NPs (red). Peaks highlighted for Si (grey) and Au (pink) related spacings.

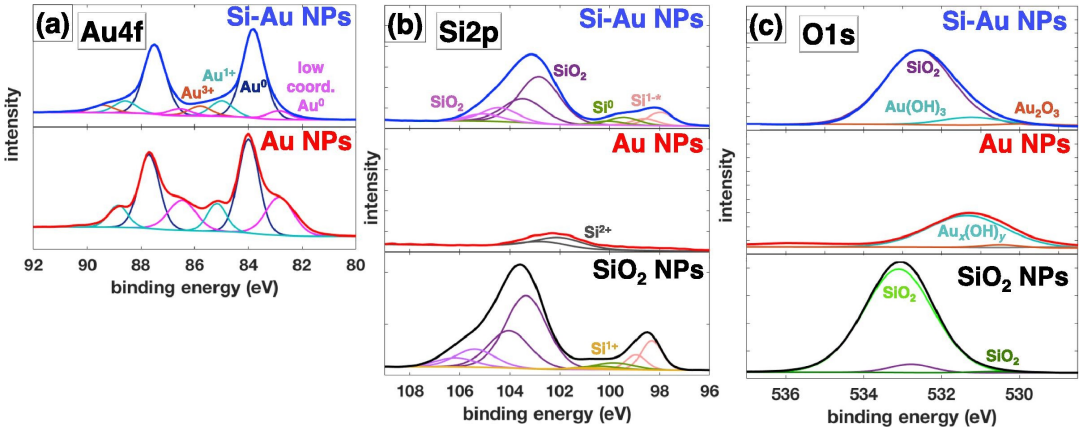

Figure 3.5: XPS spectra for Au4f (a), O1s (b), Si2p (c) atomic orbitals for silica-Au NPs (blue), Au NPs (red), and silica NPs (black) with fitted peaks.

Species	Silica-Au NPs	Au NPs	SiO_2 NPs	Bulk (reference)
Low coord. Au^0	82.9; 7%	82.8; 30%		83.3 eV [123–125]
Au^0	83.83; 72%	84.0; 55%		84.0 eV [123–125,127]
Au^{1+}	84.9; 13%	85.2; 15%		85.2 eV [124]
Au^{3+}	85.8; 8%			85.8 eV; [126]
Si^{1-*}	98.0; 11%		98.3; 13%	
Si^0	99.4; 8%		99.8; 6%	99.4 eV [128–130]
Si^{1+} (Si_2O)			100.9; 2%	100.5 eV [129–131]
Si^{3+} (Si_2O_3)		101.9; 100%		102 eV [129]
Si^{4+} (thin SiO_2)	102.9; 69%		103.4; 64%	102.6–104 eV [128–130,132,133]
SiO_2 (thick/quartz)	104.6; 12%		105.4; 15%	
Au_xO_y		529.0; 2%		529–530 eV [134]
Au_2O_3	529.8; 1%	530.5; 5%		530.2 eV [134]
$Au_x(OH)_y$	531.2; 9%	531.3; 93%;		531.2 eV[a] [134]
SiO_2 (amorphous)			530.7; 1%	530.7 eV [135]
SiO_2 (quartz)	532.6; 90%		532.8; 5%	532.9 eV [128,136]
SiO_2			533.1; 94%	533.2–534 eV [128,132,136–138]
Au–Cl	199; 100%	198.5; 100%		198.8–199.2 eV [136b]

Table 3.1: Binding energy (eV) and atomic percent of various species deconvoluted from XPS analysis. Binding energy values correspond to $Au4f_{7/2}$, $Si2p_{3/2}$, O1s, and $Cl2p_{3/2}$ peaks. *Suggested species not reported in literature. [a]Value reported for $Au(OH)_3$. [b] Binding energies reported for transition metal chloride compounds.

which has not been previously reported. Due to its proximity to the neutral Si^0 species, the peak at 98.0 eV is most likely in the form of Si^{1-}, since the Si^{1+} is shifted up by 1 eV from the Si^0 peak.[129–131] The presence of this putative Si^{1-} species is surprising due to the electropositive nature of Si, but the accessibility of metastable phases in the nonequilibrium environment formed at the plasma-water interface could enable the formation of such exotic species.[139–141] The large peak centered around 103.5 eV in the silica-Au NPs was fit with two peaks which are likely two types of silica species with different electronic structures[128,137], or silicon species with different oxide layer thicknesses.[129,138] The more abundant peak at 102.9 eV could be a thin oxide layer,[129] or it could be bound with gold particles, as reports with silica and colloidal Au may have a slightly lower binding energy to silica alone.[128] The peak at 104.6 eV is on the higher range of binding energies for silica, which could be due to a thicker oxide layer in[128] the matrix or the presence of large silica particles,[129,138] based on a recent report of 104.3 eV binding energy of a 200 nm thick layer of silica.[138] Alternatively, the higher binding energy peak may arise from quartz based on previous XPS studies.[128,142] The control silica NPs synthesized in water contain the same peaks in the Si2p spectrum, confirming that these species are formed from laser ablation of the silicon wafer in liquid,

regardless of the presence of metal salt. A small peak (2%) corresponding to Si^{1+} [129–131] was also present in the control silica NPs; the other peaks are shifted to slightly higher binding energies compared to the silica-Au NPs. [138] This could also be due to the general oxide layers being thicker [129,138] or due to the absence of Au NPs. [128] Gross *et al.* studied binding energy shifts of silica with and without colloidal gold, and found that with quartz species, the Si2p binding energy shifted down slightly when colloidal gold was present, while silica gel exhibited no binding energy shift whether the gold was present or not. [128] TEM, HRTEM, FFT and lattice spacing measurements of the control silica NPs (Fig. 3.6, more details in Appendix B) show two populations of silica: amorphous and polycrystalline particles. This reflects the two deconvoluted peaks in the Si2p spectrum, although it is difficult to assign peaks to the different morphologies, due to overlapping binding energies reported for the different silica species. [127,128,132,137,138] The weak Si2p signal in the control Au NP sample may be partially oxidized Si species arising from contamination from the quartz cuvette used for irradiation experiments.

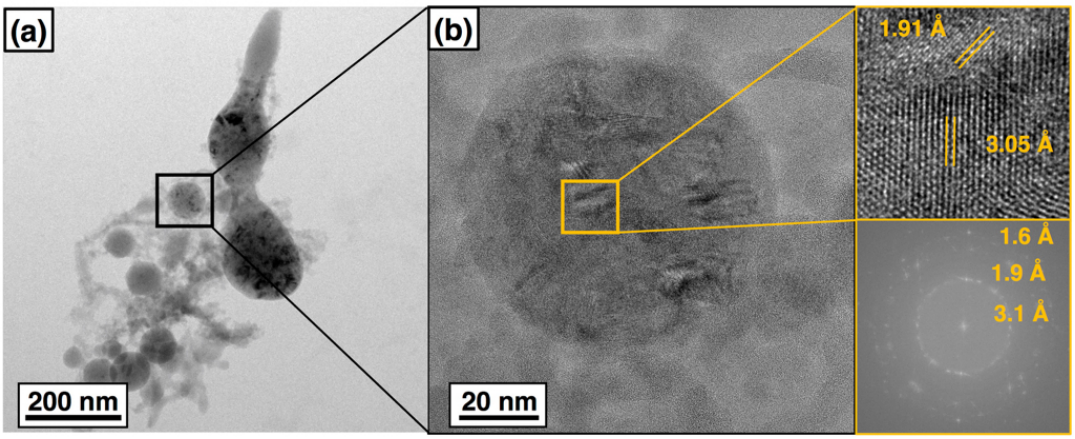

Figure 3.6: TEM images of silica NPs generated from ablating a silicon wafer immersed in water (a). HRTEM with FFT and lattice spacings of silica NPs (b).

The O1s spectra in Fig. 3.5 show that most of the O1s surface species in the silica-Au NPs is from silica, [136,137] and a small percentage from oxidized gold (Au_2O_3 and $Au(OH)_3$). [134] The binding energy assigned to SiO_2 at 532.6 eV matches closely to that reported by Gross *et al.* for quartz with colloidal gold (532.7 eV), and is close to the reported value for crystalline quartz. [135] Although the HRTEM image for the silica-Au NPs (Fig. 3.2a) does not contain any crystalline silica species, XPS analysis can identify species not visible with electron

microscopy imaging. The control Au NPs contain mostly oxidized gold species, corresponding to surface hydroxides. The binding energy at 531.3 eV is close to that of $Au(OH)_3$,[134] giving the surface gold atoms a Au^{3+} oxidation state that was not detected in the Au4f spectrum for the control Au NPs. Partial oxidation of the gold surface atoms is likely the case. Three peaks were deconvoluted in the control silica NPs O1s spectrum, with a small (1%) amount corresponding to that of amorphous silica,[135] and the other two in the range of silica species.[128,129,132,136,138] The peak at 532.8 eV closely matches reported binding energy values for quartz (532.7 eV[135]), while the majority of the O1s signal comes from the peak deconvoluted at 533.1 eV, which is close to the 533.2 eV binding energy reported for silica.[128,129,132,136,138] It is difficult to assign species based on the Au4f, Si2p, and O1s XPS spectra due to overlapping binding energies reported. However, we hope to demonstrate the multiple types/populations of silica generated from our fs-RLAL approach.

The Cl2p binding energies are presented in Table 3.1, and the spectra are displayed in Appendix B, Fig. B4 The peaks correspond to metal chlorides, likely from the $KAuCl_4$ precursor.[136]

3.3 Catalytic Reduction of Para-Nitrophenol

The catalytic reduction of para-nitrophenol (PNP) to para-aminophenol (PAP) by sodium borohydride is a common model reaction to test the catalytic activity of metal nanoparticles.[111,120] This reaction was used to compare the as-synthesized silica-Au NPs to the control Au NPs, to see if the added silica support enhanced the catalytic efficiency compared to control Au NPs. Table 3.2 displays the size, specific surface area (SSA), and catalytic rate constants comparing the silica-Au NPs and the control Au NPs synthesized in this work. The 6.17 nm diameter of the Au NPs in the silica-Au NP sample was weighted by assigning the Au quantified from SEM-EDS analysis of the centrifuged pellet to the stabilized Au NPs (1.9 nm, 8.7 wt%), and the amount of Au detected in the supernatant to the isolated particles (7.0 nm, 44.6 wt%). Calculations for the weighted mean diameter and other values reported in Table 3.2 are provided in the Appendix B.

The rate constant is normalized to the moles of Au added to the experiment, reflecting the efficiency of Au atoms present in the nanocatalysts independent of the size dispersity, while the SSA-normalized rate constant depends on available surface sites driving the PNP reaction.

Property	Silica-Au NPs	Control Au NPs
size (nm)	6.17[a]	9.3±4.6
k_{Au} (s^{-1}) μmol^{-1}	0.104 ± 0.013	0.067 ± 0.011
SSA (m^2 L^{-1})	0.97[b]	0.64
k_1 (s^{-1} L m^{-2})	0.0053 ± 0.0007	0.0051 ± 0.0009

Table 3.2: Summary of nanoparticle size, specific surface area (SSA), and rate constants.[a]Weighted mean diameter calculated using 1.9 nm stabilized and 7.0 nm isolated Au NPs; weighted amounts taken from wt.% quantified using SEM-EDS.[b]SSA calculated using 6.17 nm weighted mean diameter of Au NPs. Calculations provided in Appendix B.

When the rate constant is considered, the silica-Au NPs are much more catalytically active compared to the control Au NPs, showing higher efficiency of the Au atoms in the sample. However, when the SSA of the samples is normalized, the rate constant of the silica-Au NP sample is not significantly different than the control Au NPs. This reflects the inert chemical behavior of the silica support material, which is not expected to enhance the catalytic activity of the silica-Au NPs.[143,144]

3.4 Reaction Timelines

To explain the formation of two populations of silica-Au NPs in fs-RLAL, we consider the timescales of chemical reactions in the initially generated plasma and material ejection from the Si wafer occurring in our experiments. Due to the extremely short duration of the femtosecond laser pulse as compared to the nanosecond pulses typically used in RLAL, both plasma reactions and material ejection can occur on significantly faster timescales than the $\sim\mu$s timescales of cavitation bubble formation and collapse. Here, we will focus on how these early reactions taking place on timescales of tens of femtoseconds through nanoseconds can form two types of silica-Au NPs.

We first consider reactions in the initially formed plasma at the water-Si interface. The laser intensity used in our experiments exceeds the optical breakdown (OB) threshold of 10^{13} W cm^{-2} for 800 nm, 30 fs pulses in water,[90] and the fluence is sufficient to produce an electron-hole pair density at the Si surface exceeding the critical threshold of 10^{22} cm^{-3} for ablation.[76,145] The electrons generated in the OB plasma (Eqs. 1.1, 1.2, 1.3) and ejected from the Si surface can induce Au^{3+} reduction (Eq. 3.1). The timescales for both electron formation processes are on the order of a few tens of femtoseconds,[76,77,145,146] and the resulting electrons become hydrated (Eq. 1.2) on a timescale of several hundred femtoseconds.[94,95]

Because hydrated electrons react with $[AuCl_4]^-$ with a diffusion-controlled rate constant of 6.1×10^{10} M^{-1} s^{-1} [147] and have a lifetime in pure water of hundreds of ns [148], $[AuCl_4]^-$ reduction in solution can begin within hundreds of femtoseconds of the laser pulse and occur during the next several ns. As a result, a significant fraction of the available $[AuCl_4]^-$ near the laser focus may be consumed within 1 ns of the laser pulse. The OB plasma also contains OH radicals that lead to the formation of H_2O_2 (Eq. 1.5) on the timescale of ~10 ns–10 μs. [148] This peroxide formation induces autocatalytic surface growth of the gold clusters to larger nanoparticles (Eq. 3.2). [46,47,49] We propose that this plasma-mediated mechanism beginning within tens of femtoseconds following arrival of the laser pulse drives the formation of the larger isolated Au NPs in our experiments.

$$[AuCl_4]^- + 3\,e^-_{aq} \longrightarrow Au(0) + 4\,Cl^- \tag{3.1}$$

$$[AuCl_4]^- + \frac{3}{2}\,H_2O_2 + Au_m \longrightarrow Au_{m+1} + \frac{3}{2}\,O_2 + 3\,HCl + Cl^- \tag{3.2}$$

Second, we consider the dynamics of material ejection from the Si surface. After the removal of free electrons, a strong electrostatic field develops on the Si surface due to the charge separation, which ultimately pulls out silicon atoms and ions from the surface if the laser fluence is above the ablation threshold. [76,77,145] Our fluence of 0.88 J cm^{-2} exceeds the reported ablation threshold for Si in water with fs laser pulses (0.16 J cm^{-2} [75]) by a factor of 5.5. At fluences up to three times the ablation threshold, both experiments and molecular dynamics simulations report the beginning of material ejection on a timescale of tens or hundreds of ps after the laser pulse, depending on the target material and environmental conditions (Table 3.3). [76,139,141,146,149] While reported timescales for Si ejection are typically faster than 100 ps, [76,146,149] these studies were conducted in air or vacuum, without the confinement provided by the water environment. The slower timescales of 200–500 ps reported for Ag in water [139,141] likely provide a better estimate for the ejection of Si atoms into the surrounding water in our experiments. Subsequent ejection of larger molten droplets can then occur on timescales of several ns. [139] These Si species in the expanding low-density Si-water mixing region or injected into the colder water above will undergo rapid oxidation and cooling and can provide nucleation sites for nearby gold ions. We propose that the ejection of Si species on the sub-ns timescale leads to formation of the stabilized silica-Au NPs. The small size of the Au NPs stabilized by the silica matrix may result from either depleted $[AuCl_4]^-$

concentration due to the plasma reactions discussed above or silica species coalescing around the initially formed Au nuclei, halting further growth.

Materials	Pulse Duration (fs)	Environment	Timescale (ps) / Ref.
Si	130	air	20–100 [76]
Si	500	vacuum	24 [149]
Si	90	air	10–100 [146]
Ag	40	water	200 [141]
Ag	10^4	water	500 [139]

Table 3.3: Reported timescales for onset of material ablation with femtosecond pulses.

The proposed reactions and timescales in our experiments that lead to each population of silica-Au NPs are illustrated in Fig. 3.7. At early times during and immediately after the pulse, the plasma reactions begin. Free electrons generated in the plasma at the Si-water interface hydrate and react with the initially high concentration of $[AuCl_4]^-$, forming Au nuclei within hundreds of fs to a few ns. These can coalesce and react with the H_2O_2 generated beginning around 10 ns to predominantly form the larger isolated Au NPs. Meanwhile, surface reactions begin around 100 ps or later. The ejected Si atoms and liquid droplets oxidize and coalesce, at which point they can react with the remaining $[AuCl_4]^-$ and Au nuclei present. The expected low concentration of $[AuCl_4]^-$ near the Si-water interface at around 1 ns after the laser pulse could give rise to the predominant formation of ultrasmall Au NPs stabilized by the Si that is ejected. Alternatively, the encapsulation of the growing Au nanoclusters by the Si species could quench the growth. The presence of some large Au NPs that appear to be attached to the Si matrix (Fig. 3.1a) may be accounted for by Au NPs formed in the plasma reactions coming into contact with the Si species prior to their cooling. Finally, we note that the formation of cavitation bubbles beginning approximately 100 ns after the laser pulse [58] could contribute to the observed silica-Au NP morphologies, particularly for the stabilized Au NPs.

Both the isolated and embedded silica-Au NPs formed in our experiments have significantly different morphologies as compared to silica-Au NPs prepared from ns-RLAL, indicating that completely different reaction dynamics from those depicted in Fig. 3.7 occur when ns lasers are used. Saraeva *et al.* generated small 10 nm Au NP-decorated 1 μm silica particles from ns-RLAL of a silicon wafer immersed in a $[AuCl_4]^-$ solution.[150] They reported

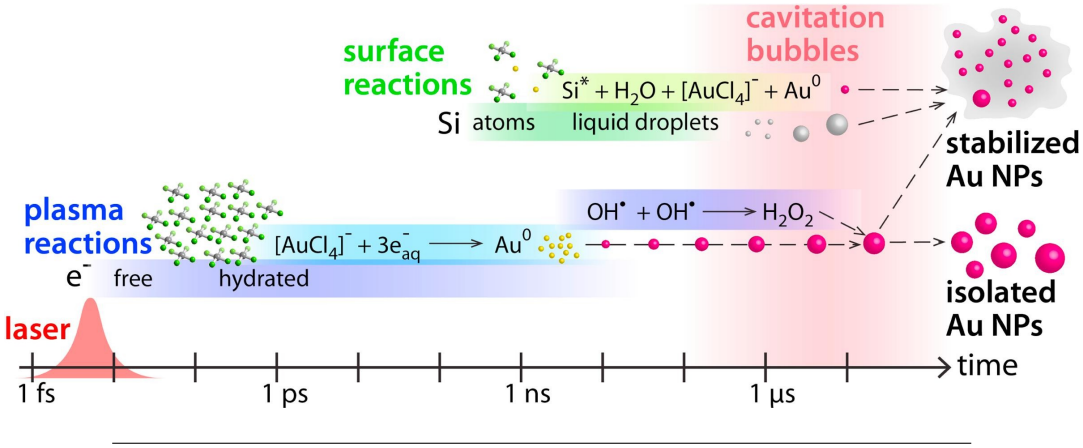

Figure 3.7: Proposed timescales of reactions in fs-RLAL.

that no Au NPs formed in the absence of the Si wafer, indicating that $[AuCl_4]^-$ reduction occurred primarily through reaction with ablated Si species through processes such as galvanic replacement.[150] In contrast, the formation of Au NPs from plasma reactions in water alone indicates that $[AuCl_4]^-$ reduction in fs-RLAL can occur without any Si species interactions, as we propose in Fig. 3.7. Liu *et al.* employed a double beam ns-RLAL approach using a 355 nm, 2 ns pulse for ablation and a 532 nm, 10 ns pulse to irradiate the ablation plasma, resulting in large silica particles (200–500 nm) possessing wrinkled surfaces, silica particles with veins of gold throughout, and silica-core/Au-shell particles.[140] They reported that irradiation of the plasma region at a wavelength resonant with the Au SPR frequency facilitated the reduction of $[AuCl_4]^-$ to form Au NPs that encapsulate the ejected Si species.[140] The simultaneous material ejection and metal salt reduction timescales over hundreds of ns in the latter experiments are distinct from the likely separate timescales of metal salt reduction and material ejection that can occur in fs-RLAL. Further investigation of the different nanoparticle formation mechanisms in ns- and fs-RLAL is needed to fully understand the origin of the distinct particle morphologies produced.

3.5 Conclusions

This work introduced a fs-RLAL approach as a facile route to silica-Au NPs with significantly smaller Au NP sizes than accessible in previously reported ns-RLAL studies. The silica-Au NPs were found to be active towards catalytic reduction of PNP by $NaBH_4$, with similar surface area normalized activity when compared to the control Au NPs synthesized in the absence of Si. Characterization of the products revealed two populations of Au NPs-

(i) larger, predominantly isolated Au NPs (7.0±2.0 nm), and (ii) small Au NPs (1.9±0.7 nm) stabilized by an amorphous silica matrix, along with previously unreported silica species deconvoluted in the Si2p XPS spectra. Considering the timescales of reactions in a fs-laser optical breakdown plasma and material ejection from ablation, we proposed formation mechanisms for the two observed populations of silica-Au NPs. Unlike in ns-RLAL, we expect that photochemical reduction of metal ions can occur before material ejection in fs-RLAL, potentially enabling unprecedented control over accessible particle morphologies due to the separation of the reduction and ablation steps. Further elucidation of the distinct chemical reactions and timescales occurring in ns- and fs-RLAL is needed to advance the rational design and synthesis of catalytically active nanostructures using this readily generalizable approach.

Chapter 4

Silica-Copper Nanostructures

4.1 Background and Motivation

Copper nanoparticles (Cu NPs) are valued for their low cost, high conductivity, and thermal stability, making them a popular alternative to rare earth metals for biological sensing and imaging,[151] antimicrobial applications,[152] inkjet-printable electronics,[143] and catalysis.[18] In particular, the ability of copper to access many oxidation states makes supported Cu NPs active catalysts towards reactions such as electrochemical reduction,[28] thermochemical hydrogenation,[153] and photochemical reduction of CO_2,[154] photocatalytic degradation of organic dyes,[155] and other organic transformations.[27,156,157]

While Cu NPs possess high catalytic activity and high temperature stability, a major bottleneck to using copper-based nanomaterials for catalysis is the propensity for small Cu NPs to agglomerate, and for Cu surfaces to oxidize. Support materials such as graphene, oxides, polymers, and metal-organic frameworks (MOFs) are added to prevent agglomeration and surface oxidation, while preserving the high catalytic activity of Cu NPs.[18,26,158] In particular, silica has been used as a support material for various metal NPs due to the silanol surface groups that enhance binding with metal NPs.[18,29] The majority of synthesis approaches to fabricating copper-silica nanostructures involve wet chemical methods such as incipient wetness impregnation, deposition-precipitation, strong electrostatic adsorption, and ammonia evaporation.[18,26–30] In these methods, the silica is either prepared by the Stöber method or purchased commercial amorphous/fumed silica, and the copper is added in the form of a salt complex. Copper-silica bonding is achieved by heating up the slurry or solution, followed by calcining the finished product. A drawback of many of these methods is that uneven distribution of the copper complex throughout the silica often results in poorly dispersed Cu NPs

with large size distributions and low copper loading. In this chapter, the synthesis of silica-Cu nanostructures are prepared using the fs-RLAL technique (details in Section 2. Different morphology silica-Cu nanoparticles were formed when the fs-RLAL synthesis was carried out in different pH precursors, and the results are discussed below.

4.2 pH-Dependent Morphology of Cu-Silica Nanostructures

The three Cu-silica (sample names provided in Table 2.1) products are visualized in the TEM images displayed in Fig. 4.1a-c with detailed insets, and additional TEM images are reported in Appendix C. While all three products contain large spherical particles around ∼70−100 nm in diameter, these particles are most abundant in the Cu-silica-3.0 sample, and rarely seen in the Cu-silica-10.4 sample. Many of the spherical particles in the Cu-silica-3.0 and Cu-silica-5.4 samples are smooth throughout the entire particle, while some have a darker core and lighter shell, indicative of a Cu-core and silica-shell structure (insets in Fig. 4.1a and b). The Cu-silica-3.0 sample had very few core-shell particles. Size distribution analysis was possible on only 43 particles, and histograms of the core and outer diameter are displayed in Appendix C. The Cu-silica-5.4 had substantially more core-shell particles than the Cu-silica-3.0 sample, with size distribution analysis displayed in Figure 4.1d. The inner core had a mean diameter of 22.4±14.4 nm with sizes ranging from 2−63 nm, and the outer shell mean was 32.1±14.8 nm with sizes ranging 12−84 nm in diameter. Figure 4.1d displays histograms fit to Log-normal distributions of the inner and outer diameters of the Cu-silica-5.4 sample. The Cu-silica-10.4 sample exhibits completely different morphology from the samples produced at lower pH (Fig. 4.1c). This product predominantly contains small, 1.52±0.75 nm Cu NPs dispersed throughout a matrix made up of long nano-needles and amorphous structures, along with a few large spherical particles decorated with small Cu NPs (inset). A histogram of the Cu NPs is displayed in Fig. 4.1e fit to a Gaussian distribution.

HRTEM images of the Cu-silica-5.4 and Cu-silica-10.4 products are displayed in Fig. 4.2a and c with SAED patterns (Fig. 4.2b and d). HRTEM analysis was not performed on the Cu-silica-3.0 sample due to the low number of core-shell particles. The inset in the Cu-silica-10.4 HRTEM image shows a small crystalline nanoparticle with lattice spacings measuring 2.13 Å corresponding to the (200) plane of Cu_2O.[159] The bottom inset of Fig. 4.2a shows the amorphous structure of the silica. The SAED pattern in Fig. 4.2b has two faint diffraction

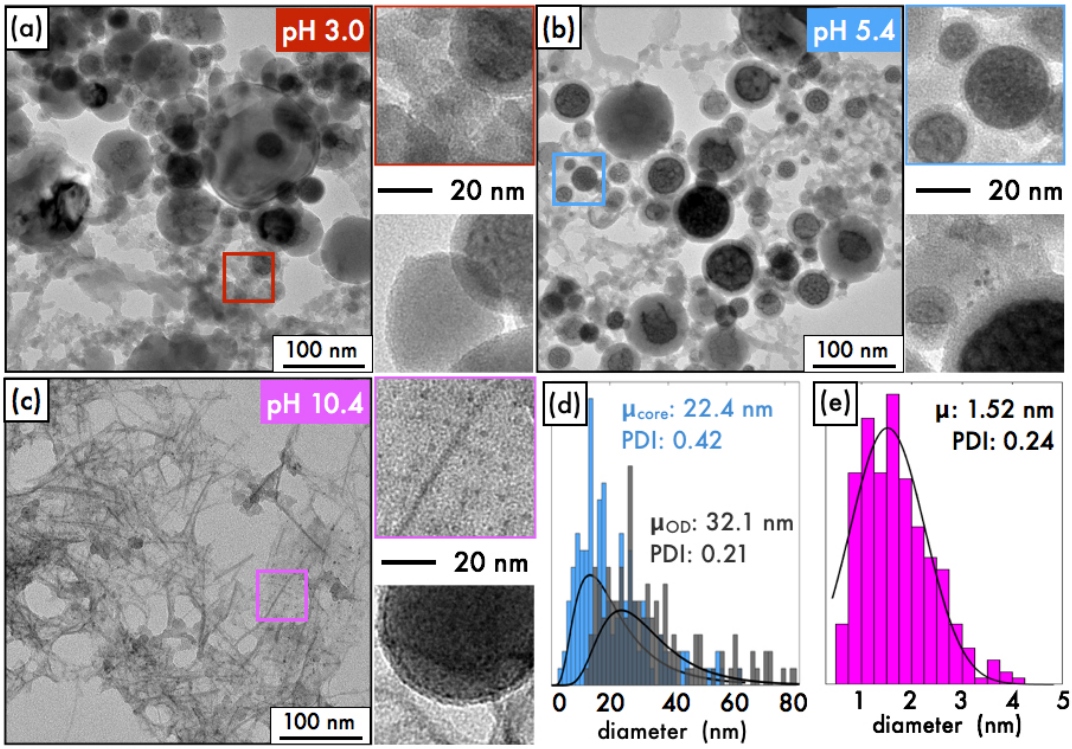

Figure 4.1: TEM images of Cu-silica samples at pH 3.0 (a), pH 5.4 (b), and pH 10.4 with histograms of Cu-silica-5.4 (e) and Cu-silica-10.4 (e).

rings measuring 2.41 Å and 2.04 Å corresponding to the (111) plane of Cu_2O and the (111) plane of fcc-Cu.[160] The Cu-silica-5.4 sample in Fig. 4.2c had some small crystalline nanoparticles with lattice spacings measuring 2.07 Å, corresponding to the (111) plane of fcc-Cu. It was difficult to confirm that the core of the core-shell particles was crystalline copper due to the thick amorphous layer over top of it (bottom inset in Fig. 4.2c). The SAED pattern of the Cu-silica-5.4 sample in Fig. 4.2d shows three faint rings with diameters 3.11 Å, 2.01 Å, and 1.14 Å, corresponding to the (111) plane of fcc-Si, the (111) and (311) planes of fcc-Cu.[159] Our results are consistent with the Cu crystalline phases generated by laser ablation of copper, in which the major phases of copper generated included Cu_2O and fcc-Cu.[161–163]

SEM-EDX analysis was performed on the three Cu-silica samples, with a representative EDX spectrum of the Cu-silica-10.4 sample displayed in Fig. 4.3. The peaks located at 0.53 keV, 0.95 keV, and 1.74 keV correspond to the O Kα, Cu Lα, and Si Kα lines. The inset graph shows the wt.% Cu, Si, and O quantified in the samples, and Table 4.1 displays the numerical values of wt.% Cu, Si, and O from EDX, XPS, and ICP-OES analysis. The Cu-silica-10.4 sample contains the highest amount of Cu, about ten to twenty times the amount

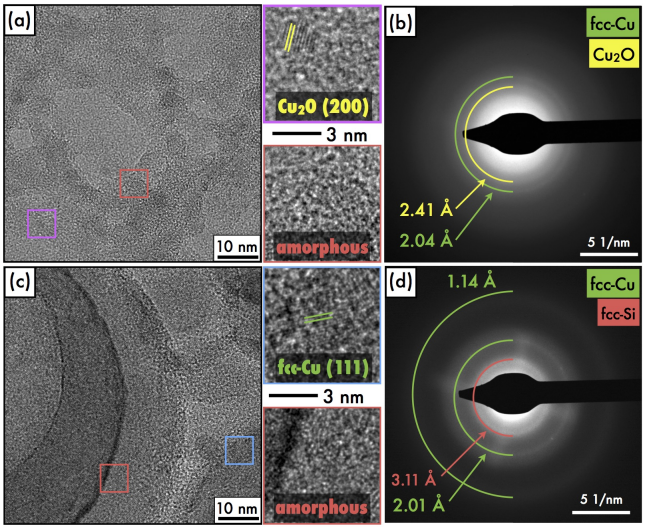

Figure 4.2: HRTEM images of Cu-silica-10.4 (a) and Cu-silica-5.4 (c) with SAED patterns (b) and (d), respectively.

as the Cu-silica-5.4 and Cu-silica-3.0 samples. The significantly higher Cu loading in the Cu-silica-10.4 sample is corroborated by the ICP-OES and XPS results, also displayed in Table 4.1. XPS data was converted from atomic %, with calculations provided in Table C1 in Appendix C. XPS analysis shows significant surface oxidation of the three samples, which is compensated for by the decrease in Cu content in the Cu-silica-10.4 sample, and decrease in Si content in the other two samples. The copper content did not decrease between EDX and XPS analysis for the Cu-silica-5.4 sample, suggesting that the copper present within the top 10 nm of this sample is protected from surface oxidation.

	ICP-OES[a]	SEM-EDX[a]			XPS[bc]		
Sample	Cu	Cu	Si	O	Cu	Si	O
Cu-silica-3.0	1.4±0.4	4.3±0.9	67.5±1.5	28.1±0.7	0.3±0.3	40.1±0.1	59.6±31
Cu-silica-5.4	1.5±0.1	2.6±0.4	86.5±2.1	11.0±1.7	2.6±2.0	45.9±0.9	51.5±6.8
Cu-silica-10.4	31.5±0.4	36.5±2.1	37.3±4.6	26.2±2.6	19.2±6.1	22.6±2.7	58.1±5.5

Table 4.1: weight % Cu from ICP-OES, weight % Cu, Si, and O from SEM-EDX, and XPS analysis. [a]analysis representative of entire sample material. [b]analysis representative of top 10 nm surface layer. [c]Values converted from atomic %, which is provided in Table C1 in Appendix C.

4.3 Cu-silica Nanostructure Composition

High resolution Cu2$p_{3/2}$ and Si2p atomic orbital XP spectra are displayed in Fig. 4.4a and b with the Cu-silica-10.4 spectra on the bottom panels and the Cu-silica-5.4 and -3.0 samples

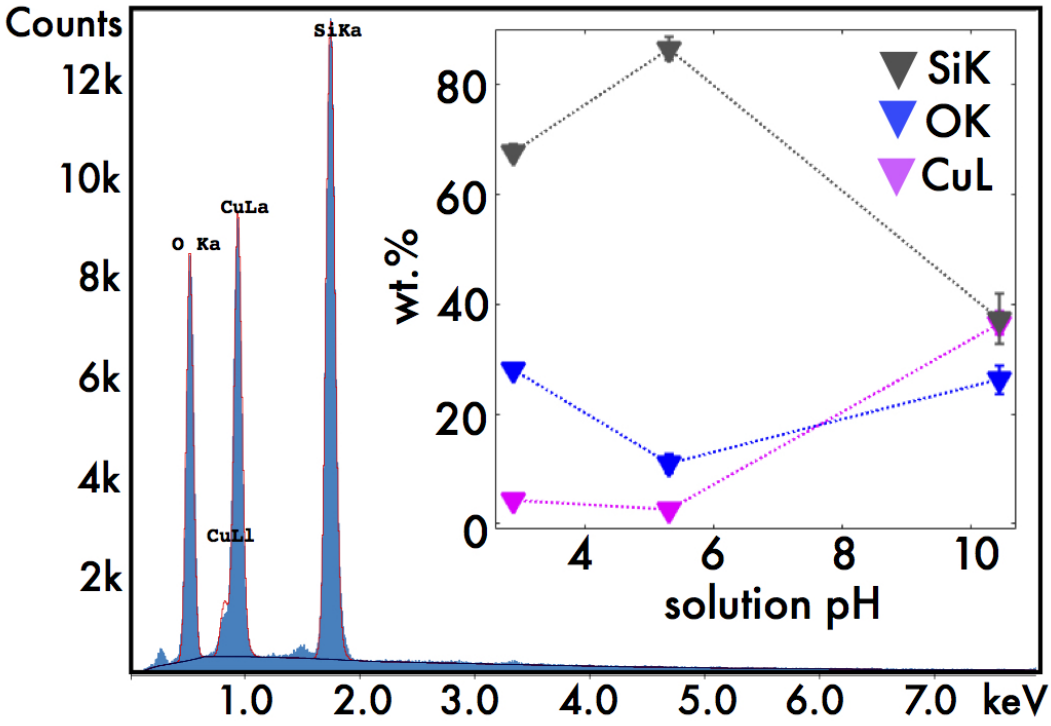

Figure 4.3: SEM-EDX spectrum of representative Cu-silica-10.4 sample with inset of wt.% of SiK, OK, and CuL for different pH solutions.

on the top panels (a Si2p spectrum of silica generated from ablating a silicon wafer in water is displayed in Appendix C). No Cu was detected in the $Cu2p_{3/2}$ spectrum for the Cu-silica-3.0 sample. In the $Cu2p_{3/2}$ spectra, a peak at 932.7 eV (purple) was fit in both samples, which corresponds to either Cu^0 (932.6 eV) or Cu^+ as in Cu_2O (932.2 eV).[129,136,164–166] The second peak near 934 eV in the Cu-silica-5.4 sample (blue) corresponds to Cu^{2+} and matches that of a CuO species.[160,167,168] In the Cu-silica-10.4 sample, this feature it is shifted to 935.3 eV (black), corresponding to Cu^{2+} interacting with silica.[27,160] In particular, this feature matches the binding energy of copper phyllosilicate ($Cu_2Si_2O_5(OH)_2$, Cu-PS) near 935–936 eV.[27,168,169] The peaks around 942–945 eV correspond to shake up satellite features from the 2p→3d transition from the $3d^9$ ground state electron configuration of Cu^{2+}.[164,165,170] This feature is strongly present in the Cu-silica-10.4 sample, and only weakly visible in the Cu-silica-5.4 sample due to its Cu low loading.

The Si2p atomic orbitals in Fig. 4.4b have several silicon species, with a large peak centered around 103 eV corresponding to oxidized silica, and a small peak near 99 eV (green) corresponding to Si^0.[171,172] Within the large oxidized silicon peak around 103 eV, two species

are fit for all three samples- the peak at 103.5 eV (gray) corresponds to Si^{4+} of Si—O—Si tetrahedrally coordinated silicon in amorphous silica,[172–174] and the feature at 102.2 eV (dark blue) corresponds to Si^{3+} in the form of Si_2O_3.[173,174] A third species was fit in the Cu-silica-10.4 sample at 100.7 eV (dark green), close to the 101 eV binding energy of Si^{+}.[173–175] Such down-shifting of the Si binding energy has been attributed to interaction of silica with Cu atoms.[156,176] The up-shifted Cu^{2+} peak and the down-shifted Si^{2+} peak suggest an interaction where Cu is slightly positive and the Si is slightly negative.

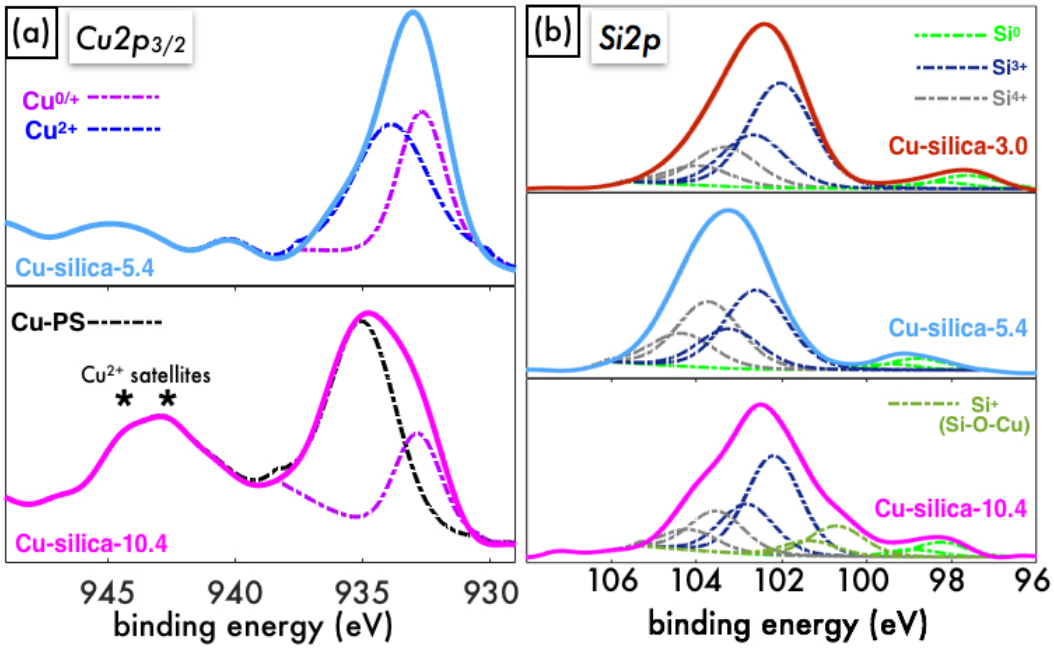

Figure 4.4: High resolution XP spectra of $Cu2p_{3/2}$ (a) and Si2p (b) atomic orbitals. Cu-silica samples generated under same experimental conditions, with different pH solutions.

Figure 4.5 displays the FTIR spectra of the three samples along with a control silica-10.4 sample, generated by ablating a silicon wafer immersed in water adjusted to pH 10.4 with KOH. The peaks at 800 and 1090 cm^{-1} in the control sample (gray) correspond to the symmetric and asymmetric stretching of amorphous silica. These two bands are prominent in the Cu-silica-3.0 and -5.4 samples (red and blue), but the 800 cm^{-1} band is nearly absent in the Cu-silica-10.4 spectrum (magenta). Moreover, the 1090 cm^{-1} band is significantly down-shifted to 968 cm^{-1}. This corresponds to a shift in bonding environment from Si—O—Si to Si—O—Cu, due to the longer Cu-O bond length than Si-O.[176] This band is also close to the 1024 cm^{-1} feature in Cu-PS.[9,153,177,178] The Cu-silica-10.4 sample also has a weak feature that could be attributed to $Cu(OH)_2$ at 690 cm^{-1}, Cu-PS at 670 cm^{-1}, or both.[9,153,177–179] The

broadness of this band and the weak intensity make it difficult to distinguish between these copper structures. The peak around 1400 cm^{-1} that is present in the Cu-silica-3.0 sample likely arises from the symmetric stretching vibration of nitrate groups in $Cu_2NO_3(OH)$.[180] All samples have peaks around 1652 cm^{-1}, which corresponds to the O—H bending mode of adsorbed water.[27,180]

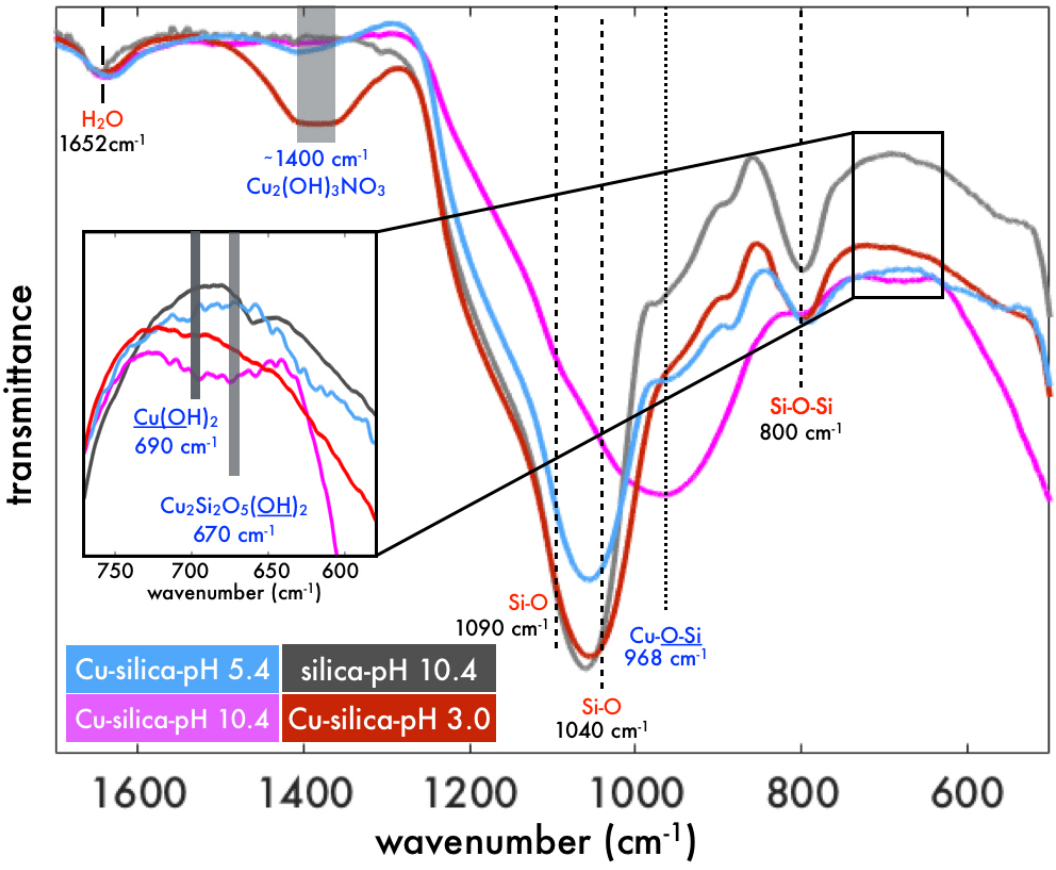

Figure 4.5: FTIR spectra of silica-pH 10.4 (generated from ablating Si wafer in water at pH 10.4), the Cu-silica-3.0, Cu-silica-5.4, and Cu-silica-10.4 samples.

XRD patterns of the Cu-silica-10.4 (magenta) and Cu-silica-5.4 (blue) samples are displayed in Fig. 4.6 and compared to a control sample in which a silicon wafer was ablated in water (black). All samples contain sharp, intense peaks located at 2θ = 28.4°, 47.3°, 56.1°, 69.2°, 76.4°, and 88.1° corresponding to the (111), (222), (331), (440), (533), and (640) planes of cubic silicon (ICDD: 04-012-7888). There is a small, broad peak around 36° present only in the Cu-silica-10.4 sample that corresponds to either the (111) CuO plane (35.6°), the (111) plane of Cu_2O (36.5°), or a Cu-PS structure.[9,153,177,178] The inset shows the Gaussian peak fit yielding a FWHM of 4.90° corresponding to a 1.78 nm diameter of

the crystalline nanoparticle, according to the Scherrer equation.[181] The FWHM of the fcc-Si (111) peak at 28.4° was determined to be 0.25°, yielding a silicon crystalline diameter of 33.6 nm. The XRD pattern shows that there are crystalline silicon particles present in these samples, consistent with the large spherical particles visible in the TEM images in Fig. 4.1a. The absence of silica in the XRD patterns supports the amorphous nature of the silica as evident in the HRTEM images, Si2p XPS spectra, and FTIR spectra.

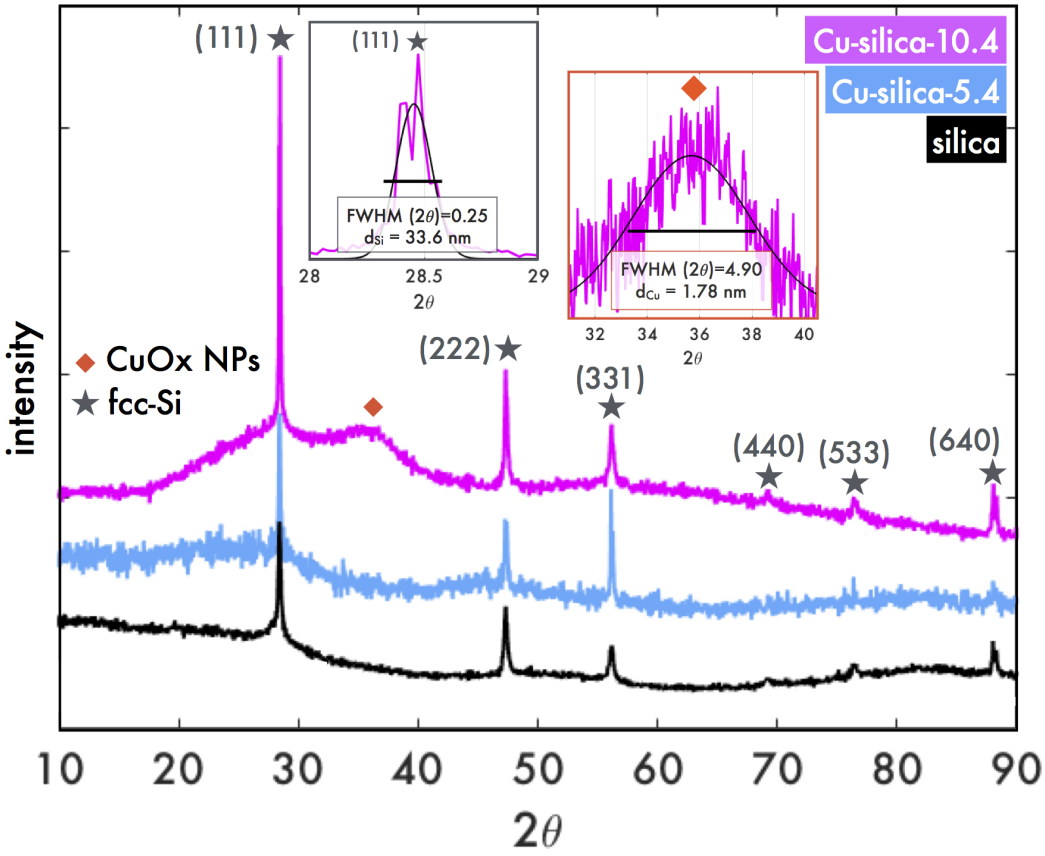

Figure 4.6: XRD patterns of Cu-silica-10.4, Cu-silica-5.4, and silica generated from laser ablation of silicon wafer in water.

4.3.1 Catalytic Activity Toward Para-Nitrophenol Reduction

The catalytic reduction of para-nitrophenol (PNP) by sodium borohydride was employed as a model reaction to compare the catalytic activity of the silica-Cu samples. Because all samples were irradiated under the same laser conditions and underwent the same post-synthesis processing procedure, we assume the amount of silica present in all samples is equivalent, and the rate constants reported reflect the catalytically active copper particles in the samples.

Therefore, the same volume of re-dispersed pellet was added to all PNP reactions. Experimental details and calculations for determining the catalytic rate constants are provided in Appendix A.

Briefly, the catalytic reduction of PNP to para-aminophenol (PAP) by sodium borohydride follows pseudo-first order reaction kinetics due to the excess of $NaBH_4$ added to the reaction

$$\mathrm{PNP} + \mathrm{NaBH}_{4(xs)} \xrightarrow{Cu-silica} \mathrm{PAP}. \tag{4.1}$$

The para-phenolate ion absorbs strongly at 400 nm, allowing for the reaction rate to be determined by monitoring its absorbance upon the addition of the catalyst. The apparent rate constants, k_{app} (s^{-1}) versus wt.% Cu from XPS analysis are displayed in Fig. 4.7, with the different pH conditions labeled. There is a linear relationship between the rate constant and the surface Cu content, reflecting the high catalytic activity of the Cu-silica-10.4 sample which contains the highest amount of surface Cu. While nearly no Cu was detected in the Cu-silica-3.0 sample, it still possess catalytic activity, suggesting that the there was Cu present in the sample, but in very small quantities.

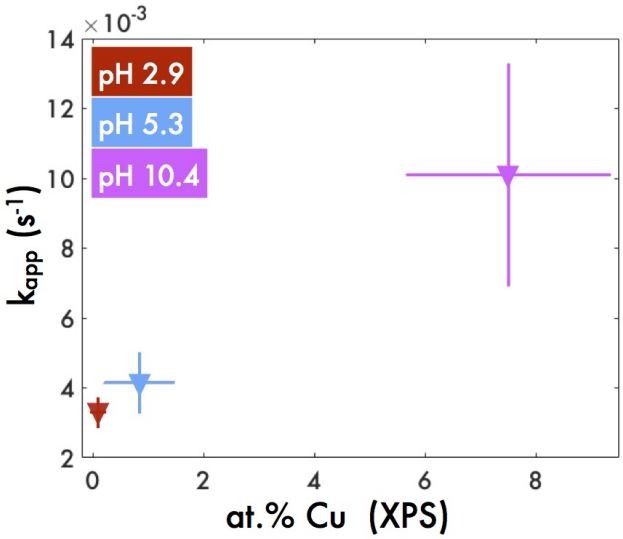

Figure 4.7: Apparent rate constant (k_{app}) versus at.% Cu from XPS analysis.

4.4 Influence of Solution pH on Nanostructure Morphology

Wet chemical approaches to fabricating oxide supported metal nanoparticles emphasize the importance of choosing the support, metal precursor, and solution pH for maximizing the metal loading.[182] Determining the point of zero charge (PZC) of the support material aids in identifying the pH conditions for optimal interaction between the metal complex and the oxide support.[35,182] The PZC of a material is the pH at which the hydroxyl groups that populate the surface of an oxide have a neutral charge. When the pH is below the PZC of the support, the hydroxyl groups are protonated, and when the pH is above the PZC, the hydroxyl groups are deprotonated.[26,30,182] Silica has a PZC of pH 4, so when the solution pH is above this value, cationic metal complexes in solution can adsorb onto the negatively charged surface of the silica.[30]

The copper loadings reported in Table 4.1 demonstrate the need for basic pH to achieve high copper loading under our synthesis conditions; even in the weakly acidic solution at pH 5.4, little copper was found in the product. In contrast, the Cu-silica-10.4 sample had a high copper loading of 31.5 wt%; much higher than many previous reports using wet chemical techniques that typically achieve around 10 wt.%.[30,35,183–186] Previous investigations of pH-dependent metal loading on silica that achieved copper loadings above 30 wt.% have formed Cu-PS structures,[157,177,187,188] consistent with our results. However, the wet-chemical synthesis methods used are considerably more time- and material-consuming than our RLAL method. For instance, the method of Toupance *et al.*, in which a copper nitrate solution adjusted to pH 9 using ammonia mixed with nonporous silica was stirred at room temperature for one week, required 100 times the amount of copper relative to our conditions to yield 36.6 wt.% Cu with 4.5 nm Cu NPs.[177]

In contrast to pre-synthesized fumed silica or nonporous silica spheres used in wet chemical methods, our silica is produced *in situ* from laser ablation. As the silicon atoms and clusters are ejected into solution, they may interact with other nearby species including hydrated electrons and hydroxyl radicals, resulting in oxidation to silica. Under basic conditions, nearby OH^- ions may interact with the oxidized silica clusters, deprotonating their surfaces.[189] The negatively charged silica clusters attract nearby copper in the form of the bridged copper hydroxide dimer, $[Cu_2(OH)_2]^{2+}$, which is formed in the pH range 6.5−10.5.[30,190]

The abundance of deprotonated silica clusters generated from laser ablation provide numerous sites for these copper complexes to interact with, driving the high copper loading under basic conditions.

Figure 4.8 displays a graphical representation of the formation mechanisms of the copper-silica materials under the different pH conditions. We note that the solution pH decreased from 10.4 to 8.5 and 5.4 to 4.2 during synthesis of the Cu-silica-10.4 and -5.4 samples, respectively. The two samples generated at final solution pH less than pH 4 are shown above the 'silica PZC 4.0' line[26,30] in Fig. 4.8. Under these conditions, silica clusters ablated off of the Si wafer into solution become protonated and repel the surrounding Cu^{2+} ions, leading to low amounts of Cu incorporated into the product. While it is possible that a small amount of Cu in the product dissolves in the acidic solution following laser synthesis (see details in Appendix C), this process is unlikely to be the primary cause of low Cu incorporation because little Cu is incorporated even at an initial pH of 5.4. For the Cu-silica-5.4 sample in which Cu is incorporated into the particles, segregation of the Cu-silica phases result in large Cu-core/silica-shell particles with varying sizes and shell thicknesses. The formation of the silica shell rather than silica core may be due to the higher surface energy of silicon than copper in the liquid form. Synthesis of Cu-core/silica-shell particles by evaporating elemental Cu and Si using a high powered electron beam resulted in phase segregation with the silicon shell forming around liquid Cu, due to the higher surface energy of liquid silicon relative to liquid Cu.[191,192] In contrast, the proposed formation mechanism of the Cu-silica-10.4 sample is displayed below the line labeled 'silica PZC 4.0', where Cu-O-Si bonds form due to the strong interaction between the deprotonated silica clusters and the cationic copper hydroxide dimers. The morphology contains sheet- and needle-like structures comprised of amorphous silica, copper phyllosilicate, or both, decorated with sub-2 nm Cu clusters. The small size of the Cu particles likely results from the strong interaction between the Cu nuclei and the silica clusters, halting further Cu NP growth. The presence of sub-2 nm clusters dispersed throughout the silica is similar to our recent report of fs-RLAL synthesis of sub-3 nm Au NPs dispersed throughout a silica matrix under basic conditions[110] Our observation of distinct copper-silica material structures using fs-RLAL at different solution pH is consistent with previous RLAL studies showing a dependence of Pt-Co NP properties on solution pH[22,105] and suggests that solution pH provides a generally applicable method to control nanomaterial properties with RLAL.

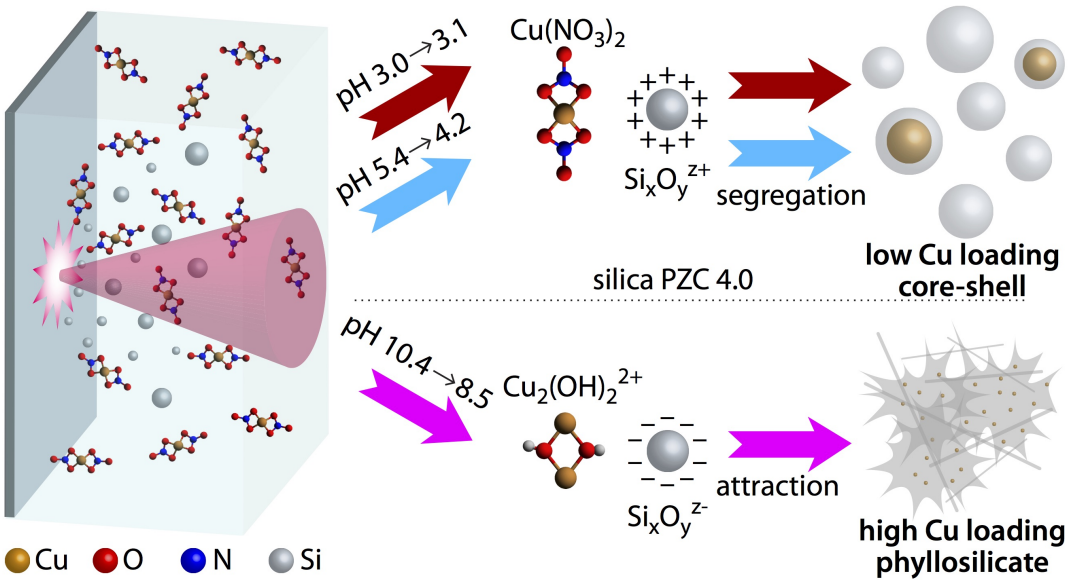

Figure 4.8: Graphical representation of the pH dependent formation of Cu-silica samples

4.5 Conclusions

Copper-silica nanocomposites were synthesized using a fs-RLAL approach, with distinct copper-silica morphologies forming from different precursor solution pH conditions. The highest copper loading on silica of 31.5 wt.% achieved with a precursor solution pH of 10.4 generated 1.52±0.75 nm Cu NPs well dispersed throughout a silica matrix. TEM, XPS, XRD, and FTIR analysis are consistent with the coexistence of copper phyllosilicate and amorphous silica in the matrix. Lower solution pH of 5.4 and 3.0 resulted in Cu-core/silica-shell morphologies with Cu NP sizes ranging from 30–80 nm in diameter, and only 1.4–1.5 wt.% loading of Cu. The catalytic activity of the synthesized materials was proportional to the copper loading, with very low catalytic activity toward the reduction of para-nitrophenol from the samples synthesized at pH 3.0 and 5.4, and much higher catalytic activity from the sample synthesized at pH 10.4. The pH dependent compositions and morphologies of our copper-silica nanocomposites are attributed to the interaction of positively charged Cu precursor species and ablated silica species. At low pH, protonation of silica clusters results in copper and silica phase segregation, forming core-shell structures. At high pH, the copper hydroxide dimer ion strongly interacts with deprotonated silica clusters, resulting in sub-2 nm Cu clusters supported on a copper phyllosilicate/amorphous silica matrix. The results in this study demonstrate the importance of understanding the effect of solution pH on the electronic

charge of ablated target material to allow for better control over the product morphology. This approach to synthesizing Cu-silica composite nanomaterials provides valuable insight into designing RLAL reaction conditions for synthesizing additional metal-oxide nanocomposites with high metal loadings that may be used for catalytic applications.

Chapter 5

Nickel-Phyllosilicate Formation from Reactive Laser Ablation in Liquid

5.1 Background and Motivation

Metal phyllosilicates are a class of minerals comprised of layered silicate species in octahedral and tetrahedral coordinations, with metal cations stabilized throughout the silicate layers. Figure 5.1 displays the 2:1 and 1:1 Ni-phyllosilicate (Ni-PS) phases.[24,193–195] The type of metal cations commonly found in the phyllosilicates are first-row transition metals including Ni, Cu and Co. These metal-PSs range from plate-like structures to nano-scrolls, and are affected by the local bonding environment between the silicates and metal cations, dictated by the atomic radius of the metal cations relative to the silicates.

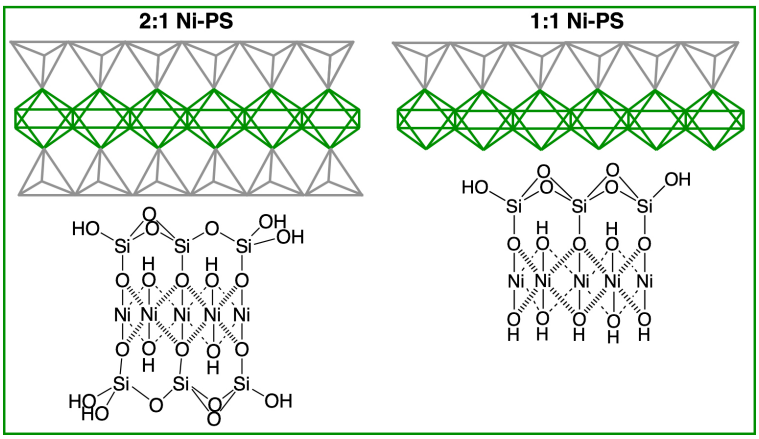

Figure 5.1: Nickel-phyllosilicate (Ni-PS) as 2:1 and 1:1 phases.

This class of materials has recently gained attention due to the ability to induce reduction of the well-dispersed metal cations to form ultrasmall metal NPs or nanoclusters that are

highly stabilized by the silicate structure due to the silicate-O-metal bonding environment.[24] Thus, these silicate-stabilized metal nanoparticles have promising properties for catalytic applications that require high degrees of thermal stability, such as CO_2 hydrogenation. Additionally, the different metal cations are known to have high catalytic activity toward different reactions including Fischer-Tropsh (Co-PS),[31] methane (Ni-PS) and methanol (Cu-PS) formation from CO_2 hydrogenation.[24,31,114]

While significant research has expanded the understanding of the structures and properties of metal-PS, the synthesis approaches typically revolve around a two-step method of preparing the metal-PS followed by an annealing step to reduce the metal cations to metal clusters, and only recently was the synthesis of Cu-PS from the RLAL approach reported.[24,195–197] The field of laser-assisted synthesis of nanostructured materials has grown significantly in the past decade, leading to the development of highly functionalized nanomaterials including Ni-Fe layered double hydroxides[15], PtCo/CoOx nanoalloys[104], and structurally disordered $CoFe_2O_4$/CoO materials[198], with promising properties for catalytic applications. However, as identified in the previous chapter, the solution conditions, especially pH, can strongly affect the powdered product composition. There is less literature focusing on the dissolved solution-based species that drive the pH-dependent product composition. In this chapter, the pH-dependent silicate species formed upon fs-laser ablation of a silicon wafer immersed in water and $Ni(NO_3)_2$ solutions over a range of pH conditions will be explored. The aim of this chapter is to better understand the solution-based species that affect the product composition and morphology of Ni-based structures under different pH conditions.

5.2 Results and Discussion

5.2.1 Characterization of Dissolved Species in Solution

The prepared samples from Table 2.2 were centrifuged for 90 min at 13,000 rpm to ensure that all clusters and nanoparticles were separated out into the pellet, and the species present in the supernatant were only the dissolved species. ICP-OES and SEM-EDX were used to quantify the Ni content in the supernatant (as ppm) and the washed pellet (as wt.%), respectively, and the results are displayed in Figure 5.2, with numerical values provided in Table 5.1. The silica-Ni-pH 5.9 sample had the highest concentration of Ni in the supernatant at 117.5

ppm, and the concentration of Ni in the supernatant decreased as the precursor solution pH increased up to pH 10.6. Alternatively, the wt.% Ni quantified in the dried pellets shows an inverse relationship to the Ni content quantified in the supernatant. The lowest wt.% Ni of 0.47±0.08 was in the silica-Ni-pH 5.9 pellet, and increased with solution pH up to 29.3±3.6 wt.% in the silica-Ni-pH 11.8 sample.

Sample	Ni in Supernatant (ppm)[a]	Ni in pellet (wt.%)[b]	Initial pH	Final pH
silica-Ni-pH 5.9	117.5±3.8	0.47±0.08	5.94±0.01	5.63±0.5
silica-Ni-pH 8.3	87.4±2.6	6.5±1.8	8.33±0.06	7.05±0.28
silica-Ni-10.6	0.53±0.01	23.1±3.5	10.55±0.06	8.56±0.27
silica-Ni-11.8	0.33±0.01	29.3±3.6	11.79±NA	9.85±NA

Table 5.1: Nickel concentration (ppm) in supernatant. [a] Determined from ICP-OES. [b] Determined via SEM-EDX of dried pellet.

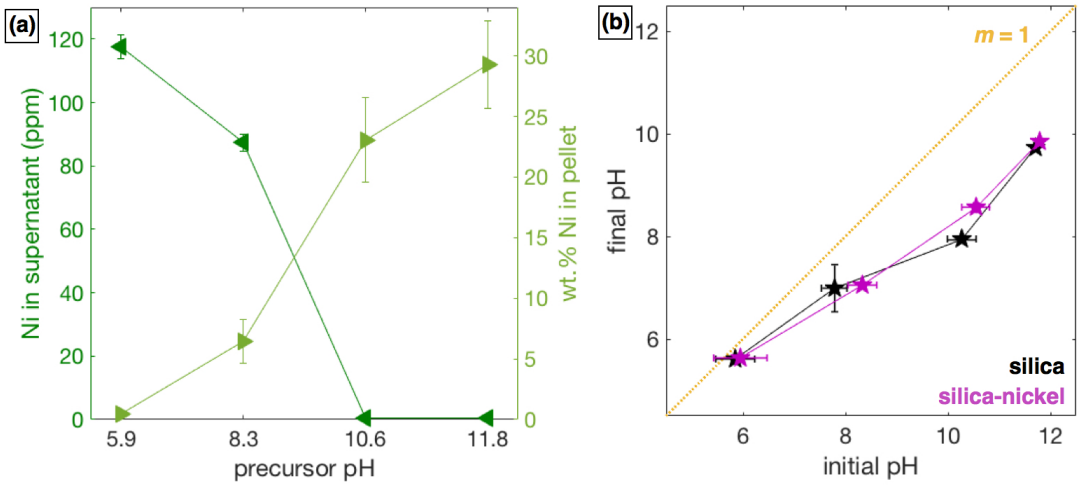

Figure 5.2: Nickel content in supernatant (left y-axis) and in dried pellet (right y-axis) (a); pH change of solutions before and after irradiation (b).

The precursor solution pH decreased after laser irradiation was complete, and the magnitude of this decrease was affected by the initial solution pH. Figure 5.2b displays the final solution pH versus initial solution pH for all silica and silica-nickel samples, with numerical values provided in Table 5.1. The pH change was dependent upon the initial solution pH, and not on the added $Ni(NO_3)_2$, as the data points of the silica and silica-Ni samples are nearly overlapping. For the solutions near an initial pH of 6, nearly no pH change was observed from laser irradiation, as the data points are near the plotted line with a slope of one. As the initial pH increased, the final pH decreased, with a maximum decrease of ∼2 pH units for the two highest pH samples pH 10.6 and 11.8.

Because the change in solution pH upon laser irradiation was dependent upon the initial solution pH, the solution-phase silicate species generated in the low- and high-pH samples were characterized. Figure 5.3a and b display ESI-mass spectra of the collected supernatants of four samples at the low and high pH conditions. In Figure 5.3a the mass spectra of the silica-pH 5.9 and silica-Ni-pH 5.9 are compared, with peaks labeled at 76 m/z and 244 m/z. The major peak at 76 m/z in the silica-pH 5.9 sample corresponds to deprotonated metasilicate, with the structure provided in Fig. 5.3. The metasilicate peak disappeared in the silica-Ni-pH 5.9, and a separate peak located at 244 m/z formed, corresponding to a $[(H_2O)_5NiOSi(H_2O)_2O]^-$ (Si-O-Ni) monomer species, with the structure provided in Fig. 5.3. The presence of metasilicate upon ablation in water, along with its disappearance and subsequent formation of the Si-O-Ni monomer species upon the addition of $Ni(NO_3)_2$, suggests that the metasilicate species plays a role in forming the Si-O-Ni monomer. Previous reports on the formation of Ni-PS have identified the formation of this Si-O-Ni monomer species as being the most favorable compound formed at lower pH ranges.[195,199] When the Si wafer was ablated in high pH solutions, the metasilicate peak is present in both solutions without (silica-pH 11.7) and with $Ni(NO_3)_2$ (silica-Ni-pH 10.6) (Figure 5.3b; spectra are normalized to the intensity of the metasilicate peak at 76 m/z). An additional peak is present at 95 m/z, which is assigned to deprotonated silicic acid. In the silica-Ni-pH 10.6 spectrum, a relative decrease in the 95 m/z species is observed upon addition of the $Ni(NO_3)_2$ to the precursor solution. Moreover, no peak at 244 m/z is present in the silica-Ni-pH 10.6 spectrum. Other peaks are assigned to a hydrated $Ni(OH)_2$ species (127 m/z) and a silicate-dimer (155 m/z). Since no major Ni-containing peaks were identified in this spectrum, it is likely that the majority of the nickel is found in the separated dried powder.

5.2.2 Characterization of Solid Products

XRD patterns of the obtained solid powders in Figure 5.4 contain a broad peak near 25°, corresponding to amorphous silica.[200] The weakly intense peaks located at 2θ = 28.5°, 47°, 56°, 69°, and 76° correspond to the (111), (220), (311), (400), and (331) planes of fcc-silicon, and the cell parameter was calculated to be a = 0.544±0.002 nm, in agreement with the value of fcc-silicon (JCPDS numbe 27-1402).[200] These peaks are present in both the silica- and silica-Ni samples, with more intense peaks present in the silica samples prepared below pH 11.7. The fcc-silicon peaks are weakly visible in all silica-Ni samples, and decrease in intensity in

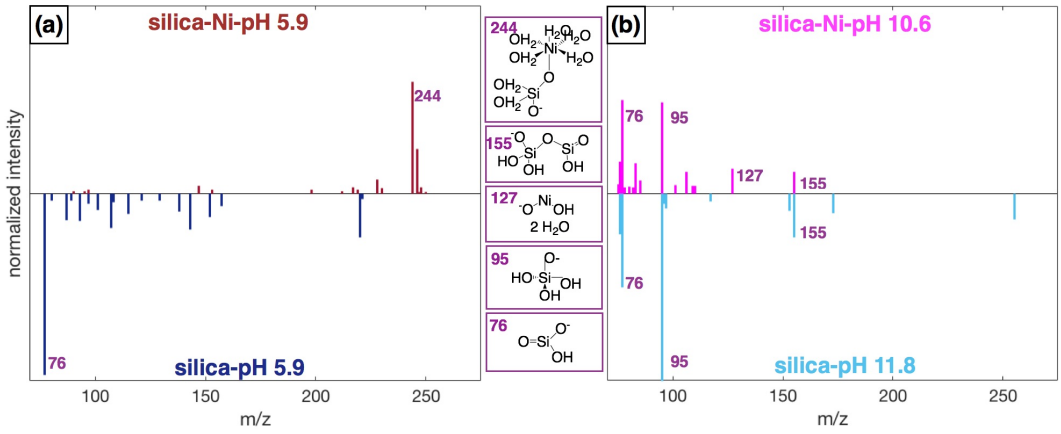

Figure 5.3: ESI-MS patterns for silica and silica nickel samples at different pHs.

the silica-Ni-10.6 and silica-Ni-11.8 samples. The silica-Ni-pH 8.3, pH 10.6, and pH 11.8 samples also have broad peaks located at 2θ = 34° and 61° that increase in intensity with increasing solution pH, with an additional peak near 73° in the silica-Ni-pH 11.8 sample. These peaks are consistent with reports of ill-crystallized nickel-phyllosilicate.[193,194,201–204] The silica-Ni-pH 5.9 pattern matches that of the XRD patterns of the nickel-free silica samples, and does not have any peaks associated with the Ni-PS phase. As the solution pH increased to 8.3, the silica-Ni-pH 8.3 pattern has both the fcc-Si peaks along with very weakly intense peaks for Ni-PS, corresponding the presence of both the fcc-Si and a small amount of Ni-PS phase in this sample. The silica-Ni-pH 10.6 and pH 11.8 samples have more intense peaks corresponding to the Ni-PS phase, and very weak peaks corresponding to fcc-Si. Thus, in this pH range, the Ni-PS is the major phase present in the powder samples.

TEM images of the silica-Ni samples are displayed in Figure 5.5, and representative TEM images of the silica samples are displayed in Figure 5.6. The silica-Ni-pH 5.9 sample in Fig. 5.5a has mostly amorphous silica with large spherical particles ∼50 nm in diameter, decorated with small ∼1.5 nm particles, which are more visible in the inset of Fig. 5.5a. These small particles are most likely comprised of silicon or silica, since this morphology is similar to that of the silica-pH 10.5 TEM image in Fig. 5.6, and due to very low nickel loading in the pellet (Fig. 5.2a). In the silica-Ni-pH 10.6 and pH 11.8 samples (Figure 5.5c–d), the morphology transformed from the mostly amorphous silica and spherical particles in Figure 5.5a to that of Ni-PS phase. The crinkly-like morphology of the Ni-PS visible in the insets of Figure 5.5c and d is consistent with the morphology of Ni-PS from previous

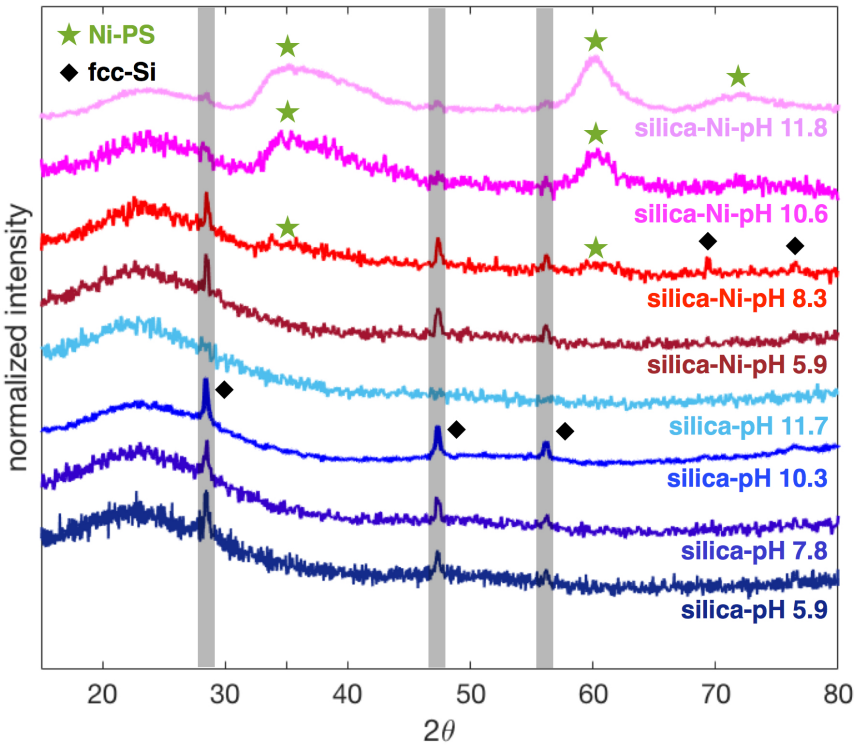

Figure 5.4: XRD patterns of silica and silica-nickel samples prepared from different precursor pH solutions.

reports.[24,178,202,204,205] The silica-Ni-pH 8.3 sample has a combination of amorphous silica and the Ni-PS structure, as seen in the inset of Figure 5.5b. The morphology of the samples from TEM corroborate the XRD patterns in Fig 5.4, and confirm that increased solution pH results in the formation of an ill-crystallized Ni-PS structure.

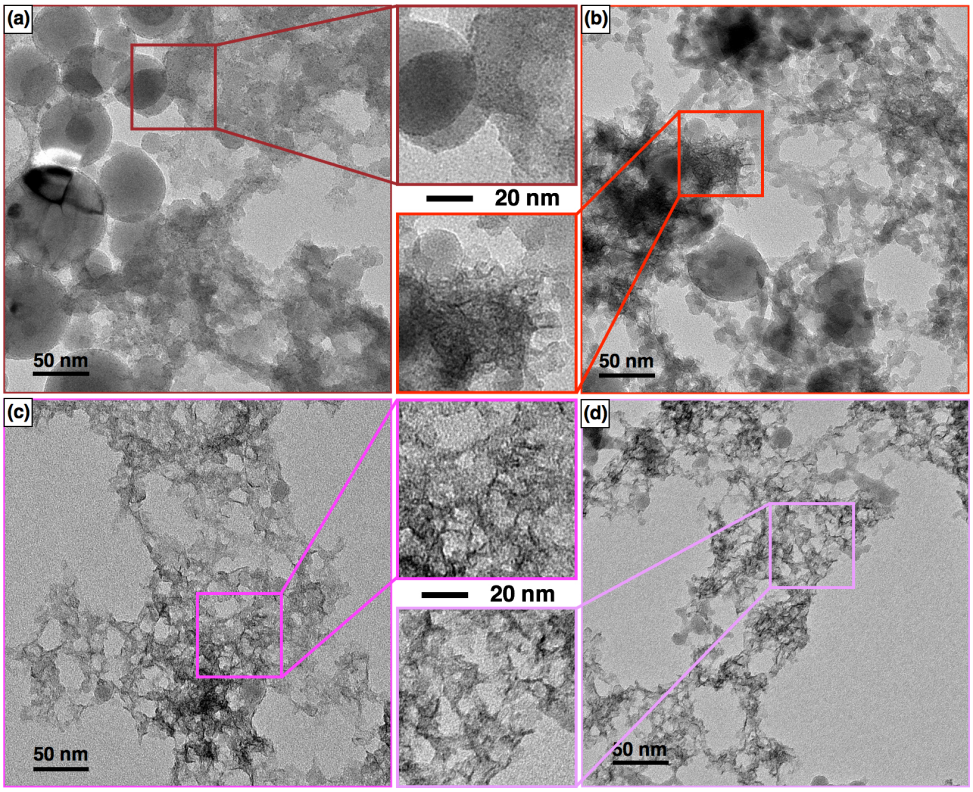

Figure 5.5: TEM images of silica-Ni samples at pH 5.9 (a), 8.3 (b), 10.6 (c), and 11.8 (d).

FTIR spectra are displayed in Figure 5.7 with inset (a) focusing on the ν(OH) stretching region and (b) focusing on the Si–O and δ(OH) bending region. The silica-pH 7.8 is displayed as a representative spectrum of the silica-only samples, as they were similar across the pH range, and are provided in Appendix D. The FTIR spectra of silica-pH 7.8 and silica-Ni-pH 5.9 were similar, with absorbance bands corresponding to the isolated OH groups of the silica support (3745 cm^{-1}), and the asymmetric ($\sim$1075 cm^{-1}) and symmetric (800 cm^{-1}) stretching bands of Si–O of the SiO_4 tetrahedra in silica.[193,196,205] This result suggests that the key components in the silica-Ni-pH 5.9 correspond to the silica support, with no features consistent with nickel-containing phases. The silica-Ni-pH 8.3 spectrum had peaks at 3745 cm^{-1}, 1075 cm^{-1} and 800 cm^{-1} that resembled the silica-7.8 and silica-Ni-pH 5.9 spectra. An additional absorbance at 670 cm^{-1} was identified that was not observed in the two other

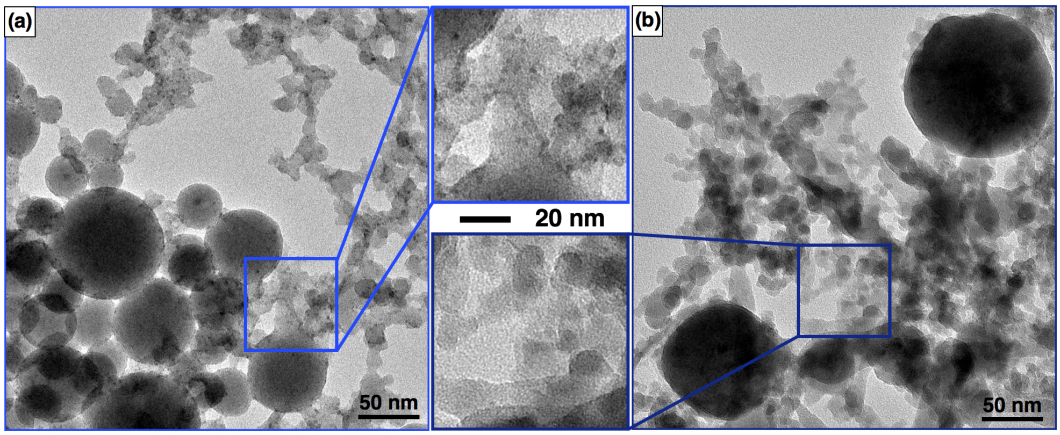

Figure 5.6: TEM images of silica NPs generated at pH 10.5 (a) and in water at pH 5.9 (b).

spectra, and corresponds to the δ(OH) bending mode of the 1:1 Ni-PS structure.[193,196,205] The silica-Ni-pH 10.6 sample lacks the 3745 cm^{-1} feature, exhibits a decrease in absorbance at 800 cm^{-1}, and has a shift in the 1075 cm^{-1} peak to 1020 cm^{-1}. These spectral features are consistent with the disappearance of the isolated OH groups of silica and the formation of Si–O–Ni bonds of Ni-PS. The observed 1020 cm^{-1} frequency corresponds to the 2:1 Ni-PS phase; the 1:1 Ni-PS phase would be expected at 1005 cm^{-1}.[196,206] The silica-Ni-pH 10.6 sample also exhibits a new broad feature around 650 cm^{-1}. This feature could arise from the δ(OH) bending mode of a 1:1 Ni-PS phase at 670 cm^{-1}, an ill-crystallized α-Ni(OH)$_2$ structure at 640 cm $^{-1}$, or both.[15,196,204] In the silica-Ni-pH 11.8 spectrum, this feature has an even more asymmetric absorbance in the 640 cm^{-1} range than near 670 cm^{-1}, which suggests a greater contribution from Ni(OH)$_2$. The silica-Ni-pH 11.8 also contains a small but sharp peak at 3645 cm^{-1} (inset (a)), corresponding to the ν(OH) stretching vibration in either the 1:1 Ni-PS phase or in β-Ni(OH)$_2$.[15,196]

To determine the origin of the sharp peak at 3645 cm^{-1} in the silica-Ni-pH 11.8 spectrum, the precursor Ni(NO$_3$)$_2$ solution was centrifuged and dried (13,000 rpm, 90 min) and the FTIR spectrum of the collected powder is displayed in Fig. 5.7 (Ni(OH)$_2$ (synth.)). This spectrum has a sharp peak at 3640 cm^{-1}, confirming that this feature in the silica-Ni-pH 11.8 spectrum is due to unreacted, precipitated Ni(OH)$_2$ from the precursor. Additionally, the absorbance in inset (b) of Figure 5.7 of the Ni(OH)$_2$ (synth.) spectrum is near 520 cm^{-1}, consistent with the δ(OH) bending mode of the β-Ni(OH)$_2$ phase.[15,196] Thus, the absorbance band of the silica-Ni-pH 8.3, pH 10.6, and pH 11.8 samples near 640 cm^{-1} likely arise

from the $Ni(OH)_2$ phase. The precursor solution pH increase from the silica-Ni-pH 8.3 to the silica-Ni-pH 11.8 samples presents shifts in absorbance intensity and frequency that are consistent with the formation of Ni-PS and $Ni(OH)_2$. The silica-Ni-pH 11.8 sample also contains some unreacted, β-$Ni(OH)_2$, as evidenced by the spectrum of its dried precursor.

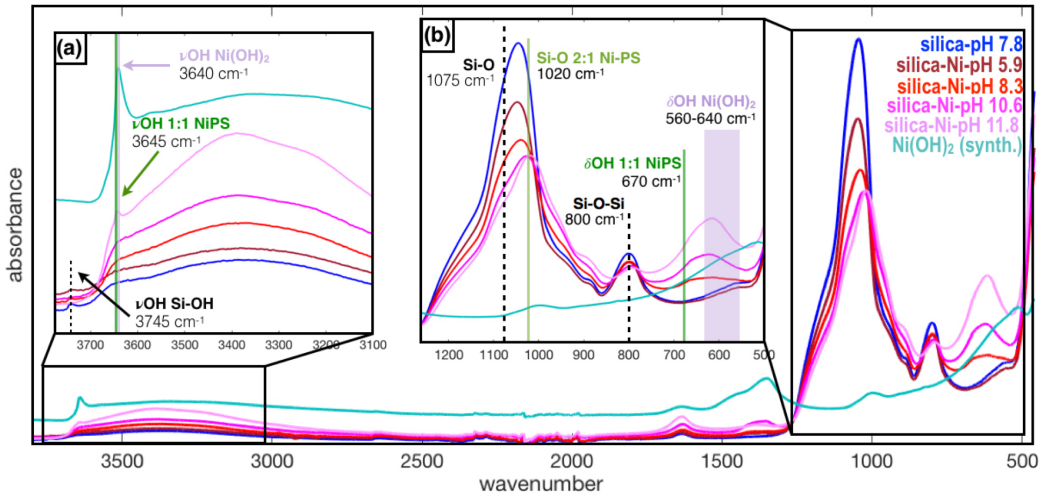

Figure 5.7: FTIR spectra of silica and silica-nickel samples prepared from different precursor solution pH.

The $Ni2p_{3/2}$ atomic orbital spectra obtained with XPS from silica-Ni-pH 8.3, 10.6, and 11.8 are displayed in Figure 5.8. No Ni was detected in the silica-Ni-pH 5.9 sample. In all three samples the surface Ni atoms possess a Ni^{2+} charge state due to lack of features in the range of Ni^0 (852.7 eV).[207] The silica-Ni-pH 10.6 and 11.8 spectra are fit with two peaks assigned to the 1:1 and 2:1 Ni-PS phases, and the silica-Ni-pH 8.3 spectrum was fit with one peak at 855.3 eV assigned to the 1:1 Ni-PS phase.[15,205,207] Because the binding energy of $Ni(OH)_2$ at 855–856 eV overlaps that of the 1:1 Ni-PS phase (885.5 eV), it is difficult to definitively assign the peaks in this binding energy range. The similar binding energy of $Ni(OH)_2$ to that of the Ni in 1:1 Ni-PS is due to the octahedrally coordinated Ni^{2+} to both Ni-O-Si and Ni-OH bonds in the 1:1 structure as seen in Figure 5.1. While it is difficult to definitively assign surface Ni species to $Ni(OH)_2$ or Ni-PS with XPS, the the spectra of the silica-Ni-pH 10.6 and 11.8 samples are consistent with Ni-PS phases observed with XRD, TEM, and FTIR.

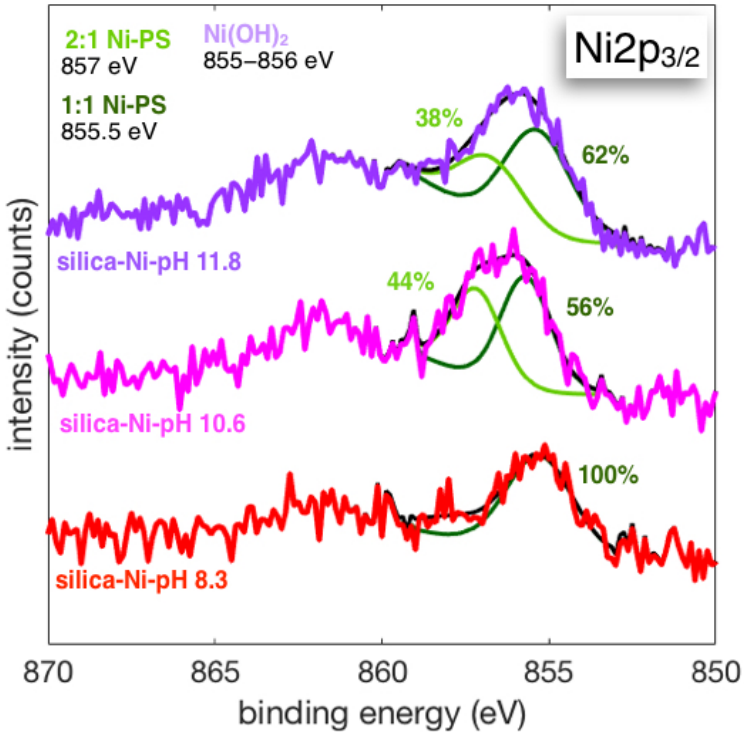

Figure 5.8: High resolution XP spectra of $Ni2p_{3/2}$ atomic orbital for silica-Ni samples prepared at different pH solutions.

5.2.3 Discussion

Analysis of solution phase silicate species generated from laser ablation and characterization of the nickel-containing products revealed that silicic acid is the key species generated under alkaline conditions (above pH 10) that reacts with nickel cations in solution to form Ni-PS. When no KOH was added to the nickel nitrate precursor solution, no silicic acid was generated, and a Si-O-Ni monomer was the major product that remained in solution. The generation of the silicic acid at high solution pH conditions drove the decrease in solution pH after laser irradiation, independent of the addition of nickel nitrate to the precursor. The magnitude of solution pH decrease after irradiation corresponds to the relative amount of silicic acid generated. Solutions of pH ~6 had no drop in pH after irradiation, and no peak at 95 m/z in the ESI-MS. The samples with initial pH ~10.6 and ~11.8 decreased to ~8.6 and ~9.9, respectively, while the intermediate pH ~8 dropped only one pH unit, suggesting that a smaller amount of silicic acid was generated in this pH range. Analysis of the dried silica-Ni powders confirmed that silicic acid is the major species driving the formation of Ni-PS. The silica-Ni-pH 5.9 sample had nearly identical FTIR and XRD features as the silica-only

samples, while the silica-Ni-pH 10.6 sample exhibited distinct features consistent with Ni-PS. The silica-Ni-pH 8.3 sample had a mixture of XRD, FTIR, and TEM features to that of the silica-Ni-pH 5.9 and the silica-Ni-pH 10.6 samples, consistent with the availability of less silicic acid for Ni-PS formation.

It should be noted that the formation of nickel hydroxide ($Ni(OH)_2$) is common at high solution pH, and precipitates above pH 9.[196] Because the silica-Ni-pH 11.8 sample dropped to a pH of 9.9 after laser irradiation, any unreacted nickel in the solution was likely incorporated in the dried pellet as precipitated $Ni(OH)_2$. FTIR analysis of the dried silica-Ni-pH 11.8 precursor confirmed the presence of β-$Ni(OH)_2$ in the irradiated silica-Ni-pH 11.8 sample. Thus, the 29.3 wt.% Ni in the dried powder represents both the Ni-PS and some unreacted β-$Ni(OH)_2$. In contrast, the 23.1 wt.% Ni in the silica-Ni-pH 10.6 sample represents the Ni-PS phase, since the final solution pH of 8.6 is below the precipitation point of $Ni(OH)_2$, as evidenced by the 127 m/z peak corresponding to hydrated $Ni(OH)_2$ in the supernatant via ESI-MS.

The majority of synthesis approaches to Ni-PS include deposition-precipitation (D-P) and hydrothermal treatments, where the silica source (silicic acid, sodium silicate, fumed silica) is mixed with the nickel precursor ($NiCl_2$, $Ni(NO_3)_2$), and the solution pH was controlled by addition of urea. Investigations on the effect of the Si/Ni ratio, specific surface area (SSA) of the silica precursor, and D-P reaction time have lead to the observations that the Si/Ni ratio, the solution pH, and SSA of the silica source affected the relative yields of $Ni(OH)_2$ as compared to 1:1 or 2:1 Ni-PS structures.[24,195,196,199,206] Low SSA silica formed $Ni(OH)_2$ over silica in one report[196] and $Ni(OH)_2$ with 1:1 Ni-PS in a separate report.[195] High SSA silica and solution pH formed 2:1 Ni-PS, as long as the pH was below the $Ni(OH)_2$ precipitation threshold.[195,196,206]

In this work, silicic acid was generated directly *in situ* through the laser ablation process, wherein ejected silicon atoms form silicic acid upon interaction with solution. The silicic acid monomer was only observed in ESI-MS in the high pH samples of the silica-pH 11.7 and silica-Ni-pH 10.6 samples. In the two samples prepared at pH ~6, a metasilicate species was identified in ESI-MS, which was attributed to the $[(H_2O)_5NiOSi(H_2O)_2O]^-$ monomer formation. Previous reports on the formation mechanism of Ni-PS structures have suggested that silicic acid or its deprotonated $(OH)_3SiO^-$ form is responsible for the formation of this

$[(H_2O)_5NiOSi(H_2O)_2O]^-$ monomer, which was suggested as an intermediate species in Ni-PS formation.[24,195,196,199,206] Our data do not support the above hypothesis, but suggest that the metasilicate species is responsible for forming the $[(H_2O)_5NiOSi(H_2O)_2O]^-$ monomer, which is not a Ni-PS intermediate. The silicic acid formed at high pH instead drives the Ni-PS formation. Figure 5.9 displays a summary of these proposed reaction processes and the resulting solid products.

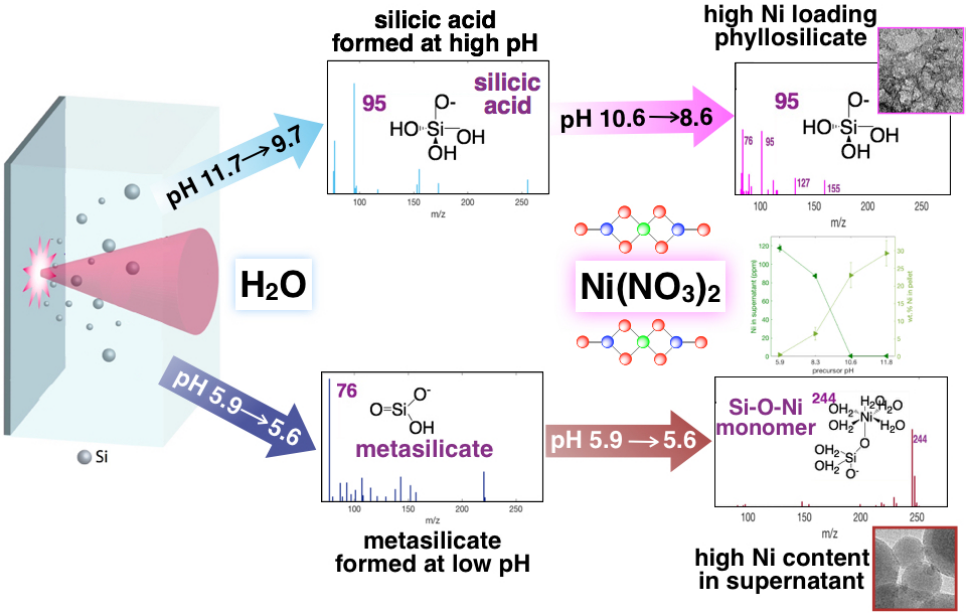

Figure 5.9: Proposed reaction mechanisms based on dissolved species generated from silicon wafer ablation in various solutions.

In the previous chapter, Cu-PS formation was attributed to the silica clusters becoming deprotonated and attracting nearby $Cu_2(OH)_2^{2+}$ complexes due to strong electrostatic attraction.[197] However, the findings from this investigation identify the silicic acid as the primary driver of metal-phyllosilicate formation. The formation of both Cu-PS in the previous chapter and the Ni-PS in this one demonstrate a general method of metal-phyllosilicate synthesis using a laser ablation in liquid technique. The key to successfully preparing metal-phyllosilicates requires that the solution have a high enough pH to induce silica dissolution generating silicic acid that may interact with the divalent metal cations. Because both copper nitrate and nickel nitrate formed Cu-PS and Ni-PS under similar experimental conditions, the specific metal salts used do not appear to play as large of a role in the metal-phyllosilicate formation as the ablated silicate species do. These results suggest that the laser ablation in liquid technique can become a versatile route to a variety of metal phyllosilicate materials with very high metal loadings. These materials are expected to provide exceptional thermal

stability and high activity for catalytic applications.

5.3 Conclusion

The synthesis of nickel-phyllosilicate with 23 wt.% Ni was achieved using the fs-RLAL method by ablating a silicon wafer immersed in nickel nitrate solutions under alkaline conditions. Analysis of the supernatants of irradiated solutions revealed that silicic acid was the key species driving the nickel-phyllosilicate formation when the solution pH was above 10. The generation of silicic acid led to a decrease of solution pH by two pH units after laser irradiation. In contrast, for irradiated solutions of nickel nitrate and water at ∼pH 6, the solution pH did not change after irradiation, no silicic acid was detected in the supernatants, and nearly no nickel was detected in the dried powder. Instead, a metasilicate species as the major product in when the silicon wafer was ablated in water, while a Si-O-Ni monomer was the major species detected when nickel nitrate was added to the solution. The results from this work and the previous chapter identify a general mechanism of metal-phyllosilicate synthesis using laser ablation liquid under alkaline conditions. The metal cation complex does not appear to play a large role in metal-PS formation, but rather the solution pH drives the metal-PS formation due to the silicic acid generated from the ablation process. This synthesis method may be applied to other divalent metal cations to fabricate metal-phyllosilicates that may be used for catalytic applications.

Chapter 6

Conclusions and Future Work

6.1 Conclusions

This work focused on the synthesis, characterization, and understanding the formation mechanisms of novel metal-oxide nanostructures generated from a femtosecond reactive laser ablation in liquid technique. The first project focused on preparing a silica-Au nanomaterial containing two populations of Au NPs which reflected two distinct reaction mechanisms. The larger, 7.0 nm Au NPs formed from the electrons generated from water photolysis and in the ablation plasma. These reactions occurred on shorter timescales following the laser pulse, leading to more time for the nearby $[AuCl_4]^-$ complexes to reduce, nucleate, and grow into the larger Au NPs. Alternatively, the second population of 1.5 nm Au NPs dispersed throughout the silica matrix were formed from the surface reactions which occurred on longer (several hundred ps) reaction timescales following the laser pulse. These surface reactions involved the Si atoms and clusters ejecting out of the crystal lattice of the Si wafer due to Coulombic repulsion, and interacted with the nearby $[AuCl_4]^-$ complexes in solution. As the Si clusters coalesced they oxidized to form silica, and acted as nucleation sites for the Au clusters to form. The small Au NPs dispersed throughout the silica matrix was due to either the depleted Au concentration after a significant portion of the Au ions formed the isolated Au NPs, or due to the coalescing silica matrix forming around the Au clusters.

Next, the same experimental technique was carried out to generate silica-Cu nanostructures by ablating a silicon wafer immersed in solutions containing $Cu(NO_3)_2$. Modifying the precursor pH (pH $3-10$) led to the realization that when the solutions' pH values were below the point of zero charge (PZC) of silica (pH $\sim$4), the ablated silica clusters possessed a positive surface charged due to the protonated surface hydroxyl groups. The protonated

silica clusters and the Cu^{2+} cations in solution electrostatically repelled each other, forming Cu-core/silica-shell nanoparticles due to the phase segregation. Alternatively, when the precursor pH was significantly higher than the PZC value (at pH 10.6), the ablated silica clusters became deprotonated in solution where strong electrostatic attraction with the nearby $[Cu(OH)_2]^{2+}$ clusters formed a copper-phyllosilicate (Cu-PS) structure with 2.70 nm Cu_2O clusters dispersed throughout the Cu-PS. The findings from this project highlight the importance of understanding the inherent properties of the target material and the chemical transformations it undergoes when it is ablated in different pH solutions. Therefore, this project demonstrated the ability to fabricate very different morphology products using the same experimental setup, by simply modifying the precursor pH.

The last project investigated the dissolved silica ablation products generated in water and nickel nitrate solutions over a range of pH conditions. When the supernatants of irradiated solutions were analyzed via ESI-MS, silicic acid was the major product formed when the precursor pH was above pH 10. This silicic acid species contributed to a two-pH unit decrease after laser irradiation, in both water and nickel nitrate solutions. Additionally, the silicic acid was determined to be the key compound driving the formation of nickel-phyllosilicate in alkaline conditions. In contrast, when silicon was ablated in water and nickel nitrate solutions near pH 6, no silicic acid was detected and no significant change in pH was observed. A deprotonated metasilicate species was detected in the water supernatant, disappeared when nickel nitrate was added to the precursor solution, and a Si-O-Ni monomer was the major species detected. Characterization of the dried powders confirmed the formation of Ni-PS when the precursor was above pH 10, with 23 wt.% Ni in the silica-Ni-pH 10.6 sample. The results from this work identify a general mechanism of metal-phyllosilicate synthesis using laser ablation in liquid under alkaline conditions. This synthesis method may be applied to other metal cations to fabricate metal-phyllosilicates for a range of catalytic applications.

The findings from this work provide a general synthesis method for preparing silica-metal composite nanomaterials comprised of high metal loading using a laser-assisted synthesis technique. Identifying the key silicate species involved in the synthesis of nickel-phyllosilicate demonstrates the ability to control the reactive species generated in an ablation plasma by modifying the precursor pH. These findings will contribute to reliable design of composite nanostructures with high metal loading for a variety of catalytic applications.

6.2 Future Work

The laser energy used in these experiments was far above the ablation threshold of silicon, resulting in large spherical polycrystalline silica particles when ablated in water, which is consistent with other reports of PLAL of silicon in water.[209] In contrast, ablating a silicon wafer near its ablation threshold has been found to form small, uniformly spherical Si NPs.[210] I am interested in first ablating a Si wafer near its ablation threshold (0.16 W cm^{-2} under our experimental conditions) to see if the small spherical Si NPs result, then carrying out similar experiments with the silica-Cu and silica-Ni (chapters 4 and 5) to see if the low laser intensity affects the product morphology. It is likely that the phyllosilicate material will be the major product if silicic acid is generated under alkaline solutions, but at lower pH conditions will the core-shell morphology still form?

Preliminary studies of combining copper and nickel nitrate salts into alkaline precursor solutions have been tested for their catalytic activity toward PNP. There was a distinct effect of the Ni:Cu ratio in the precursor to the PNP rate constant. First, the 1:0 Ni:Cu product had nearly no catalytic activity toward PNP, with a near-zero rate constant, and the 0:1, 1:2, 1:1, and 2:1 Ni:Cu ratios were compared. Interestingly, the 2:1 Ni:Cu had the highest catalytic rate constant of all samples tested. Characterization of the products have yet to be done, and will provide insight into the nature of this ratio-dependent catalytic activity. A possible hypothesis as to the nature of the highest catalytic rate constant of the 2:1 Ni:Cu product is due to the different redox potentials of nickel and copper. Copper has a higher redox potential (Cu^{2+}/Cu^{1+}, +0.16 V)[211] than nickel (Ni^{2+}/Ni^{0}, -0.26 V), leading to copper ions reducing more easily than the nickel ions. As a result, during laser ablation the Ni^{2+} may remain unreduced, acting as anchoring sites for Cu_2O nanoclusters from the partially reduced Cu^{1+} sites. Characterization with TEM, XPS, XRD, ICP-OES, FTIR and SEM-EDX will provide data to better understand how the Ni and Cu are bonded together and with the ablated silica.

Metal-phyllosilicates have been reported to possess varying morphology including plate-like structures, nanotubes, and nanoscrolls.[24,203,212,213] The asymmetry of the inner and outer octahedral and tetrahedral sheets can be modified by selecting different cations, resulting in varying degrees of curvature. These nanotubes and nanoscroll structures have promising applications in catalysis,[24,214] gas adsorption and storage,[214] drug delivery,[215] and as anode support material for lithium ion batteries.[216] For example, incorporating aluminum into the

phyllosilicate structure can form a nanotube possessing Al(OH)Al outer groups and SiOH inner groups, promoting both shape specific reactivity and charge separation between the inner (SiO^-) and outer ($Al(OH)_2^+$) groups.[214] Thus, highly selective catalytic materials may be prepared by incorporating aluminum ions or preparing different stoichiometries of nickel in phyllosilicate materials to promote the nanotube morphology.

This work focused on the complex chemistry involved in fs-RLAL of silicon immersed in various metal salt solutions, leading to the synthesis of a variety metal-silica nanocomposites for catalytic applications. The simple and versatile fs-RLAL experimental setup allows for efficient exploration of various support materials including zinc, titanium, and aluminum. The large bandgaps of zinc oxide and titanium dioxide make these supports promising candidates for photocatalytic applications; in a recent study, zinc oxide-copper(I) oxide nanoparticles were reported to have high selectivity toward methanol formation from CO_2.[217] In another study, TiO_2—CuO_x and TiO_2—FeO_x composites generated from a laser ablation technique had photocatalytic activity toward 2,4-dichlorophenoxyacetic acid degradation under solar irradiation.[218] Ideal nanocatalysts have high surface area, high metal loading, and have a support material with high electrical conductivity. One of the parameters identified in this work that contributes to high metal loading is the point of zero charge (PZC) of the support material; by changing the solution pH to allow for high electrostatic attraction between the ablated support species and the metal ions in solution has been shown to form high metal loading in the final product. While silica has a PZC at pH 4, carrying out fs-RLAL at high solution pH resulted in high metal loading; however, ZnO has a PZC around pH 9.[219] To drive deprotonation of the ablated ZnO clusters for electrostatic attraction with the metal ions in solution, increasing the solution pH to well above pH 11 is anticipated. Alternatively, fs-RLAL in solutions containing metal *anions* below pH 9 may also drive electrostatic attraction between the protonated ablated ZnO clusters and the metal anions. Additionally, carrying out ESI-MS on the supernatants of the ablated support material over a range of pH conditions and tracking the pH change after laser irradiation helped determine pH-dependent species formed from the support material that aided in the formation of distinctly different products. These examples demonstrate the ability to prepare a range of support-metal nanocomposite materials tailored to the specific catalytic reaction of interest, and considering the solution-based parameters outlined in this work to guide the selection of solution composition around the support material properties.

Appendix A

Appendix A

Link back to chapter 2.

A1 UV-vis Spectra to Determine Irradiation Time

To monitor the reduction of $[AuCl_4]^-$ to form silica-Au NPs, the sample cuvette containing the silicon wafer immersed in the $KAuCl_4$ solution was placed in a UV-vis spectrometer described in detail elsewhere.[47] Spectra were collected in between irradiation periods of 2–8 min, and inspected to determine full conversion of $[AuCl_4]^-$ to silica-Au NPs. Figure A1a shows overlaid UV-vis spectra of a representative sample irradiated with 50 μJ laser pulses in 2 minute increments for 8 minutes. Significant growth of a peak around 520 nm occurs between 2 min and 4 min; this corresponds to the surface plasmon resonance (SPR) of spherical AuNPs 5–20 nm in diameter forming.[220] The grey spectrum in Fig A1a corresponds to a colloidal solution of SiO_2 particles formed from ablating a silicon wafer immersed in water for 8 min, under the same experimental parameters. The control Au NPs required 600 s of irradiation for full conversion of the $KAuCl_4$ to Au NPs. In situ UV-vis absorbance measurements at 450 nm were used to track the conversion, since that wavelength corresponds to the growth of Au NPs, without absorbance contributions from either the precursor or the surface plasmon resonance (SPR) from the Au NPs.[46,47,74] Figure A1b shows the final spectrum of the control Au NPs, with an inset of the growth at 450 nm over time.

A2 Para-Nitrophenol Reduction

The catalytic activity of the silica-Au NPs and control Au NPs were tested with the model PNP reduction by $NaBH_4$ reaction.[120,221,222] The in situ UV-vis setup used for this reaction is

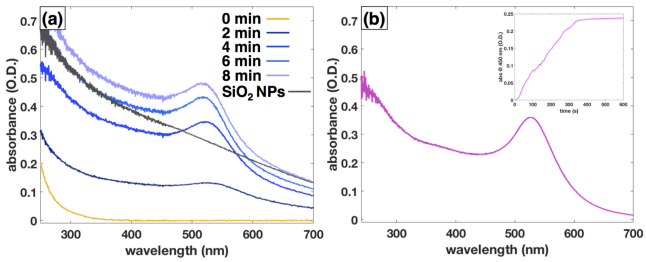

Figure A1: UV-vis spectra of silica-Au NPs after incremental laser irradiation and spectrum of silica (SiO_2) NPs generated from ablating a Si wafer in water for 8 min. (a) Final spectrum of control Au NPs; inset shows in situ UV-vis absorbance recorded at 450 nm to show growth of Au NPs (b).

described in further detail in the main article (Section 2.4). The reduction of PNP by NaBH4 takes place on the surface of the metal nanoparticles, and can be described by Langmuir-Hinshelwood kinetics.[111,221] Equation A.1 displays the kinetic rate equation,

$$\frac{\mathrm{d}c_{PNP}}{\mathrm{d}t} = k_{\mathrm{app}} c_{\mathrm{PNP}} \tag{A.1}$$

where k_{app} is the rate constant (s^{-1}), and c_{PNP} is the concentration of PNP (mM).[120] Since the $NaBH_4$ is in excess, the reaction assumes pseudo first-order kinetics, so the concentration of PNP and the surface area of the catalyst are the kinetic driving forces. Integrating Eq. A.1 gives

$$\ln \frac{c_t}{c_0} = -kt \tag{A.2}$$

which allows for the k_{app} rate constant to be determined by plotting $\ln\frac{A_{400}}{A_i}$ over time (A_i is the initial absorbance of the p-nitrophenolate ion at 400 nm before the catalyst is added) and extracting the slope. Figure A2b displays the UV-vis absorbance of the p-nitrophenolate ion over time (at 400 nm), where the black portion of the line represents the linear region in which the kapp rate constant is extracted. The k_{app} rate constant was converted to units of $\mathrm{s}^{-1}\mu$mol Au^{-1} by dividing by the amount of gold added to the reaction, yielding the rate constant referred to as k_{Au} in the main text. Plotting k_{app} as a function of μmol Au added to the reaction demonstrates a linear relationship, displayed in Fig. A2c. The SSA-normalized rate constant k_1 (L $\mathrm{m}^{-2}\mathrm{s}^{-1}$) was determined by dividing the kapp value by the SSA.

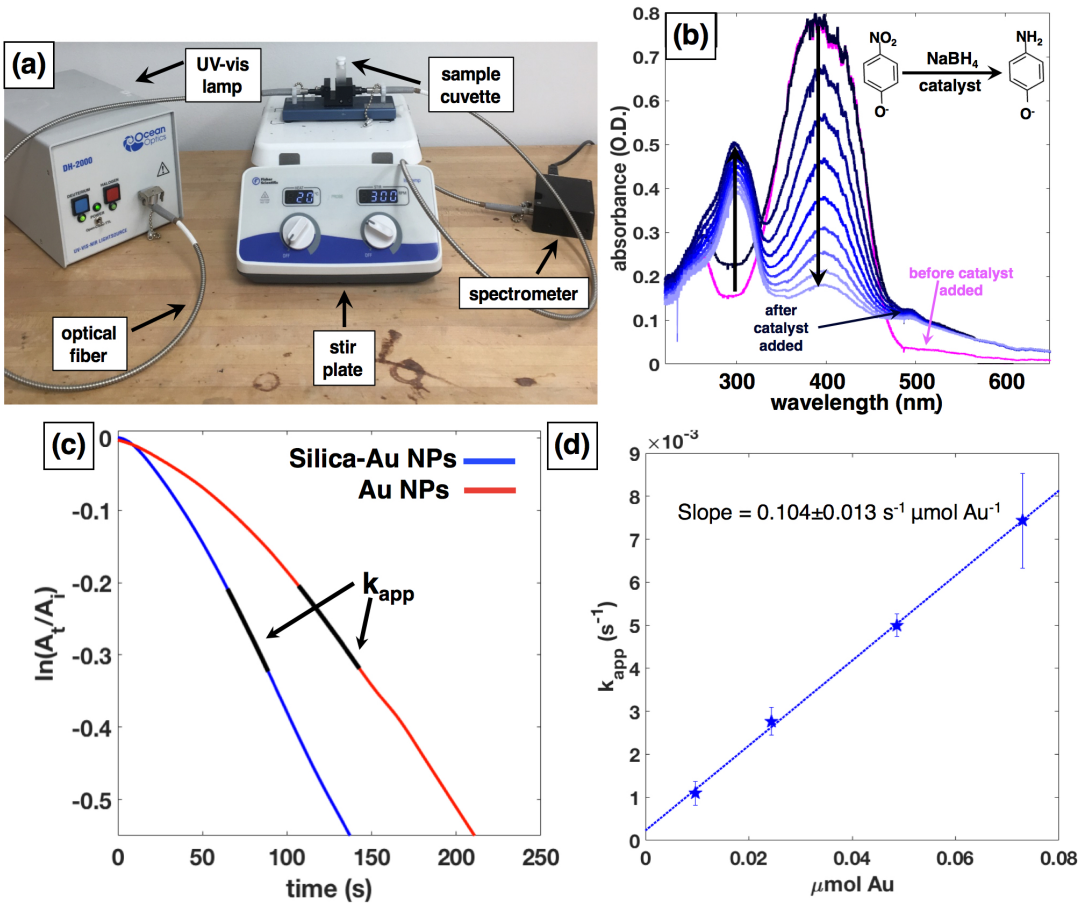

Figure A2: Absorbance spectrum of PNP reduction by $NaBH_4$. Decrease of p-nitrophenolate ions (black arrow) at 400 nm, and increase of p-aminophenol product (blue arrow) shown (a). Typical time dependence of the absorbance of p-nitrophenolate ions at 400 nm; black portion of line is where k_{app} (s^{-1}) is extracted for silica-Au NP and Au NP samples (b). k_{app} plotted against μmol Au in solution yields k_{Au} rate constant ($s^{-1}\mu mol\ Au^{-1}$) (c).

Appendix B

Appendix B

Link back to chapter 3.

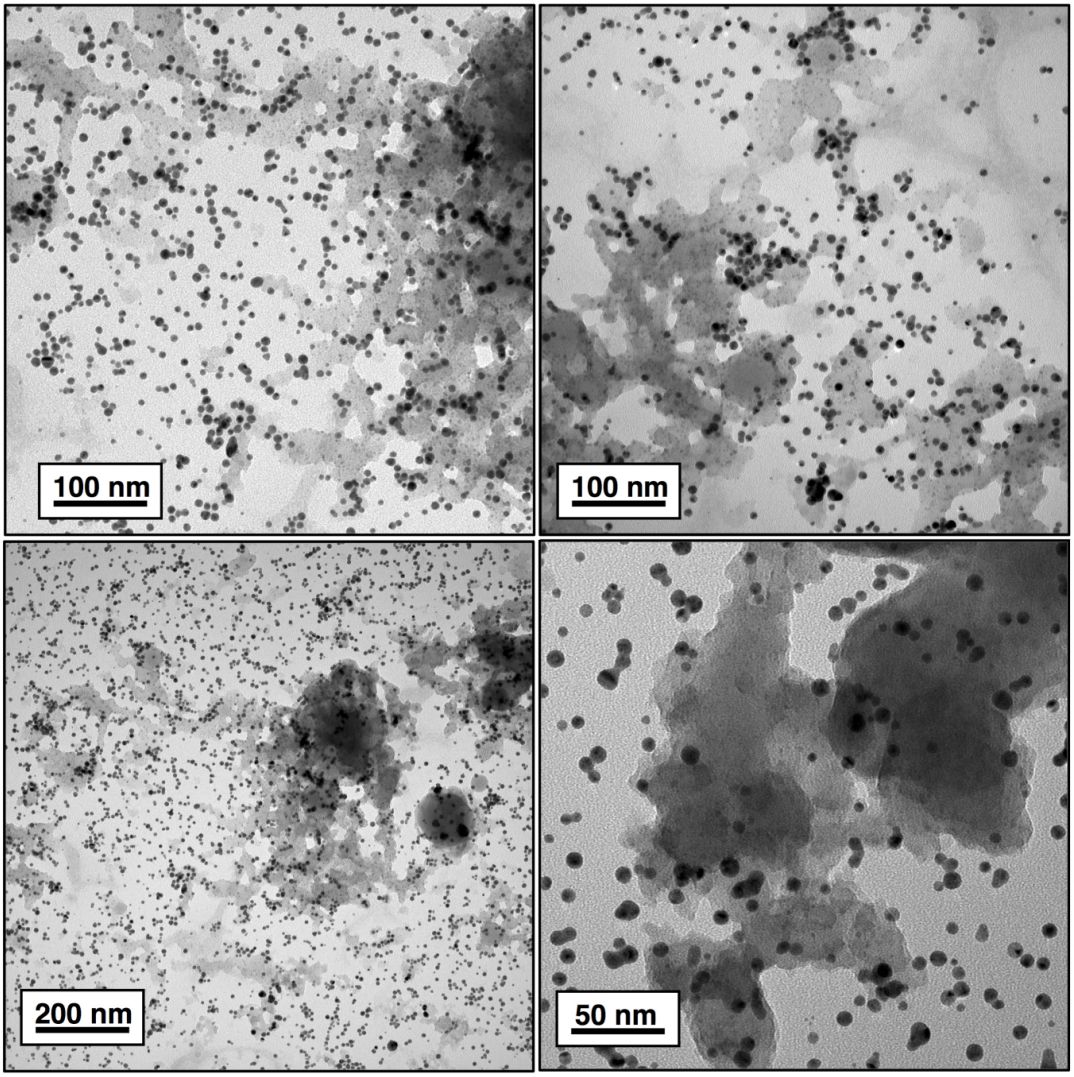

Figure B1: TEM images of silica-Au NPs at different magnifications.

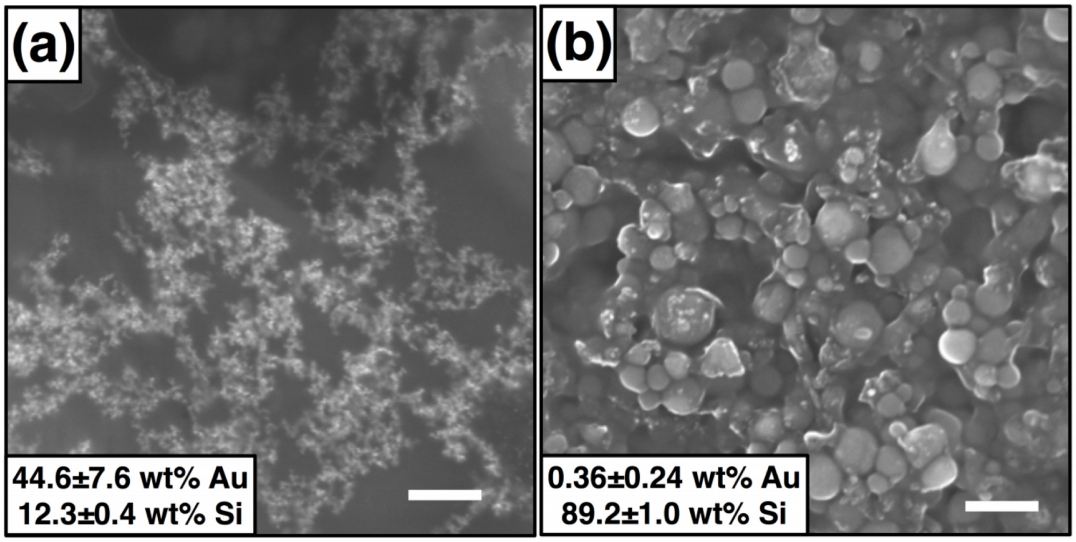

Figure B2: SEM image with wt.% of Au and Si from EDX analysis of supernatant of silica Au NPs (a) and control SiO_2 NPs prepared by ablating a silicon wafer immersed in water (b). Scale bar represents 200 nm.

B1 Characterization of Silica NPs

Silica nanoparticles were synthesized as an ablation control, where a silicon wafer was ablated in water under the same laser parameters as with the silica Au NPs. The UV-vis spectrum of the colloidal silica solution is displayed in Fig A1a (grey spectrum), and the corresponding TEM, HRTEM with lattice spacings and FFT are displayed in Figures B3a and b. The lattice spacings of 3.05 , 1.91 , and 1.6 correspond to the (111), (220), and (311) crystal planes of silica. Although the silica particle in Figure B3b displays polycrystalline structure, other amorphous silica particles are observable in the TEM image in Fig B3a, suggesting different ablation mechanisms and formation dynamics occurring.

B2 Nanoparticle Surface Area Calculations

Representative values reported in Table 3.2 of the main text are from the weighted mean silica-Au NP diameter, calculated from the wt.% of Au detected from SEM-EDX measurements of the pellet and supernatant samples. Mean NP sizes of the stabilized Au NPs (1.94±0.7 nm) and isolated Au NPs (7.0±2.0 nm) were calculated experimentally from the size distribution measured by TEM and analyzed with ImageJ software (Fig. 3.1 in main text). The weighted mean diameter of the two populations in the silica Au NP sample was calculated using the wt.% of Au quantified using SEM-EDX of the centrifuged pellet (8.7

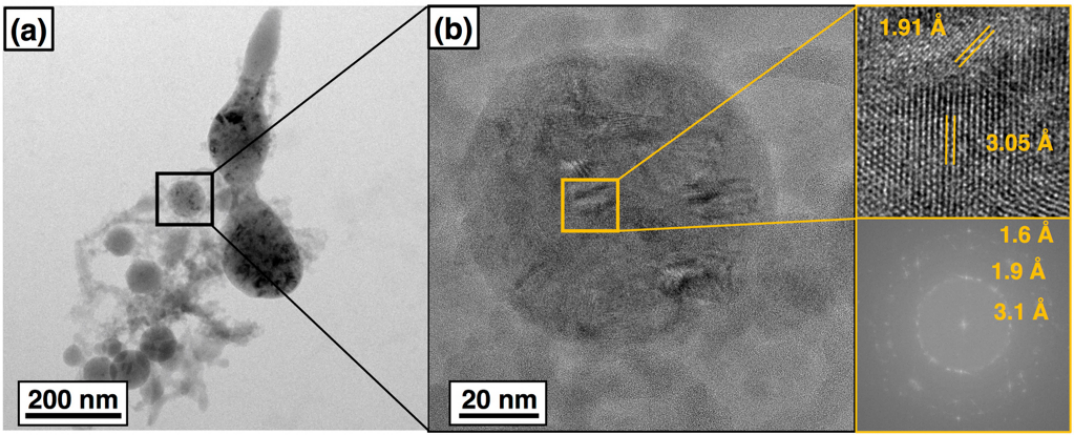

Figure B3: TEM images of silica NPs generated from ablating a silicon wafer immersed in water (a). HRTEM with FFT and lattice spacings of silica NPs (b).

wt.%) and supernatant (SN, 44.6 wt.%).

$$\%\ \text{stabilized Au NPs} = \frac{8.7}{8.7+44.6} = 16.3\% \tag{B.1}$$

$$\%\ \text{isolated Au NPs} = \frac{44.6}{8.7+44.6} = 83.6\% \tag{B.2}$$

$$\text{weighted mean diameter (nm)} = (1.9 \times 0.163) + (7.0 \times 0.837) = 6.17 \tag{B.3}$$

The weighted mean diameter of 6.17 nm for the silica-Au NPs incorporates the percentage of small stabilized Au NPs and the larger isolated Au NPs. This value will be used in the representative calculations for the Surface Area (SA) and Specific Surface Area (SSA) calculations below.

$$\text{radius (r, cm)} = \frac{diam}{2} \times 10^9 = 3.08 \times 10^7 \tag{B.4}$$

$$\text{NP volume (cm}^3\text{)} = \frac{4}{3}\pi r^3 = 1.23 \times 10^{19} \tag{B.5}$$

$$\text{g Au NP}^{-1} = \text{NP vol.} \times \rho Au = 2.37 \times 10^{18} \tag{B.6}$$

$$\text{SA (m}^2\text{)} = 4\pi r^2 = 1.20 \times 10^{16} \tag{B.7}$$

$$\text{SSA (m}^2\text{L}^{-1}\text{)} = (\text{mM KAuCl}_4)(\text{MW}_{\text{KAuCl}_4})(51\text{wt\% Au in KAuCl}_4)\frac{NP}{gAu}(SA) = 0.97 \tag{B.8}$$

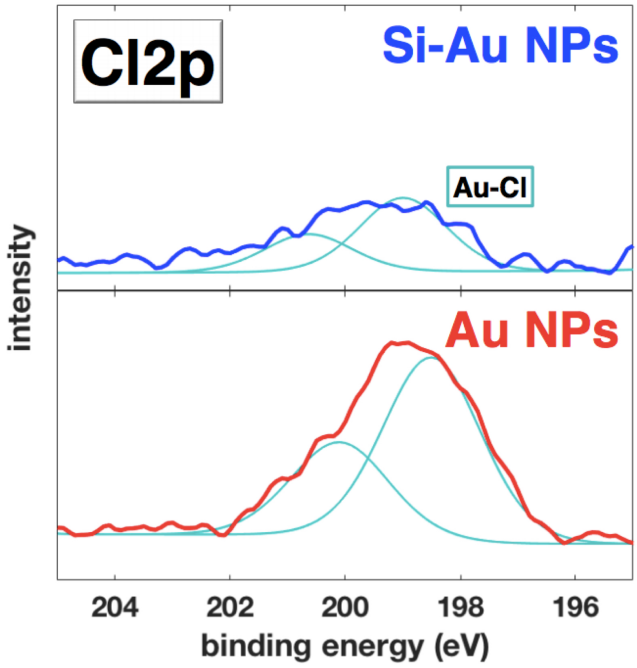

Figure B4: Cl2p XPS spectra of silica-Au NPs and Au NPs

Appendix C

Appendix C

Link back to chapter 4.

C1 Additional TEM Images

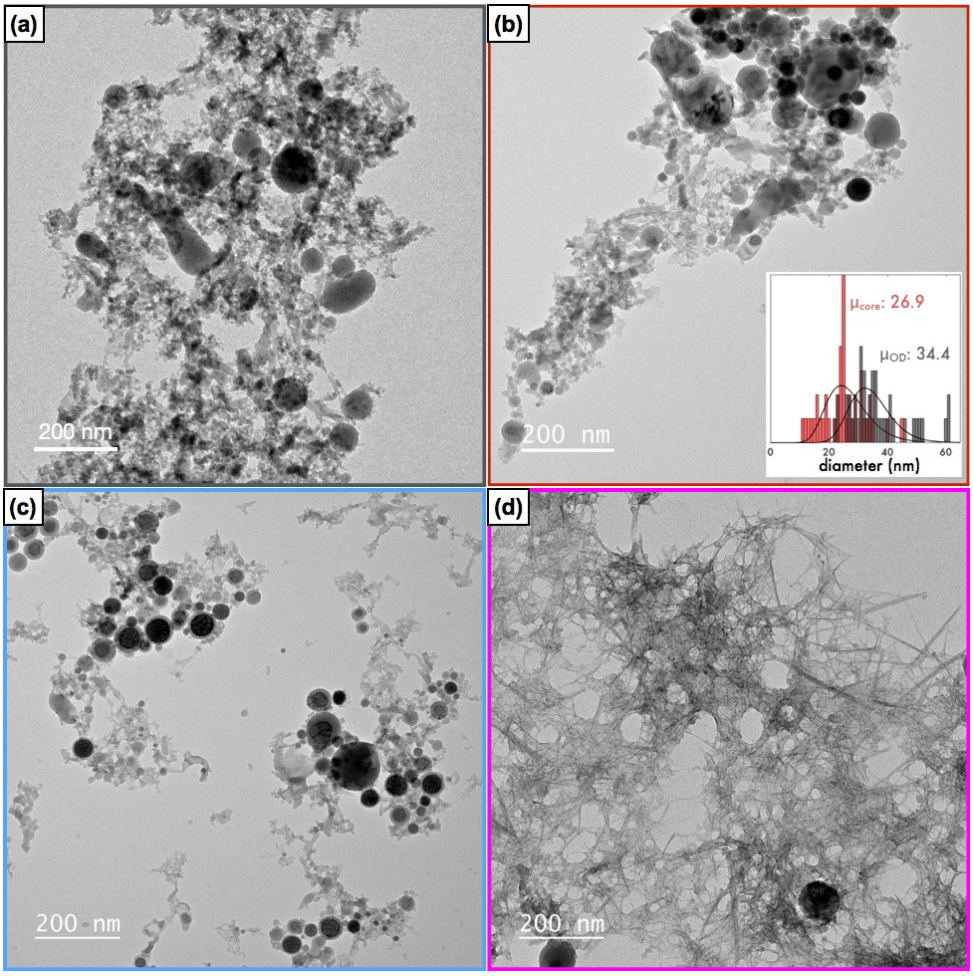

Figure C1: Additional TEM images of silica NPs from ablating a Si wafer immersed in water (a), Cu-silica-3.0 (b), Cu-silica-5.4 (c), and Cu-silica-10.4 (d).

C2 Converting At.% to Wt.% from XPS Quantitation

Atomic % is the output concentration from XPS quantitation, which was used to convert to wt.% for easier comparison with SEM-EDS and ICP-OES results. Table C1 displays the values from XPS in at.% and converted to wt.%; the following conversions were carried out. The example calculations include values from converting the atomic % of Cu in the Cu-silica-10.4 sample.

	Atomic %			Weight %		
Sample	Cu	Si	O	Cu	Si	O
Cu-silica-3.0	0.1±0.1	27.7±0.2	72.2±0.4	0.3±0.3	40.1±0.1	59.6±31
Cu-silica-5.4	0.8±0.6	33.4±9.3	65.8±8.6	2.6±2.0	45.9±0.9	51.5±6.8
Cu-silica-10.4	6.4±2.0	17.0±4.9	76.5±7.3	19.2±6.1	22.6±2.7	58.1±5.5

Table C1: Atomic % (left) determined from XPS quantitation (left) and converted to wt.% (right) based on equations below.

$$\text{g Cu in Cu-silica-10.4} = \frac{6.4 \text{ atoms Cu}}{100 \text{ atoms total}} \times \frac{1 \text{ mol Cu}}{6.022 \times 10^{23} \text{ atoms}} \times \frac{63.546 \text{ g Cu}}{1 \text{ mol Cu}} = 6.71 \times 10^{-24} \tag{C.1}$$

This calculation was carried out for O and Si in the sample, which were used to calculated the total g of Cu, Si, and O in the sample assuming 100 atoms, corresponding to 3.5×10^{-23} g total shown in equation C.2.

$$\text{wt\% Cu in sample} = \frac{6.71 \times 10^{-24} \text{ g Cu}}{3.5 \times 10^{-23} \text{ g total}} \times 100 = 19.2 \tag{C.2}$$

C3 Additional XPS Characterization

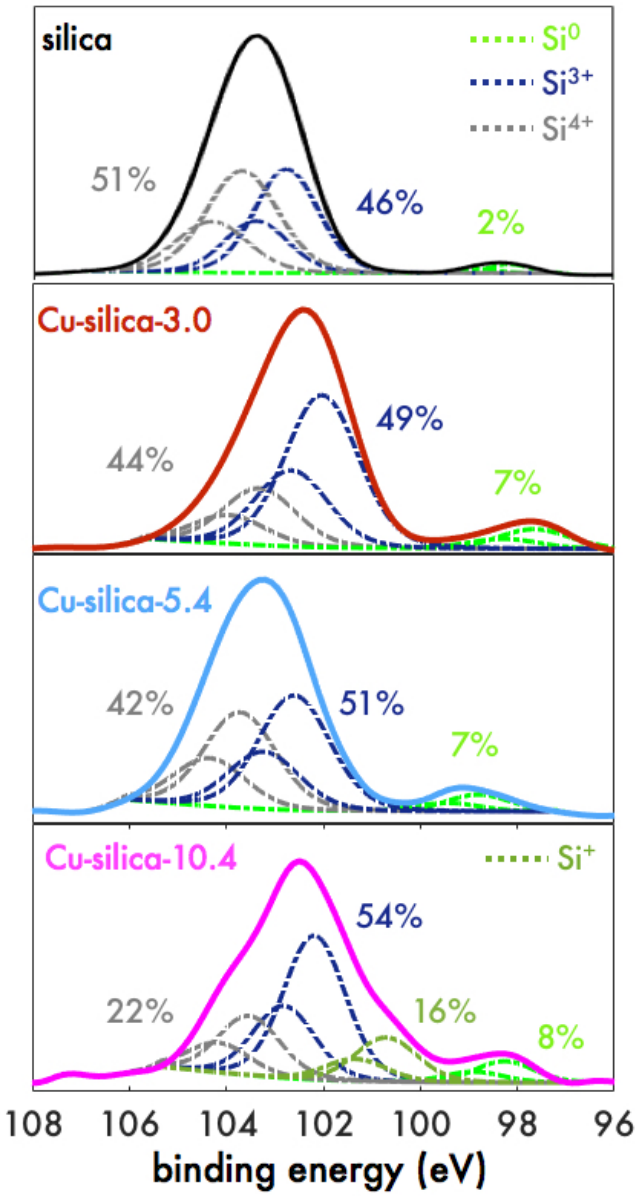

Figure C2: Si2p XP spectra of silica, Cu-silica-3.0, Cu-silica-5.4, and Cu-silica-10.4 samples. Oxidation species of Si are labeled with area % ratios of species in each sample.

C4 Investigation of Acid-Induced Dissolution of Cu

To determine whether the acidic solution of the Cu-silica-3.0 sample dissolved any Cu in the product post-synthesis before centrifugation, we centrifuged two samples of Cu-silica-5.4. One of the samples had 1 mM HNO_3 added to the product solution before transferring to a centrifuge tube, and the other one was transferred as-prepared. The supernatants (SNs)

were tested using ICP-OES to determine the amount of Cu, and compared to the total Cu detected in the samples (i.e., sum of Cu detected in SNs and pellets). Figure C3 displays the ratio of Cu(SN)/Cu(total) of the two conditions. The error bars denote the standard deviation over two injections from each sample. The sample with 1 mM added HNO_3 had a slightly higher ratio of Cu(SN)/Cu(total), signifying more Cu remained in the SN compared to the sample without added acid. However, the difference between the two samples is nearly within the measurement error. Therefore, we conclude that post-synthesis dissolution of Cu from the solid samples plays at most a small role in the low Cu loading observed under acidic conditions.

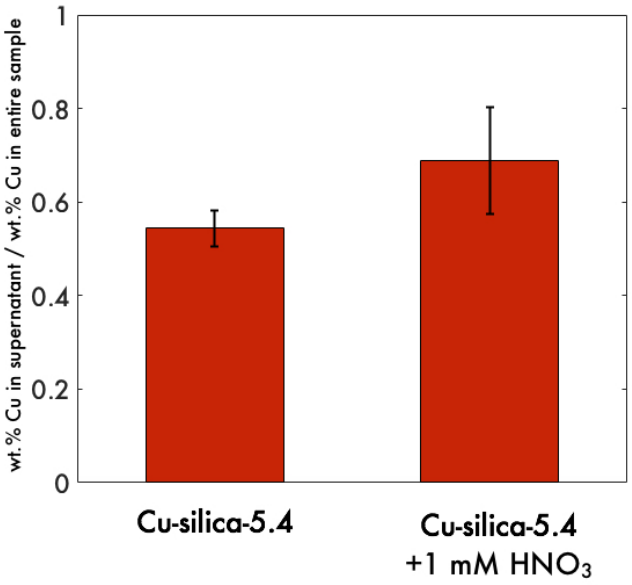

Figure C3: Ratio of Cu in supernatant (SN) over total Cu detected in sample for centrifuged Cu-silica-5.4 sample and Cu-silica-5.4 centrifuged in 1 mM HNO_3, labeled.

Appendix D

Appendix D

Link back to chapter 5.

D1 FTIR Spectra of Silica Samples

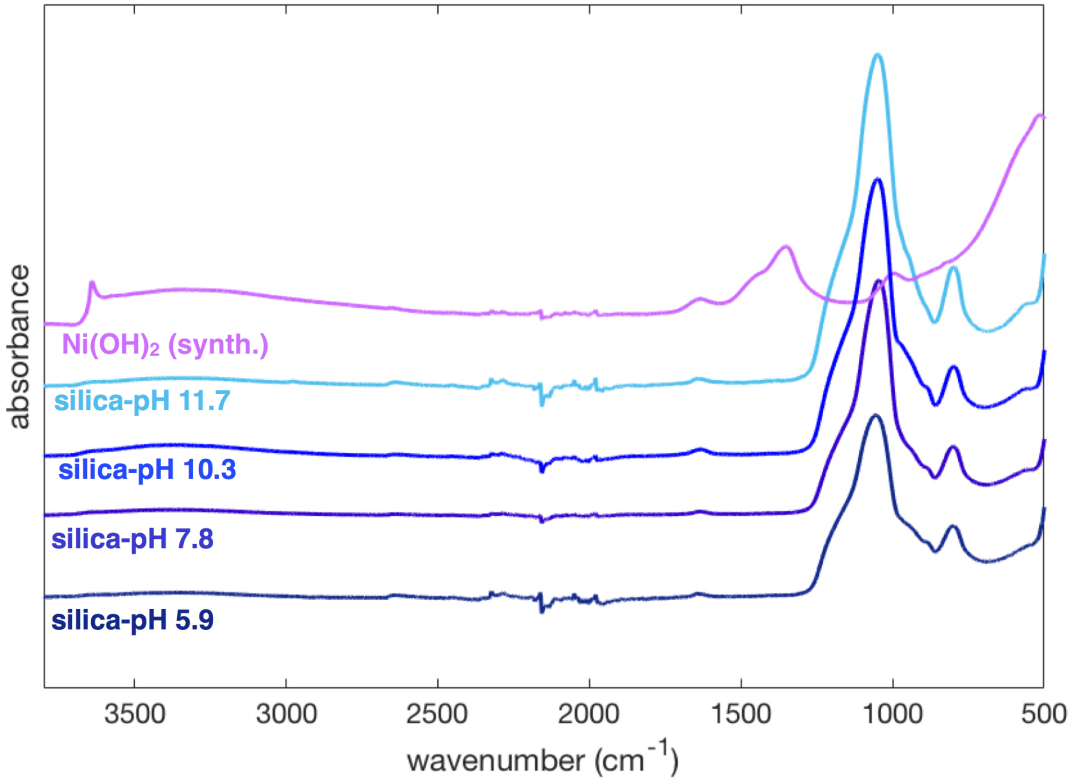

Figure D1: FTIR spectra of silica NPs generated at different pH conditions. $Ni(OH)_2$ (synth.) prepared by centrifuging and drying precursor solution of silica-Ni-pH 11.8 sample. See Table 2.2 for details.

Bibliography

[1] Dreaden, E. C.; Mackey, M. A.; Huang, X.; Kang, B.; El-Sayed, M. A. *Chem. Soc. Rev.* **2011**, *40*, 3391–3404.

[2] Bertucci, A.; Kim, K.-H.; Kang, J.; Zuidema, J. M.; Lee, S. H.; Kwon, E. J.; Kim, D.; Howell, S. B.; Ricci, F.; Ruoslahti, E.; Jang, H.-J.; Sailor, M. J. *ACS Applied Materials & Interfaces* **2019**, *11*, 23926–23937.

[3] Kang, J.; Kim, D.; Wang, J.; Han, Y.; Zuidema, J. M.; Hariri, A.; Park, J.-H.; Jokerst, J. V.; Sailor, M. J. *Advanced Materials* **2019**, *31*, 1905454.

[4] Li, Y.; Somorjai, G. A. *Nano Letters* **2010**, *10*, 2289–2295.

[5] Nozik, A. J. *Nano Letters* **2010**, *10*, 2735–2741.

[6] Liu, S.; Bai, S.-Q.; Zheng, Y.; Shah, K. W.; Han, M.-Y. *ChemCatChem* **2012**, *4*, 1462–1484.

[7] Zahmakıran, M.; Özkar, S. *Nanoscale* **2011**, *3*, 3462–3481.

[8] Gawande, M. B.; Pandey, R. K.; Jayaram, R. V. *Catal. Sci. Technol.* **2012**, *2*, 1113–1125.

[9] Di, W.; Cheng, J.; Tian, S.; Li, J.; Chen, J.; Sun, Q. *Applied Catalysis A: General* **2016**, *510*, 244 – 259.

[10] Haruta, M. *Catalysis Today* **1997**, *36*, 153 – 166, Copper, Silver and Gold in Catalysis.

[11] Li, G.; Tang, Z. *Nanoscale* **2014**, *6*, 3995–4011.

[12] Ma, Z.; Zhang, Y.; Liu, S.; Xu, W.; Wu, L.; Hsieh, Y.-C.; Liu, P.; Zhu, Y.; Sasaki, K.; Renner, J. N.; Ayers, K. E.; Adzic, R. R.; Wang, J. X. *J.Electroanal. Chem.* **2018**, *819*, 296 – 305.

[13] Moussa, S.; Abdelsayed, V.; El-Shall, M. S. *Chemical Physics Letters* **2011**, *510*, 179 – 184.

[14] Mingalev, P.; Olenin, A.; Lisichkin, G. *Petr. Chem.* **2019**, *59*.

[15] Hunter, B. M.; Blakemore, J. D.; Deimund, M.; Gray, H. B.; Winkler, J. R.; Müller, A. M. *Journal of the American Chemical Society* **2014**, *136*, 13118–13121.

[16] Guo, Z.; Liu, B.; Zhang, Q.; Deng, W.; Wang, Y.; Yang, Y. *Chem. Soc. Rev.* **2014**, *43*, 3480–3524.

[17] Gong, M.; Li, Y.; Wang, H.; Liang, Y.; Wu, J. Z.; Zhou, J.; Wang, J.; Regier, T.; Wei, F.; Dai, H. *J. Am. Chem. Soc.* **2013**, *135*, 8452–8455.

[18] Gawande, M. B.; Goswami, A.; Felpin, F.-X.; Asefa, T.; Huang, X.; Silva, R.; Zou, X.; Zboril, R.; Varma, R. S. *Chemical Reviews* **2016**, *116*, 3722–3811.

[19] Misono, M. In *Heterogeneous Catalysis of Mixed Oxides*; Misono, M., Ed.; Studies in Surface Science and Catalysis; Elsevier, 2013; Vol. 176; pp 1 – 23.

[20] Cao, S.; Tao, F. F.; Tang, Y.; Li, Y.; Yu, J. *Chem. Soc. Rev.* **2016**, *45*, 4747–4765.

[21] An, K.; Somorjai, G. A. *Catalysis Letters* **2015**, *145*, 233–248.

[22] Hu, S.; Tian, M.; Ribeiro, E. L.; Duscher, G.; Mukherjee, D. *J. Power Sources* **2016**, *306*, 413 – 423.

[23] Yu, M.; Waag, F.; Chan, C. K.; Weidenthaler, C.; Barcikowski, S.; Tüysüz, H. *ChemSusChem* **2020**, *13*, 520–528.

[24] Bian, Z.; Kawi, S. *Catalysis Today* **2020**, *339*, 3 – 23, New Opportunities and Challenges in Energy and Environmental Catalysis (EEST2018).

[25] Zhang, S.; Wang, J.; Liu, H.; Wang, X. *Catal. Commun.* **2008**, *9*, 995 – 1000.

[26] Eskandari, S.; Tate, G.; Leaphart, N. R.; Regalbuto, J. R. *ACS Catal.* **2018**, *8*, 10383–10391.

[27] Chen, L.-F.; Guo, P.-J.; Qiao, M.-H.; Yan, S.-R.; Li, H.-X.; Shen, W.; Xu, H.-L.; Fan, K.-N. *Journal of Catalysis* **2008**, *257*, 172 – 180.

[28] Cao, L.; Raciti, D.; Li, C.; Livi, K. J. T.; Rottmann, P. F.; Hemker, K. J.; Mueller, T.; Wang, C. *ACS Catalysis* **2017**, *7*, 8578–8587.

[29] Xu, C.; Chen, G.; Zhao, Y.; Liu, P.; Duan, X.; Gu, L.; Fu, G.; Yuan, Y.; Zheng, N. *Nature Commun.* **2018**, *9*, 3367.

[30] Jiao, L.; Regalbuto, J. R. *Journal of Catalysis* **2008**, *260*, 329 – 341.

[31] Munnik, P.; de Jongh, P. E.; de Jong, K. P. *Chemical Reviews* **2015**, *115*, 6687–6718.

[32] Jiao, L.; Regalbuto, J. R. *J. Catal.* **2008**, *260*, 342–350.

[33] Holby, E. F.; Sheng, W.; Shao-Horn, Y.; Morgan, D. *Energy Environ. Sci.* **2009**, *2*, 865–871.

[34] Tuxen, A. et al. *Journal of the American Chemical Society* **2013**, *135*, 2273–2278.

[35] Wong, A.; Liu, Q.; Griffin, S.; Nicholls, A.; Regalbuto, J. R. *Science* **2017**, *358*, 1427–1430.

[36] Zhang, D.; Gökce, B.; Barcikowski, S. *Chem. Rev.* **2017**, *117*, 3990–4103.

[37] Reichenberger, S.; Marzun, G.; Muhler, M.; Barcikowski, S. *ChemCatChem* **2019**, *11*, 4489–4518.

[38] Anton Fojtik, A. H. *Berichte der Bunsengesellschaft für physikalische Chemie* **1993**, *97*, 252–255.

[39] Semaltianos, N. G. *Critical Reviews in Solid State and Materials Sciences* **2010**, *35*, 105–124.

[40] Zeng, H.; Du, X.-W.; Singh, S. C.; Kulinich, S. A.; Yang, S.; He, J.; Cai, W. *Adv. Funct. Mater.* **2012**, *22*, 1333–1353.

[41] Kabashin, A. V.; Meunier, M. *J. Appl. Phys.* **2003**, *94*, 7941–7943.

[42] Kabashin, A. V.; Meunier, M.; Kingston, C.; Luong, J. H. T. *J. Phys. Chem. B* **2003**, *107*, 4527–4531.

[43] Sylvestre, J.-P.; Poulin, S.; Kabashin, A. V.; Sacher, E.; Meunier, M.; Luong, J. H. T. *J. Phys. Chem.B* **2004**, *108*, 16864–16869.

[44] Xiao, J.; Wu, Q. L.; Liu, P.; Liang, Y.; Li, H. B.; Wu, M. M.; Yang, G. W. *Nanotechnology* **2014**, *25*, 135702.

[45] Nakamura, T.; Mochidzuki, Y.; Sato, S. *J. Mater. Res.* **2008**, *23*, 968–974.

[46] Moore Tibbetts, K.; Tangeysh, B.; Odhner, J. H.; Levis, R. J. *The Journal of Physical Chemistry A* **2016**, *120*, 3562–3569, PMID: 27159014.

[47] Meader, V. K.; John, M. G.; Rodrigues, C. J.; Tibbetts, K. M. *J. Phys. Chem. A* **2017**, *121*, 6742–6754.

[48] Zhao, C.; Qu, S.; Qiu, J.; Zhu, C. *J. Mater. Res.* **2003**, *18*, 1710–1714.

[49] Tangeysh, B.; Moore Tibbetts, K.; Odhner, J. H.; Wayland, B. B.; Levis, R. J. *J. Phys. Chem. C* **2013**, *117*, 18719–18727.

[50] Odhner, J. H.; Moore Tibbetts, K.; Tangeysh, B.; Wayland, B. B.; Levis, R. J. *J. Phys. Chem. C* **2014**, *118*, 23986–23995.

[51] Uwada, T.; Wang, S.-F.; Liu, T.-H.; Masuhara, H. *J. Photochem. Photobiol. A* **2017**, *346*, 177 – 186.

[52] Herbani, Y.; Nakamura, T.; Sato, S. *J. Colloid Interface Sci.* **2012**, *375*, 78 – 87.

[53] Sarker, M. S. I.; Nakamura, T.; Herbani, Y.; Sato, S. *Appl. Phys. A* **2012**, *110*, 145–152.

[54] Tangeysh, B.; Moore Tibbetts, K.; Odhner, J. H.; Wayland, B. B.; Levis, R. J. *Nano Lett.* **2015**, *15*, 3377–3382.

[55] Tangeysh, B.; Tibbetts, K. M.; Odhner, J. H.; Wayland, B. B.; Levis, R. J. *Langmuir* **2017**, *33*, 243–252.

[56] Belmouaddine, H.; Shi, M.; Karsenti, P.-L.; Meesat, R.; Sanche, L.; Houde, D. *Phys. Chem. Chem. Phys.* **2017**, *19*, 7897–7909.

[57] Nakashima, N.; Yamanaka, K.; Saeki, M.; Ohba, H.; Taniguchi, S.; Yatsuhashi, T. *J. Photochem. Photobiol. A* **2016**, *319–320*, 70 – 77.

[58] Rodrigues, C. J.; Bobb, J. A.; John, M. G.; Fisenko, S. P.; El-Shall, M. S.; Tibbetts, K. M. *Phys. Chem. Chem. Phys.* **2018**, *20*, 28465–28475.

[59] Ferreira, P. H. D.; Vivas, M. G.; Boni, L. D.; dos Santos, D. S.; Balogh, D. T.; Misoguti, L.; Mendonca, C. R. *Opt. Express* **2012**, *20*, 518–523.

[60] Lu, W.-E.; Zheng, M.-L.; Chen, W.-Q.; Zhao, Z.-S.; Duan, X.-M. *Phys. Chem. Chem. Phys.* **2012**, *14*, 11930–11936.

[61] Tan, D.; Zhou, S.; Qiu, J.; Khusro, N. *J. Photochem. Photobiol. C* **2013**, *17*, 50 – 68.

[62] Yang, G. *Progr. Mater. Sci.* **2007**, *52*, 648 – 698.

[63] Perez, D.; Lewis, L. J. *Phys. Rev. Lett.* **2002**, *89*, 255504.

[64] Perez, D.; Béland, L. K.; Deryng, D.; Lewis, L. J.; Meunier, M. *Phys. Rev. B* **2008**, *77*, 014108.

[65] Eliezer, S.; Eliaz, N.; Grossman, E.; Fisher, D.; Gouzman, I.; Henis, Z.; Pecker, S.; Horovitz, Y.; Fraenkel, M.; Maman, S.; Lereah, Y. *Phys. Rev. B* **2004**, *69*, 144119.

[66] Sylvestre, J. P.; Kabashin, A. V.; Sacher, E.; Meunier, M. *Applied Physics A* **2005**, *80*, 753–758.

[67] Zeng, X. J.; Mao, X.; Greif, R.; Russo, R. E. Ultraviolet femtosecond and nanosecond laser ablation of silicon: ablation efficiency and laser-induced plasma expansion. High-Power Laser Ablation V. 2004; pp 1150 – 1158.

[68] Usui, H.; Shimizu, Y.; Sasaki, T.; Koshizaki, N. *J. Phys. Chem. B* **2005**, *109*, 120–124.

[69] Link, S.; Burda, C.; Mohamed, M. B.; Nikoobakht, B.; El-Sayed, M. A. *Phys. Rev. B* **2000**, *61*, 6086–6090.

[70] Elsayed-Ali, H. E.; Norris, T. B.; Pessot, M. A.; Mourou, G. A. *Phys. Rev. Lett.* **1987**, *58*, 1212–1215.

[71] Medvedev, N.; Li, Z.; Ziaja, B. *Phys. Rev. B* **2015**, *91*, 054113.

[72] Zhukov, V. P.; Tyuterev, V. G.; Chulkov, E. V. *J. Phys.: Condens. Mat.* **2012**, *24*, 405802.

[73] Sobhan, M. A.; Withford, M. J.; Goldys, E. M. *Langmuir* **2010**, *26*, 3156–3159.

[74] John, M. G.; Meader, K. V.; Tibbetts, K. M. In *Au Nanoparticle Synthesis Via Femtosecond Laser-Induced Photochemical Reduction of [AuCl4]-, Photochemistry and Photophysics - Fundamentals to Applications*; Saha, S., Mondal, S., Eds.; IntechOpen, 2018.

[75] Wang, C.; Huo, H.; Johnson, M.; Shen, M.; Mazur, E. *Nanotechnology* **2010**, *21*, 075304.

[76] von der Linde, D.; Sokolowski-Tinten, K.; Bialkowski, J. *Appl. Surf. Sci.* **1997**, *109-110*, 1 – 10.

[77] Gamaly, E. G.; Rode, A. V.; Luther-Davies, B.; Tikhonchuk, V. T. *Physics of Plasmas* **2002**, *9*, 949–957.

[78] Du, X.-W.; Qin, W.-J.; Lu, Y.-W.; Han, X.; Fu, Y.-S.; Hu, S.-L. *Journal of Applied Physics* **2007**, *102*, 013518.

[79] Liu, P.; Cai, W.; Fang, M.; Li, Z.; Zeng, H.; Hu, J.; Luo, X.; Jing, W. *Nanotechnology* **2009**, *20*, 285707.

[80] Liu, P.; Cao, Y. L.; Chen, X. Y.; Yang, G. W. *Cryst. Growth Des.* **2009**, *9*, 1390–1393.

[81] Yan, Z.; Compagnini, G.; Chrisey, D. B. *J. Phys. Chem. C* **2011**, *115*, 5058–5062.

[82] Dell'Aglio, M.; Gaudiuso, R.; De Pascale, O.; De Giacomo, A. *Applied Surface Science* **2015**, *348*, 4 – 9, Advanced Synthesis of Functional Nanoparticles by Lasers in Liquids – From Fundamentals to Application in Catalysis, Energy Science, and Biomedicine.

[83] Nathala, C. S. R.; Ajami, A.; Husinsky, W.; Farooq, B.; Kudryashov, S. I.; Daskalova, A.; Bliznakova, I.; Assion, A. *Applied Physics A* **2016**, *122*, 107.

[84] Hu, S.; Sun, J.; Du, X.; Tian, F.; Jiang, L. *Diam. Relat. Mater.* **2008**, *17*, 142 – 146.

[85] Menéndez-Manjón, A.; Barcikowski, S. *Appl. Surf. Sci.* **2011**, *257*, 4285 – 4290.

[86] Amendola, V.; Meneghetti, M. *Phys. Chem. Chem. Phys.* **2013**, *15*, 3027–3046.

[87] Tsuji, T.; Iryo, K.; Watanabe, N.; Tsuji, M. *Applied Surface Science* **2002**, *202*, 80 – 85.

[88] Nichols, W. T.; Sasaki, T.; Koshizaki, N. *J. Appl. Phys.* **2006**, *100*, 114911.

[89] Noack, J.; Vogel, A. *IEEE J. Quant. Electron.* **1999**, *35*, 1156–1167.

[90] Vogel, A.; Noack, J.; Hüttman, G.; Paltauf, G. *Appl.Phys. B* **2005**, *81*, 1015–1047.

[91] Kurihara, K.; Kizling, J.; Stenius, P.; Fendler, J. H. *J. Am. Chem. Soc.* **1983**, *105*, 2574–2579.

[92] Crowell, R. A.; Bartels, D. M. *J. Phys. Chem.* **1996**, *100*, 17940–17949.

[93] Chin, S. L.; Lagacé, S. *Appl. Opt.* **1996**, *35*, 907–911.

[94] Reuther, A.; Laubereau, A.; Nikogosyan, D. N. *J. Phys. Chem.* **1996**, *100*, 16794–16800.

[95] Pommeret, S.; Gobert, F.; Mostafavi, M.; Lampre, I.; Mialocq, J.-C. *J. Phys. Chem. A* **2001**, *105*, 11400–11406.

[96] Herbani, Y.; Nakamura, T.; Sato, S. *J. Phys. Conf. Ser.* **2017**, *817*, 012048.

[97] Besner, S.; Meunier, M. *J. Phys. Chem. C* **2010**, *114*, 10403–10409.

[98] He, D.; Garg, S.; Waite, T. D. *Langmuir* **2012**, *28*, 10266–10275.

[99] Moffett, J. W.; Zika, R. G. *Environmental Science & Technology* **1987**, *21*, 804–810.

[100] Frias Batista, L. M.; Meader, V. K.; Romero, K.; Kunzler, K.; Kabir, F.; Bullock, A.; Tibbetts, K. M. *J. Phys. Chem. B* **2019**, *123*, 7204–7213.

[101] Zeng, H.; Zhao, C.; Qiu, J.; Yang, Y.; Chen, G. *Journal of Crystal Growth* **2007**, *300*, 519 – 522.

[102] Abid, J. P.; Wark, A. W.; Brevet, P. F.; Girault, H. H. *Chem. Commun.* **2002**, 792–793.

[103] Jiménez, E.; Abderrafi, K.; Martínez-Pastor, J.; Abargues, R.; Valdés, J. L.; Ibáñez, R. *Superlattices and Microstructures* **2008**, *43*, 487 – 493, Proceedings of the 7th International Conference on Physics of Light-Matter Coupling in Nanostructures.

[104] Hu, S.; Goenaga, G.; Melton, C.; Zawodzinski, T. A.; Mukherjee, D. *Applied Catalysis B: Environmental* **2016**, *182*, 286 – 296.

[105] Hu, S.; Cheng, K.; Ribeiro, E. L.; Park, K.; Khomami, B.; Mukherjee, D. *Catal. Sci. Technol.* **2017**, *7*, 2074–2086.

[106] Hunter, B. M.; Hieringer, W.; Winkler, J. R.; Gray, H. B.; Müller, A. M. *Energy Environ. Sci.* **2016**, *9*, 1734–1743.

[107] Roske, C. W.; Lefler, J. W.; Müller, A. M. *Journal of Colloid and Interface Science* **2017**, *489*, 68 – 75, Laser Synthesis.

[108] Jiménez, E.; Abderrafi, K.; Abargues, R.; Valdés, J. L.; Martínez-Pastor, J. P. *Langmuir* **2010**, *26*, 7458–7463.

[109] Ermakov, V. A.; Jimenez-Villar, E.; Silva Filho, J. M. C. d.; Yassitepe, E.; Mogili, N. V. V.; Iikawa, F.; de Sá, G. F.; Cesar, C. L.; Marques, F. C. *Langmuir* **2017**, *33*, 2257–2262, PMID: 28186767.

[110] John, M. G.; Tibbetts, K. M. *Applied Surface Science* **2019**, *475*, 1048 – 1057.

[111] Gu, S.; Kaiser, J.; Marzun, G.; Ott, A.; Lu, Y.; Ballauff, M.; Zaccone, A.; Barcikowski, S.; Wagener, P. *Catalysis Letters* **2015**, *145*, 1105–1112.

[112] Fujita, T.; Horikawa, M.; Takei, T.; Murayama, T.; Haruta, M. *Chinese Journal of Catalysis* **2016**, *37*, 1651 – 1655.

[113] Haruta, M.; Yamada, N.; Kobayashi, T.; Iijima, S. *Journal of Catalysis* **1989**, *115*, 301 – 309.

[114] Chu, S.; Cui, Y.; Liu, N. *Nature Mater.* **2017**, *16*, 16–22.

[115] Liu, W.; Kosareva, O.; Golubtsov, I.; Iwasaki, A.; Becker, A.; Kandidov, V.; Chin, S. *Appl. Phys. B* **2003**, *76*, 215–229.

[116] Sreeja, S.; Venugopal Rao, S.; Radhakrishnan, P.; Tewari, S. P.; Prem Kiran, P. Supercontinuum emission from water using fs pulses in the external tight focusing limit. Proc. SPIE. 2012; pp 824718–824718–6.

[117] Sreeja, S.; Leela, C.; Kumar, V. R.; Bagchi, S.; Prashant, T. S.; Radhakrishnan, P.; Tewari, S. P.; Rao, S. V.; Kiran, P. P. *Laser Physics* **2013**, *23*, 106002.

[118] Bergé, L.; Skupin, S.; Nuter, R.; Kasparian, J.; Wolf, J.-P. *Prog. Rep. Phys.* **2007**, *70*, 1633.

[119] Milián, C.; Jarnac, A.; Brelet, Y.; Jukna, V.; Houard, A.; Mysyrowicz, A.; Couairon, A. *J. Opt. Soc. Am. B* **2014**, *31*, 2829–2837.

[120] Wunder, S.; Polzer, F.; Lu, Y.; Mei, Y.; Ballauff, M. *The Journal of Physical Chemistry C* **2010**, *114*, 8814–8820.

[121] Tai, Y.; Yamaguchi, W.; Tajiri, K.; Kageyama, H. *Appl. Catal., A* **2009**, *364*, 143 – 149.

[122] 3, *Catal. Sci. Technol.* **2013**, *3*, 679–687.

[123] Heimann, P.; van der Veen, J.; Eastman, D. *Sol. Stat. Commun.* **1981**, *38*, 595–598.

[124] Klyushin, A. Y.; Rocha, T. C. R.; Hävecker, M.; Knop-Gericke, A.; Schlögl, R. *Phys. Chem. Chem. Phys.* **2014**, *16*, 7881–7886.

[125] Weststrate, C.; Lundgren, E.; Andersen, J.; Rienks, E.; Gluhoi, A.; Bakker, J.; Groot, I.; Nieuwenhuys, B. *Surf. Sci.* **2009**, *603*, 2152 – 2157.

[126] Koslowski, B.; Boyen, H.-G.; Wilderotter, C.; Kästle, G.; Ziemann, P.; Wahrenberg, R.; Oelhafen, P. *Surface Science* **2001**, *475*, 1 – 10.

[127] Radnik, J.; Mohr, C.; Claus, P. *Phys. Chem. Chem. Phys.* **2003**, *5*, 172–177.

[128] Gross, T.; Ramm, M.; Sonntag, H.; Unger, W.; Weijers, H. M.; Adem, E. H. *Surface and Interface Analysis* **1992**, *18*, 59–64.

[129] Kim, Y. H.; Lee, D. K.; Cha, H. G.; Kim, C. W.; Kang, Y. C.; Kang, Y. S. *The Journal of Physical Chemistry B* **2006**, *110*, 24923–24928.

[130] Sublemontier, O.; Nicolas, C.; Aureau, D.; Patanen, M.; Kintz, H.; Liu, X.; Gaveau, M.-A.; Le Garrec, J.-L.; Robert, E.; Barreda, F.-A.; Etcheberry, A.; Reynaud, C.; Mitchell, J. B.; Miron, C. *J. Phys. Chem. Lett.* **2014**, *5*, 3399–3403.

[131] Himpsel, F. J.; McFeely, F. R.; Taleb-Ibrahimi, A.; Yarmoff, J. A.; Hollinger, G. *Phys. Rev. B* **1988**, *38*, 6084–6096.

[132] Bhattacharya, A. K.; Pyke, D. R.; Reynolds, R.; Walker, G. S.; R., W. C. *J. Mater. Sci. Let.* **1997**, *16*, 1–3.

[133] Geng, S.; Zhang, S.; Onishi, H. *Mater. Tech.* **2002**, *17*, 234–240.

[134] Crist, B. *The Handbooks of Monochromatic XPS Spectra Series: Commercially Pure Binary Oxides*; XPS International, 2004; Vol. v. 2.

[135] Francis, S. M.; Stephens, W. E.; Richardson, N. V. *Environmental Health* **2009**, *8*, S4.

[136] Moulder, J. F.; Stickle, W. F.; Sobol, P. E.; Bomben, K. D. In *Handbook of X-ray Photoelectron Spectroscopy*; Prairie, E., Ed.; Perkin-Elmer Corp., Physical Electronics Division, 1979.

[137] Grunthaner, F.; Grunthaner, P.; Vasquez, R.; Lewis, B.; Maserjian, J. *J. Vac. Sci. Techn.* **1979**, *16*, 1443.

[138] Soh, M. T. K.; Thomas, J. H.; Talghader, J. J. *Journal of Vacuum Science & Technology A* **2006**, *24*, 2147–2150.

[139] Shih, C.-Y.; Streubel, R.; Heberle, J.; Letzel, A.; Shugaev, M. V.; Wu, C.; Schmidt, M.; Gökce, B.; Barcikowski, S.; Zhigilei, L. V. *Nanoscale* **2018**, *10*, 6900–6910.

[140] Liu, P.; Chen, H.; Wang, H.; Yan, J.; Lin, Z.; Yang, G. *J. Phys. Chem. C* **2015**, *119*, 1234–1246.

[141] Shih, C.-Y.; Wu, C.; Shugaev, M. V.; Zhigilei, L. V. *J. Colloid Interface Sci.* **2017**, *489*, 3 – 17.

[142] Görlich, E.; Haber, J.; Stoch, A.; Stoch, J. *J. Sol. St. Chem.* **1980**, *33*, 121–124.

[143] Lee, Y.; rak Choi, J.; Lee, K. J.; Stott, N. E.; Kim, D. *Nanotechnology* **2008**, *19*, 415604.

[144] Zhao, P.; Feng, X.; Huang, D.; Yang, G.; Astruc, D. *Coordination Chemistry Reviews* **2015**, *287*, 114 – 136.

[145] Gamaly, E. *Femtosecond Laser-Matter Interactions: Theory, Experiments and Applications*; Pen Stanford, 2011.

[146] Ionin, A. A.; Kudryashov, S. I.; Seleznev, L. V.; Sinitsyn, D. V.; Bunkin, A. F.; Lednev, V. N.; Pershin, S. M. *Journal of Experimental and Theoretical Physics* **2013**, *116*, 347–362.

[147] Behar, D.; Rabani, J. *J. Phys. Chem. B* **2006**, *110*, 8750–8755.

[148] Nikogosyan, D. N.; Oraevsky, A. A.; Rupasov, V. I. *Chem. Phys.* **1983**, *77*, 131 – 143.

[149] Lorazo, P.; Lewis, L. J.; Meunier, M. *Phys. Rev. B* **2006**, *73*, 134108.

[150] Saraeva, I. N.; Luong, N. V.; Kudryashov, S. I.; Rudenko, A. A.; Khmelnitskiy, R. A.; Shakhmin, A. L.; Kharin, A. Y.; Ionin, A. A.; Zayarny, D. A.; Tung, D. H.; Duong, P. V.; Minh, P. H. *Journal of Photochemistry and Photobiology A: Chemistry* **2018**, *360*, 125 – 131.

[151] Niu, X.; L, Y.; Tang, J.; Hu, Y.; Zhao, H.; Lan, M. *Biosensors and Bioelectronics* **2014**, *51*, 22 – 28.

[152] Raspolli Galletti, A. M.; Antonetti, C.; Marracci, M.; Piccinelli, F.; Tellini, B. *Appl. Surf. Sci.* **2013**, *280*, 610 – 618.

[153] Sheng, Y.; Zeng, H. C. *Chemistry of Materials* **2015**, *27*, 658–667.

[154] Yin, G.; Nishikawa, M.; Nosaka, Y.; Srinivasan, N.; Atarashi, D.; Sakai, E.; Miyauchi, M. *ACS Nano* **2015**, *9*, 2111–2119.

[155] Zhu, L.; Li, H.; Liu, Z.; Xia, P.; Xie, Y.; Xiong, D. *The Journal of Physical Chemistry C* **2018**, *122*, 9531–9539.

[156] Zhao, Y.; Zhao, J.; Su, Z.; Hao, X.; Li, Y.; Li, N.; Li, Y. *J. Mater. Chem. A* **2013**, *1*, 8029–8036.

[157] Gong, J.; Yue, H.; Zhao, Y.; Zhao, S.; Zhao, L.; Lv, J.; Wang, S.; Ma, X. *Journal of the American Chemical Society* **2012**, *134*, 13922–13925.

[158] Huang, Z.; Li, F.; Chen, B.; Xue, F.; Chen, G.; Yuan, G. *Applied Catalysis A: General* **2011**, *403*, 104 – 111.

[159] Lastovina, T. A.; Budnyk, A. P.; Khaishbashev, G. A.; Kudryavtsev, E. A.; Soldatov, A. V. *J. Serbian Chem. Soc.* **2016**, *81*, 751–762.

[160] Wang, X.; Ma, K.; Guo, L.; Tian, Y.; Cheng, Q.; Bai, X.; Huang, J.; Ding, T.; Li, X. *Applied Catalysis A: General* **2017**, *540*, 37 – 46.

[161] Liu, P.; Li, Z.; Cai, W.; Fang, M.; Luo, X. *RSC Adv.* **2011**, *1*, 847–851.

[162] Santillán, J. M. J.; Videla, F. A.; Fernández van Raap, M. B.; Schinca, D. C.; Scaffardi, L. B. *Journal of Applied Physics* **2012**, *112*, 054319.

[163] Santillán, J. M. J.; Videla, F. A.; Fernández van Raap, M. B.; Schinca, D. C.; Scaffardi, L. B. *Journal of Applied Physics* **2013**, *113*, 134305.

[164] Biesinger, M. C. *Surf. Interf. Anal.* **2017**, *49*, 1325–1334.

[165] Biesinger, M. C.; Lau, L. W.; Gerson, A. R.; Smart, R. S. *Applied Surface Science* **2010**, *257*, 887 – 898.

[166] Marques, M.; Ferraria, A.; Correia, J.; Botelho do Rego, A.; Vilar, R. *Materials Chemistry and Physics* **2008**, *109*, 174 – 180.

[167] Tahir, D.; Tougaard, S. *Journal of Physics: Condensed Matter* **2012**, *24*, 175002.

[168] Ye, R.-P.; Lin, L.; Yang, J.-X.; Sun, M.-L.; Li, F.; Li, B.; Yao, Y.-G. *Journal of Catalysis* **2017**, *350*, 122–132.

[169] Li, X.; Zhang, J.; Zhang, M.; Zhang, W.; Zhang, M.; Xie, H.; Wu, Y.; Tan, Y. *Catalysts* **2019**, *9*.

[170] Huang, X.; Ma, M.; Miao, S.; Zheng, Y.; Chen, M.; Shen, W. *Applied Catalysis A: General* **2017**, *531*, 79 – 88.

[171] Dahle, S.; Wegewitz, L.; Qi, F.; Weber, A.; Maus-Friedrichs, W. *Plasma Chemistry and Plasma Processing* **2013**, *33*.

[172] Lamastra, F.; Mori, S.; Cherubini, V.; Scarselli, M.; Nanni, F. *Materials Chemistry and Physics* **2017**, *194*, 253–260.

[173] Won Ma, J.; Lee, W.-J.; Bae, J. M.; Jeong, K.; Hoon Oh, S.; Kim, J.-H.; Kim, S.-h.; Seo, J.-H.; Ahn, J.-P.; Kim, H.; Cho, M.-H. *Nano letters* **2015**, *15*.

[174] Al-Kattan, A.; Ryabchikov, Y.; Baati, T.; Chirvony, V.; Sánchez Royo, J. F.; Sentis, M.; Braguer, D.; Timoshenko, V.; Estève, M.-A.; V. Kabashin, A. *J. Mater. Chem. B* **2016**, *4*, 7852–7858.

[175] Bashouti, M.; Sardashti, K.; Ristein, J.; Christiansen, S. *Physical chemistry chemical physics : PCCP* **2012**, *14*, 11877–81.

[176] Kong, Y.; Zhu, H.; Yang, G.; Guo, X.; Hou, W.; Yan, Q.; Gu, M.; Hu, C. *Advanced Functional Materials* **2004**, *14*, 816–820.

[177] Toupance, T.; Kermarec, M.; Lambert, J.-F.; Louis, C. *The Journal of Physical Chemistry B* **2002**, *106*, 2277–2286.

[178] Wang, Z.-Q.; Xu, Z.-N.; Peng, S.-Y.; Zhang, M.-J.; Lu, G.; Chen, Q.-S.; Chen, Y.; Guo, G.-C. *ACS Catalysis* **2015**, *5*, 4255–4259.

[179] Huang, Z.; Cui, F.; Kang, H.; Chen, J.; Zhang, X.; Xia, C. *Chemistry of Materials* **2008**, *20*, 5090–5099.

[180] Li, H.; Ban, L.; Wang, Z.; Meng, P.; Zhang, Y.; Wu, R.; Zhao, Y. *Nanomaterials* **2019**, *9*.

[181] Monshi, A.; Foroughi, M. R.; Monshi, M. *World Journal of Nano Science and Engineering* **2012**, *2*, 154–160.

[182] Mäki-Arvela, P.; Murzin, D. Y. *Appl. Cat. A: General* **2013**, *451*, 251 – 281.

[183] Trouillet, L.; Toupance, T.; Villain, F.; Louis, C. *Phys. Chem. Chem. Phys.* **2000**, *2*, 2005–2014.

[184] Guerreiro, E.; Gorriz, O.; Larsen, G.; Arrúa, L. *Applied Catalysis A: General* **2000**, *204*, 33 – 48.

[185] Rudolf, C.; Abi-Ghaida, F.; Dragoi, B.; Ungureanu, A.; Mehdi, A.; Dumitriu, E. *Catal. Sci. Technol.* **2015**, *5*, 3735–3745.

[186] Khdary, N. H.; Ghanem, M. A.; Abdesalam, M. E.; Al-Garadah, M. M. *Journal of Saudi Chemical Society* **2018**, *22*, 343 – 351.

[187] Yue, H.; Zhao, Y.; Zhao, S.; Wang, B.; Ma, X.; Gong, J. *Nature Communications* **2013**, *4*, 2339 EP –.

[188] van der Grift, C.; Elberse, P.; Mulder, A.; Geus, J. *Appl. Cat.* **1990**, *59*, 275–289.

[189] Crundwell, F. K. *ACS Omega* **2017**, *2*, 1116–1127.

[190] Schreier, M.; Teren, S.; Belcher, L.; Regalbuto, J.; Miller, J. *Nanotechnology* **2005**, *16*, S582–91.

[191] Nomoev, A. V.; Bardakhanov, S. P.; Schreiber, M.; Bazarova, D. G.; Romanov, N. A.; Baldanov, B. B.; Radnaev, B. R.; Syzrantsev, V. V. *Beilstein J. Nanotechnol.* **2015**, *6*, 874–880.

[192] Eustathopoulos, N.; Drevet, B. *Journal of Crystal Growth* **2013**, *371*, 77 – 83.

[193] Sivaiah, M.; Petit, S.; Barrault, J.; Batiot-Dupeyrat, C.; Valange, S. *Catalysis Today* **2010**, *157*, 397 – 403.

[194] Burattin, P.; Che, M.; Louis, C. *J. Phys. Chem. C* **1997**, *101*, 7060–7074.

[195] Burattin, P.; Che, M.; Louis, C. *The Journal of Physical Chemistry B* **1998**, *102*, 2722–2732.

[196] Kermarec, M.; Carriat, J. Y.; Burattin, P.; Che, M.; Decarreau, A. *J. Phys. Chem.* **1994**, *98*, 12008–12017.

[197] John, M. G.; Tibbetts, K. M. *Appl. Surf. Sci.* **2020**, *510*, 145037.

[198] Waag, F.; Gökce, B.; Kalapu, C.; Bendt, G.; Salamon, S.; Landers, J.; Hagemann, U.; Heidelmann, M.; Schulz, S.; Wende, H.; Hartmann, N.; Behrens, M.; Barcikowski, S. *Scientific Reports* **2017**, *7*, 13161.

[199] Mizutani, T.; Fukushima, Y.; Okada, A.; Kamigaito, O. *Bulletin of the Chemical Society of Japan* **1990**, *63*, 2094–2098.

[200] Shao, M.; Hu, H.; Ban, H.; Li, M.; Gao, H. *J. Cryst. Growth* **2007**, *303*, 391 – 394.

[201] Ye, R.-P.; Gong, W.; Sun, Z.; Sheng, Q.; Shi, X.; Wang, T.; Yao, Y.; Razink, J. J.; Lin, L.; Zhou, Z.; Adidharma, H.; Tang, J.; Fan, M.; Yao, Y.-G. *Energy* **2019**, *188*, 116059.

[202] Yang, M.; Jin, P.; Fan, Y.; Huang, C.; Zhang, N.; Weng, W.; Chen, M.; Wan, H. *Catal. Sci. Technol.* **2015**, *5*, 5095–5099.

[203] Krasilin, A. A.; Nevedomsky, V. N.; Gusarov, V. V. *J. Phys. Chem. C* **2017**, *121*, 12495–12502.

[204] Kong, X.; Zhu, Y.; Zheng, H.; Li, X.; Zhu, Y.; Li, Y.-W. *ACS Catal.* **2015**, *5*, 5914–5920.

[205] Lehmann, T.; Wolff, T.; Hamel, C.; Veit, P.; Garke, B.; Seidel-Morgenstern, A. *Micropor. Mesopor. Mater.* **2012**, *151*, 113 – 125.

[206] Chen, B.-H.; Chao, Z.-S.; He, H.; Huang, C.; Liu, Y.-J.; Yi, W.-J.; Wei, X.-L.; An, J.-F. *Dalton Trans.* **2016**, *45*, 2720–2739.

[207] Nesbitt, H. W.; Legrand, D.; Bancroft, G. M. *Physics and Chemistry of Minerals* **2000**, *27*, 357–366.

[208] Biesinger, M. C.; Payne, B. P.; Lau, L. W. M.; Gerson, A.; Smart, R. S. C. *Surf. Interf. Anal.* **2009**, *41*, 324–332.

[209] Semaltianos, N. G.; Logothetidis, S.; Perrie, W.; Romani, S.; Potter, R. J.; Edwardson, S. P.; French, P.; Sharp, M.; Dearden, G.; Watkins, K. G. *J. Nanopart. Res.* **2010**, *12*, 573–580.

[210] Rioux, D.; Laferrière, M.; Douplik, A.; Shah, D.; Lilge, L. D.; Kabashin, A. V.; Meunier, M. *J. Biomed. Opt.* **2009**, *14*, 14–14–5.

[211] Lemishko, S. S.; Lemishko, A. S. *J. Phys. Chem. C* **2017**, *121*, 3234–3240.

[212] Duarte, H. A.; Lourenço, M. P.; Heine, T.; Guimarães, L. In *Stoichiometry and Materials Science*; Innocenti, A., Kamarulzaman, N., Eds.; IntechOpen: Rijeka, 2012; Chapter 1.

[213] McDonald, A.; Scott, B.; Villemure, G. *Micropor. Mesopor. Mater.* **2009**, *120*, 263 – 266.

[214] Bonelli, B.; Bottero, I.; Ballarini, N.; Passeri, S.; Cavani, F.; Garrone, E. *J. Catal.* **2009**, *264*, 15–30.

[215] Lvov, Y.; Wang, W.; Zhang, L.; Fakhrullin, R. *Adv. Mater.* **2016**, *28*, 1227–1250.

[216] White, R. D.; Bavykin, D. V.; Walsh, F. C. *J. Mater. Chem. A* **2013**, *1*, 548–556.

[217] Bae, K.-L.; Kim, J.; Lim, C. K.; Nam, K. M.; Song, H. *Nature Commun.* **2017**, *8*, 1156.

[218] Amendola, V.; Amans, D.; Ishikawa, Y.; Koshizaki, N.; Scirè, S.; Compagnini, G.; Reichenberger, S.; Barcikowski, S. *Chem. Eur n/a*.

[219] Omar, F. M.; Aziz, H. A.; Stoll, S. *Sci. Total Environ.* **2014**, *468-469*, 195 – 201.

[220] Haiss, W.; Thanh, N. T. K.; Aveyard, J.; Fernig, D. G. *Analytical Chemistry* **2007**, *79*, 4215–4221, PMID: 17458937.

[221] Hervés, P.; Pérez-Lorenzo, M.; Liz-Marzán, L. M.; Dzubiella, J.; Lu, Y.; Ballauff, M. *Chem. Soc. Rev.* **2012**, *41*, 5577.

[222] Pradhan, N.; Pal, A.; Pal, T. *Colloids and Surfaces A: Physicochemical and Engineering Aspects* **2002**, *196*, 247 – 257.